Hydrodynamics of Rod-Like Colloids and Vesicles

Inaugural-Dissertation
zur
Erlangung des Doktorgrades
der Mathematisch-Naturwissenschaftlichen Fakultät
der Universität zu Köln

vorgelegt von

Sebastian Meßlinger

aus Essen

Köln

2008

Berichterstatter:	Prof. Dr. Gerhard Gompper
	Prof. Dr. Joachim Krug

Tag der mündlichen Prüfung: 24.06.2008

Contents

Abstract

We investigate the dynamics of rod-like colloids and vesicles by means of computer simulations. These two systems are examples of the rich dynamics in “soft-matter” systems, which is characterized by large relaxation times. Therefore, dynamical behavior in soft-matter systems is easily accessable experimentally, and soft materials are driven into non-equilibrium states, already by weak external fields. Both systems have in common that they serve as model systems for transport phenomena in cell biology. We focus on the influence of hydrodynamic interactions. This is realized by the use of a mesoscale hydrodynamics simulation technique called the ”Multi Particle Collision Dynamics” (MPC) method, which takes the solvent into account explicitly.

We calculate self-diffusion constants of rod-like colloids in the isotropic and nematic phases. Rod diffusion is strongly influenced by steric and hydrodynamic interactions between rods. Due to the anisotropy of the nematic phase also diffusion is anisotropic in such systems. We find that hydrodynamic effects lead to an increased diffusion. Moreover, our simulations show that the diffusion anisotropy of the nematic phase depends on the rod aspect ratio. Our simulation results are compared to experimental measurements of our cooperation partners (group J. K. G. Dhont, FZ-Jülich) who measured diffusion constants of rod-like *fd*-viruses suspensions. Our observations of the hydrodynamic enhancement and the anisotropy of rod self-diffusion are in good agreement with the experiments.

A small amount of spherical tracer colloids is added to the rod suspensions described above, and tracer-sphere diffusion constants are determined. They also exhibit a strong diffusion anisotropy in the nematic phase. The effect of the rod network on tracer-sphere diffusion can be divided into a steric and hydrodynamic contribution. Our results are in good agreement with theoretical predictions which incorporate hydrodynamic effects. An important quantity for the calculation of the theoretical diffusion constants is the hydrodynamic screening length, which is difficult to measure in experiments, but can be directly calcu-

lated in simulations.

Due to the high concentration of rods, the typically long-ranged hydrodynamic interactions, which depend inversely proportional on the distance between colloids, are screened such that they decay exponentially. We have developed a method which allows us to calculate hydrodynamic screening lengths from the equilibrium fluctuations of solvent shear waves. With this method, we are also able to determine anisotropic screening lengths in nematic systems. We show that hydrodynamic screening lengths are of the order of typical distances between neighboring rods. The calculated screening lengths are able to explain tracer-sphere diffusion constants quantitatively.

Far more complex than rod suspensions are vesicles, as they have an internal dynamics. We study vesicles in shear flow in a two-dimensional model system which shows a variety of interesting dynamical phenomena. Depending on the viscosity ratio, i.e. the ratio between the inner and the outer viscosity of the vesicle, they can either "tumble", "swing" or show "tank-treading". In the tumbling regime, the vesicle orientation permanently rotates, in the swinging regime the vesicle exhibits temporally periodical changes in shape and orientation and in the tank-treading regime both shape and orientation are constant, whereas the membrane rotates around the enclosed volume. For the first time, a transition from tank-treading to swinging with increasing viscosity contrast could be shown in computer simulations. Our simulations are in good agreement with a phenomenological theoretical description.

Close to walls, tumbling is strongly suppressed. Furthermore, the vesicle is repelled from the wall. The origin of this repulsion is the hydrodynamical lift force. We find that the lift force decays inversely proportional to the squared wall distance and that it decays with increasing viscosity contrast. The lift force is of relevance for the motion of blood cells in blood flow.

1 Introduction

In our everyday life, we are permanently concerned with soft materials. Such soft materials are e.g. butter, mayonnaise, tooth paste, motor oil, shampoo or the foam on top of our cappuccino. The main characteristics of soft matter is that it is easily deformable, where small deformations are elastic, like in solids, but on the same time, the system can be easily deformed irreversibly, like in liquids. This "viscoelastic" behavior is a key property of soft matter systems. The physical origin of the softness arises from the fact that the relevant length scales of soft matter are mesoscopic, i.e. they are significantly larger than the atomic scale, but still small enough that thermal fluctuations play a significant role. Typically, this regime ranges from several nano- to micrometers. On the other hand, adhesion energies between mesoscopic objects are of the order of the thermal energy. Since many systems with very different internal architectures exhibit these characteristics, soft matter is very versatile. Soft matter can be subdivided into several classes, which all have in common that building blocks are mesoscopic. Colloids are small solid or even soft particles immersed into a liquid environment, commonly referred to as solvent [23]. The relevant length scales are the sizes of colloids which are in the range of 10 nm to 10 μm. Polymers are long chain-like macromolecules, which are very flexible and therefore typically coil in order to maximize entropy [28]. Here the crucial length scales are the polymer length or the diameter of the polymer coil. Typical molecular weights are 1 kg/mol to 100 kg/mol which correspond to coil radii of 5 nm to 100 nm. Membranes are two-dimensional sheets of amphiphilic molecules in a liquid environment. If membranes enclose a small volume of a liquid they are called vesicles. Here the important length scales are the spatial extensions of the membrane or the typical vesicle radius.

Soft matter is of high relevance also for cell biology, since all the above mentioned soft matter systems can be regarded as model systems for biological systems. For example, many proteins, protein aggregates like F-actin filaments, cellulose fibres, and many viruses can be regarded as colloids. Also many molecules which are found in cell biology like DNA or proteins are polymers. Lipid bilayer membranes are found at many different places in and around the cell, wherever different cell compartments have to be spatially separated from each other.

The strong influence of thermal fluctuations leads to phenomena which cannot be observed for macroscopic objects. Among these are diffusion, Brownian forces due to density gradients or entropic spring forces in polymers. All these effects have in common that they tend to minimize the free energy. Moreover, the typically low energy barriers can often be overcome in order to find global minima in the free-energy landscape. Thus, proteins can fold into their native states, or self-assembly of lipid-molecules into lipid-bilayer membranes is possible.

A variety of interactions are crucial for soft matter. Among these are electrostatic, direct steric, hydrodynamic, attractive van-der-Waals interactions and forces arising from interfacial tension. There are many possibilities to change these interactions. For example, electrostatic interactions can be screened by the addition of salt or interfacial tensions can be varied by adding surfactants. Due to the strong influence of thermal fluctuations, small changes of interaction strengths are able to alter the system properties drastically.

The large separation in lengths scales comes along with a broad range of relevant time scales. Depending on the particular soft matter system and the dynamic process of interest, relevant times range from nanoseconds to seconds. The lower boundary is the time scale for which inertial effects of colloids are lost due to thermal fluctuations, whereas the upper limit is the relevant time for the formation of some highly ordered phases. Thereby the dynamics in soft matter systems is generally far slower than in solid systems. Due to the large length and time scales, dynamical phenomena in soft matter systems can be often investigated by direct optical methods. In particular, colloidal systems are therefore often used as model systems in order to understand dynamical phenomena like phase separations or particle diffusion for general particle-based systems.

Many soft matter systems contain liquid ingredients, commonly referred to as solvents, which are typically aqueous solutions or oils. The individual solvent molecules are not relevant for the behavior of soft matter systems, and the whole solvent can be regarded as a fluctuating continuum. Its crucial effects on immersed mesoscopic objects are thermal random forces and solvent-mediated hydrodynamic interactions (HI). The former effect arises from thermal motion of solvent molecules, whereas the latter is due to collective solvent particle motion. A consequence of the meso-scaled object sizes and high viscosities is that inertial effects are negligible for soft matter systems. Hydrodynamic interactions are long ranged as they decay reciprocally with distance. Moreover, they have a strong influence on the dynamics of immersed objects and thereby on the whole soft matter system itself.

Mesoscopic length scales, thermal fluctuations and hydrodynamic as well as other interactions are the general characteristics of soft matter. In order to investigate soft matter systems by computer simulations, the simulation method has to incorporate all these effects. Due to the large separation in length and time scales an efficient treatment by Molecular Dynamics on an atomistic level is not feasible. Instead we use a mesoscale particle-based simulation technique, the “Multi Particle Collision” Dynamics (MPC) algorithm, which takes into account all hydrodynamic and thermodynamic properties which are essential for the dynamics of soft matter.

Colloidal particles are often spherical, but there are also many examples of rod-like colloids. Rod-like colloids are particularly relevant as model systems for cell biology, as many biological filaments are embedded in a liquid environment. The cytoplasm, i.e. the interior of a biological cell, is a crowded environment which typically contains many filamentous structures like F-actin and microtubuli. Rod-like colloids have been studied intensively in the past. In particular static properties, like the formation of phases are well known. For small concentrations, rods are oriented isotropically. With increasing concentration, a nematic phase is formed, where rods have a favoured orientation, but no positional order.

However, far less studied are the dynamical phenomena in isotropic and nematic rod systems, although it is of high importance for the understanding of diffusive transport in dense filament networks. In particular, the current knowledge about the influence of solvent-mediated hydrodynamic interactions on colloid dynamics is very poor. With the use of the MPC method, we are able to answer many open questions on hydrodynamic interactions in rod suspensions.

Far more complex than rod suspensions are vesicles which have an internal dynamics. These interesting objects are of high biological relevance. In the cytosol, many different kinds of vesicles can be found. Vesicles store, transport, or digest cellular products and waste, but also individual cells like blood cells can be regarded as vesicles. In particular for red blood cells, it is crucial to understand, how the vesicle behaves in shear flow and how vesicle dynamics is affected by a viscosity contrast, i.e. a different solvent viscosity inside and outside of the vesicle. It is known that vesicles in shear flow can be found in different dynamical regimes, where the orientation and the shape of the vesicle are either constant in time or undergo periodic changes. However, the influence of a viscosity contrast on the formation of dynamical regimes has not been studied so far by simulations taking into account thermal fluctuations.

A further interesting phenomenon is the hydrodynamic lift force, which acts on vesicles in shear flow closed to a wall. Due to this hydrodynamic force, the vesicle is repelled from the wall. It is of high interest to understand the dependence of the lift force on the distance from a wall and the influence of a viscosity contrast on the lift force.

2 Scientific background

2.1 Hydrodynamics

Hydrodynamics is the science of the dynamics of liquids. Although this research field is very complex, its effects can be observed directly in everyday life – in contrast to other complex subjects like relativity or quantum mechanics. Hydrodynamic effects are for example used while swimming, paddling on a lake, stiring coffee or opening a water tap. Hydrodynamics of simple fluids can be well described by the incompressible Navier-Stokes equation:

$$\begin{aligned} \varrho_m \left(\frac{\partial \mathbf{v}}{\partial t} + (\mathbf{v} \cdot \nabla)\mathbf{v} \right) &= \eta \nabla^2 \mathbf{v} - \nabla p + \mathbf{f}_{ext} \\ \nabla \cdot \mathbf{v} &= 0 \end{aligned} \tag{2.1}$$

Here $\mathbf{v} = \mathbf{v}(\mathbf{r}, t)$ denotes the velocity field, $p = p(\mathbf{r}, t)$ the pressure field, η is the fluid viscosity, ϱ_m is the mass density and $\mathbf{f}_{ext} = \mathbf{f}_{ext}(\mathbf{r}, t)$ is an external body force field (force per volume). The second equation expresses incompressibility of the liquid. The Navier-Stokes equation can be derived by balancing the forces acting on a volume element of a fluid (see, e.g. Ref. [62]). Once the external body force field $\mathbf{f}_{ext}(\mathbf{r}, t)$ together with the boundary conditions is known, the Navier-Stokes equation can be – at least in principle – solved, i.e. the velocity $\mathbf{v}(\mathbf{r}, t)$ and the pressure fields $p(\mathbf{r}, t)$ can be determined. However, since the Navier-Stokes equation is non-linear, this is not a trivial task. The non-linear term is responsible for chaotic phenomena like turbulence. Analytic solutions exist only for few special cases with very simple geometries and flow conditions [62].

The general approach is to find solutions numerically. Because of its practical relevance, this is a huge research field in computational science, called "**C**omputational **F**luid **D**ynamics" (CFD) [34, 99].

However, for typical soft matter systems, it can be shown that the contribution of the non-linear term in the Navier-Stokes equation becomes negligible. for a characteristic length l_c and a characteristic velocity v_c of the soft matter system of interest, we can rescale all quantities appearing in the Navier-Stokes equation (2.1),

$$t' = tu/l_c \qquad p' = \frac{l_c p}{\eta v_c}$$
$$v' = v/u \qquad f'_{ext} = \frac{l_c^2 f_{ext}}{\eta v_c}$$
$$\nabla' = l_c \nabla$$

With these quantities, the Navier-Stokes equation can be rewritten in a dimensionless form,

$$\begin{aligned} Re\left(\frac{\partial \mathbf{v}'}{\partial t'} + (\mathbf{v}' \cdot \nabla')\mathbf{v}'\right) &= \nabla'^2 \mathbf{v}' - \nabla' p' + \mathbf{f}'_{ext} \qquad (2.2) \\ \nabla' \cdot \mathbf{v}' &= 0. \end{aligned}$$

The dimensionless number

$$Re = \frac{\varrho_m v_c l_c}{\eta} \qquad (2.3)$$

is called the Reynolds number which quantifies, how important inertial forces are compared to viscous forces.

In typical soft matter systems, the characteristic quantities entering the Reynolds number (2.3) are

$$l_c \approx 10^{-9} - 10^{-5}\ \mathrm{m} \qquad v_c \approx 10^{-9} - 10^{-5}\ \mathrm{m/s}$$
$$\varrho_m \approx 10^{3}\ \mathrm{kg} \cdot \mathrm{m}^{-3} \qquad \eta \approx 10^{-3}\ \mathrm{kg} \cdot \mathrm{m}^{-1} \cdot \mathrm{s}^{-1}.$$

Hence the Reynolds number is of the order of

$$Re \approx 10^{-12} - 10^{-4} \ll 1.$$

On the other hand, all the terms $\frac{\partial \mathbf{v}'}{\partial t'}$, $(\mathbf{v}' \cdot \nabla')\mathbf{v}'$, $\eta \nabla'^2 \mathbf{v}' - \nabla' p'$, and $\mathbf{f}'_{ext}$ in Eq. (2.2) are typically of the order of unity (see Ref. [23], Chap. 5.5). Therefore the left-hand side of Eq. (2.2) can be neglected. This leads to the Stokes equation (also known as creeping flow equation),

$$\begin{aligned} \nabla p(\mathbf{r}) - \eta \nabla^2 \mathbf{v}(\mathbf{r}) &= \mathbf{f}_{ext} \qquad (2.4) \\ \nabla \cdot \mathbf{v}(\mathbf{r}) &= 0. \qquad (2.5) \end{aligned}$$

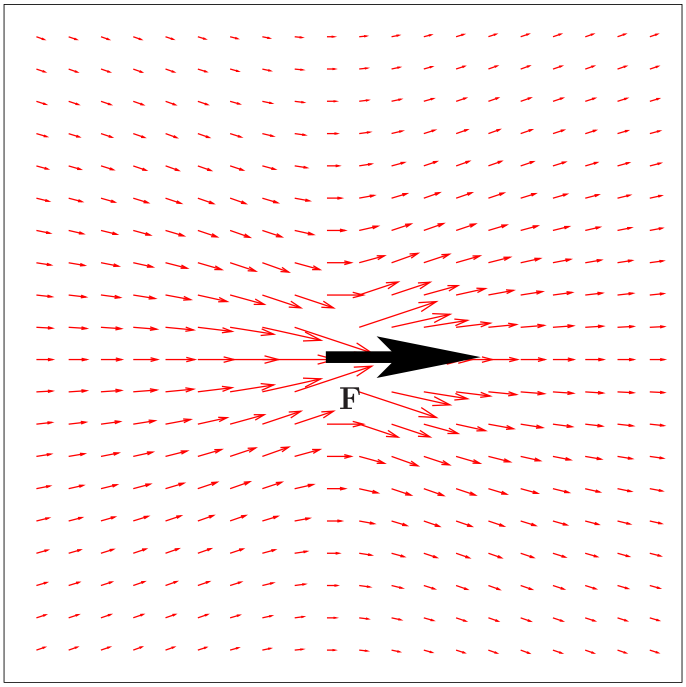

Figure 2.1: The velocity field $\mathbf{v}(\mathbf{r})$ due to a point force $\mathbf{F}$ can be calculated with the Oseen tensor (2.6).

This is a set of linear partial differential equations which can be solved by Green's functions. The corresponding Green's functions are the Oseen tensor [23]

$$\mathbf{T}_O(\mathbf{r}) = \frac{1}{8\pi\eta}\frac{1}{r}\left(\hat{\mathbf{I}} + \frac{\mathbf{r}\otimes\mathbf{r}}{r^2}\right) \tag{2.6}$$

and the pressure vector [23]

$$\mathbf{g}_O(\mathbf{r}) = \frac{1}{4\pi}\frac{\mathbf{r}}{r^3}. \tag{2.7}$$

Given an external point force $\mathbf{F}$, acting at position $\mathbf{r}'$, these Greens's functions relate $\mathbf{F}$ to a velocity

$$\mathbf{v}(\mathbf{r}) = \mathbf{T}_O(\mathbf{r}-\mathbf{r}')\cdot\mathbf{F}(\mathbf{r}') \tag{2.8}$$

and a pressure field

$$p(\mathbf{r}) = \mathbf{g}_O(\mathbf{r}-\mathbf{r}')\cdot\mathbf{F}(\mathbf{r}'). \tag{2.9}$$

The velocity field $\mathbf{v}(\mathbf{r})$, induced by an external point force, is shown in Fig. 2.1. Tensors coupling forces linearly to velocities like in Eq. (2.8) are generally called "mobility tensors". Thus, the Oseen tensor $\mathbf{T}_O(\mathbf{r})$ is the mobility tensor of the

Stokes equation (2.4). Later also other mobility tensors will be introduced, the isotropic $\mathbf{T}_s(\mathbf{r})$ and anisotropic screened mobility tensors $\mathbf{T}_a(\mathbf{r})$ (see Chap. 5). In order to make the different mobility tensors distinguishable, the mobility tensor $\mathbf{T}_O(\mathbf{r})$ (and also the pressure vector $\mathbf{g}_O(\mathbf{r})$) of the Stokes equation (2.4) is specified with the subscript "O". Subscripts are omitted in relations which generally hold for mobility tensors and which do not depend on the underlying hydrodynamic equation.

The velocity field $\mathbf{v}(\mathbf{r})$ and the pressure field $p(\mathbf{r})$ can be calculated for an arbitrary external body force $\mathbf{f}_{ext}(\mathbf{r}')$ by superposition,

$$\mathbf{v}(\mathbf{r}) = \int d\mathbf{r}'\mathbf{T}(\mathbf{r}-\mathbf{r}')\mathbf{f}_{ext}(\mathbf{r}') \tag{2.10}$$

$$p(\mathbf{r}) = \int d\mathbf{r}'\mathbf{g}(\mathbf{r}-\mathbf{r}')\cdot\mathbf{f}_{ext}(\mathbf{r}'). \tag{2.11}$$

Since $\mathbf{T}_O(\mathbf{r})$ decays like $1/r$, hydrodynamic interactions are very long-ranged. In Chap. 5, we will see that hydrodynamic interactions can be screened in crowded environments such that they are effectively short-ranged.

2.2 Colloidal systems

Particles are typically called colloids, if they are dispersed in a liquid environment and have linear sizes of 1 nm to 1 μm. As these particles are large compared to solvent molecules, the atomic details are of minor importance. In particular quantum effects are neglegible. However, colloidal particles are still small enough that effects of thermal fluctuations like Brownian motion play a significant role.

Many soft materials in real everyday life are colloidal systems. Examples are

Paints: Paints consist of small solid pigments immersed into a solvent (also called vehicle in paint chemistry). The pigment density determines the rheological properties of the paint and is optimized such that paint can be easily distributed on the substrate.

Milk: As milk contains many relatively rigid macromolecules, casein micelles, it has the properties of a colloidal system.

Gelatine: Gelatine is a composition of several proteins immersed in aqueous solution. This colloidal system forms thermally reversible gels in water with a gel-melting temperature below 36°, i.e. below body temperature

> [8]. This causes gelatin-based food to have its gel-like properties on the dish and a good flavour release in the mouth.

Also other soft matter object like proteins, star-like polymers [84], dendrimers [36] or vesicles (see Chap. 7) can be often regarded as (ultra-soft) colloids. In particular in biology, many objects have the properties of colloids. Among these are proteins [47, 92], protein aggregates (e.g. F-Actin filaments) or viruses. We will come back to these organic colloids below.

Far more important than the atomic details of colloids are other system properties like the shape of the colloids (e.g. spherical, rod-like or plate-like), the solvent viscosity and the way colloids interact with each other. The latter property is indeed the most complex, because it depends on many different mechanisms and parameters. For example, colloids are often charged, so that electrostatic interactions play a role. For uncharged colloids or charged colloids at high salt concentrations, direct steric interactions are crucial. Colloids are often highly deformable (e.g. star-like polymers [84]). The tendency of internal degrees of freedom to minimize free energy leads to entropic forces which can be described by an effective interaction potential between particles. Under certain circumstances, colloidal particles tend to aggregate. This can for example happen if surface sites on different particles bind to each other. In binary mixtures or colloid-polymer mixtures, also depletion interactions can cause aggregation [26, 27, 95]. Common for all kinds of colloidal systems is that particles interact hydrodynamically.

It is important to investigate the properties of colloidal model systems both theoretically and experimentally, in order to understand the behavior of such complex systems. Furthermore, colloidal systems are very useful toy models for statistical physicists. Like atoms, colloids can form a variety of interesting phases. Due to the large particle sizes and their slow dynamics, it is far easier to investigate colloidal model systems instead of atomic systems in a lab, because it is possible to image colloids with direct optical methods.

Many different kinds of colloidal model systems have been realized experimentally in the past. There are three common experimental approaches to produce colloidal particles. Inorganic nanostructures like tubes, rods, wires, and fibers are at the focus of research interest. The synthesis of these nanostructures is a big challenge because most inorganic materials do not form the desired structure by themselves, and also the control of particle sizes is not straightforward. The production of monodisperse inorganic colloids is an art by itself. Often used

inorganic colloids are silica [88], boehmite [12] or mineral particles [19].
Biological and organic materials usually have well-defined properties down to the nanoscale due to their genetic replication. If monodispersity is of high importance, it is convenient to use such particles. Examples of organic particles are the globular protein apoferritin [47, 92] or the rod-like *fd* virus [46, 47, 58, 61, 70, 93].
However, there are situations, where it is disadvantageous to use (bio)organic particles. Since all the particle properties are coded in genes, it is impossible to tune particle properties like sizes, shapes, rigidity, or charges independently.
A third experimental approach solves the disadvantage of fixed properties of organic colloids by combining both above mentioned classes of colloids. Organic colloids are often used as templates which are coated with inorganic material [96, 103, 104]. Such core-shell particles make it possible to take advantage of the well-defined shapes and sizes of the organic template particles with the additional option to modify particle properties like size, shape, charges or surface properties in a controlled way.

2.3 Rod-like colloids

In real life, there are many examples of rod-like structures in liquid environments. Most of them can be found in biology. In the cytoplasm, there are many filamentous components like microtubuli or F-actin (see e.g. Ref. [13], Chap. 7). In many cases, filaments are orientated isotropically (see Fig. 2.2.a) but in some situations they are directed (see Fig. 2.2.b) [16, 78]. In plants, cellulose fibres are crucial for providing stability. Also many viruses have rod-like shapes. Examples are the tobacco mosaic virus (see e.g. Ref. [2] and [13], Chap. 18) or the bacteriophage *fd* virus (see Fig. 2.3) [46, 47, 58, 61, 70, 93]. In order to learn about the properties of such systems, it is convenient to investigate simple colloidal model systems with a reduced complexity compared to real biological cells.

2.4 Phase behavior of rod-like colloids

Systems of rod-like colloids can form different thermodynamic phases. The phase behavior depends mainly on the volume fraction and the spatial extensions of the rods (lyotropic liquid crystals). For soft and flexible particles also tempera-

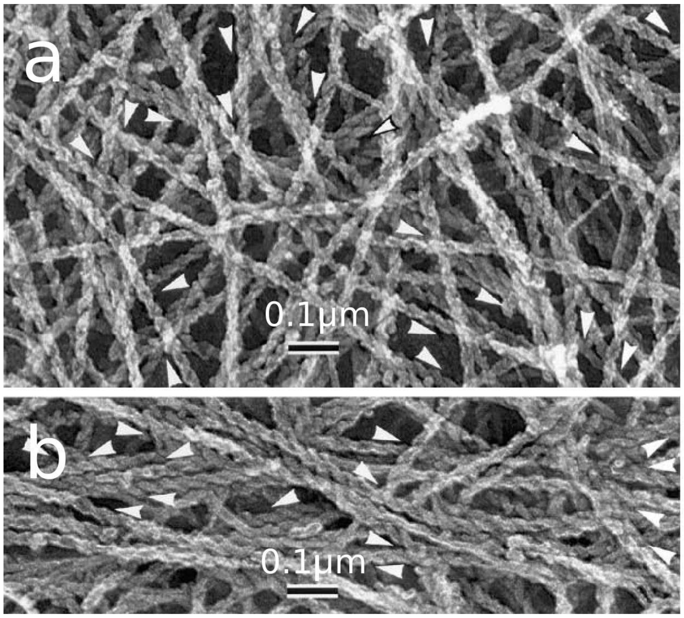

Figure 2.2: TEM-pictures of F-Actin networks in the fish epidermal keratocyte cytoskeleton (from Ref. [91]). In (a) filaments are aligned isotropically whereas (b) shows a region where one direction is preferred.

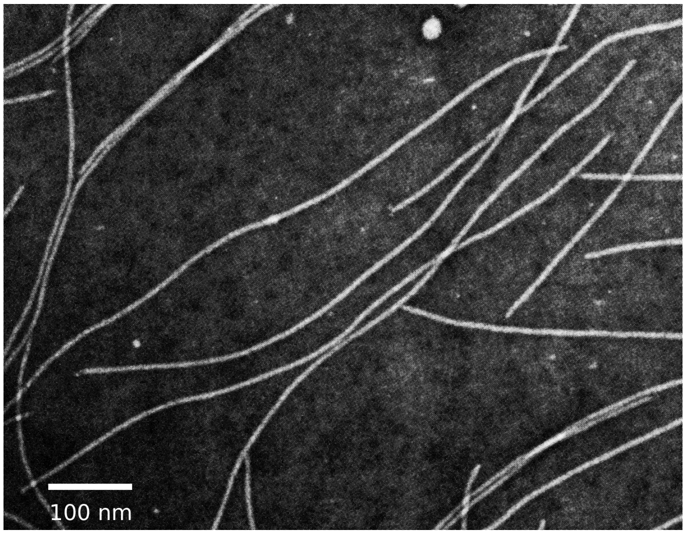

Figure 2.3: Bacteriophage *fd* viruses in the nematic phase (from Ref. [61])

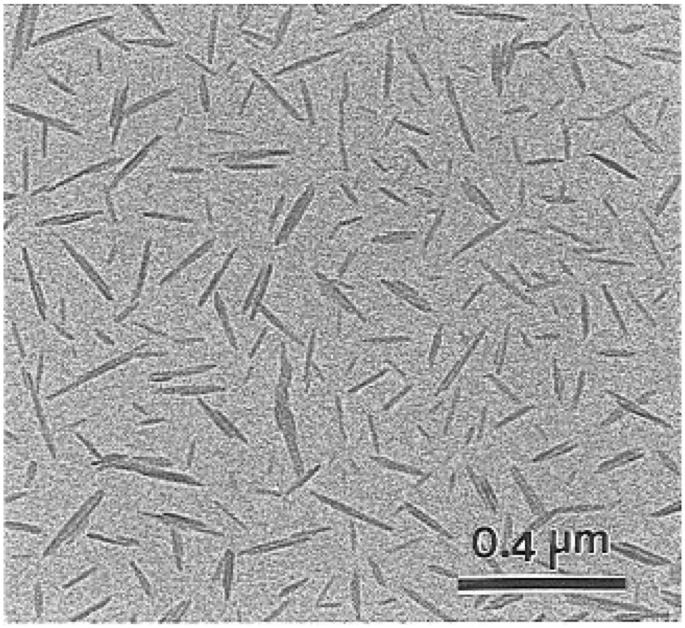

Figure 2.4: TEM picture of a dried suspension of cellulose crystallites prepared by sulfuric acid hydrolysis of cotton filter paper (from Ref. [29])

ture has an effect on the formation of phases (thermotropic liquid crystals). The static phase behaviour of rods has been studied intensively [26].

Onsager [77] was the first to explain the experimentally observed phase transition from an isotropic to a nematic state with increasing concentration. In the isotropic phase, rods are oriented completely randomly, whereas in the nematic phase, there is one preferred direction. This direction is represented by the unit vector

$$\hat{\mathbf{n}} = \frac{\langle \hat{\mathbf{u}} \rangle}{|\langle \hat{\mathbf{u}} \rangle|}, \tag{2.12}$$

called the nematic director. Here $\hat{\mathbf{u}}$ is the unit vector along the long axis of an individual rod. However, there is no positional order in the nematic phase. The degree of orientational ordering can be quantified by the nematic order parameter which is defined as

$$\langle P_2 \rangle = \frac{3}{2} \left\langle (\hat{\mathbf{u}} \cdot \hat{\mathbf{n}})^2 - \frac{1}{3} \right\rangle . \tag{2.13}$$

A nematic order parameter of $\langle P_2 \rangle = 1$ means perfectly aligned rods whereas in the isotropic phase $\langle P_2 \rangle = 0$. Onsager calculated the free energy for perfectly hard and rigid spherocylinders in a second virial approximation and predicted

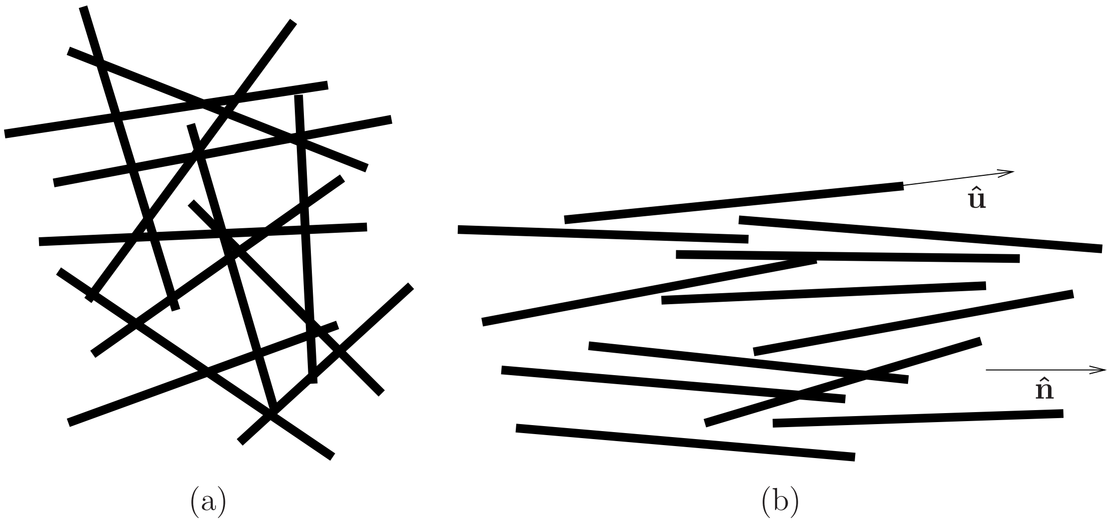

(a) (b)

Figure 2.5: Rod-like colloids (a) in the isotropic and (b) in the nematic phase.

that the volume fraction at the isotropic-nematic (I-N) transition is $\phi_{I-N} = 4d/L$ where d is the rod diameter and L the rod length. The volume fraction ϕ of a cylindrical rod with number density ϱ_{rods} is

$$\phi = \frac{1}{4}\varrho_{rods} d^2 L. \tag{2.14}$$

The quantity L/d is called the rod aspect ratio which is an important quantity for comparisons of simulations with theory or experiments. It is convenient to introduce the dimensionless concentration

$$\rho = \phi \frac{L}{d}, \tag{2.15}$$

since it has turned out that it is the critical parameter in most theories concerning lyotropic phase formations. By a more careful numerical calculation [15] it could be shown that there is a small coexistence region of nematic and isotropic phases where

$$\rho_I = 3.289 \qquad \text{and} \qquad \rho_N = 4.192 \tag{2.16}$$

are the volume fractions at coexistence of the isotropic and the nematic phases, respectively. This theory is exact in the limit of $L/d \to \infty$. There are several extensions which incorporate additional effects like flexibility [35, 51, 102] or electrostatic interactions [89]. A condensed but sufficiently detailed overview of the extensions to the Onsager theory can be found in Refs. [26, 98].

The rod overlap volume fraction ϕ^* is defined to be the volume fraction for which the average free volume of one rod is that of a sphere with a diameter L. For spherocylinders, the overlap volume fraction reads

$$\phi^* = \frac{3}{2}\left(\frac{d}{L}\right)^2 . \tag{2.17}$$

With the definition of ϕ^*, the mesh size ξ of a rod network can be defined,

$$\xi = L\sqrt{\frac{\phi^*}{\phi}}. \tag{2.18}$$

This quantity is a measure for the linear sizes of the “holes” in the network, which is important to judge whether particles in rod suspensions are able to diffuse out of its local environment or if they are trapped in a cage of other rods. For spherocylinders, the explicit expression of the mesh size is

$$\xi = d\sqrt{\frac{3}{2\phi}}. \tag{2.19}$$

Beside the two above mentioned phases, there are even more thermodynamically stable phases. For high concentrations, a smectic phase is favoured where in addition to orientational order rods also have positional order in the form of a stack of layers, where the rods are oriented parallel to the layer normal [26, 59]. Since the dynamics in smectic rod systems is too slow in order to be studied by computer simulations, this work only focuses on dynamics in isotropic and nematic systems.

2.5 Semiflexible rods

Many rod-like colloids, like the *fd* virus, are not perfectly stiff but slightly flexible. The flexibility of rods can be quantified by some (equivalent) quantities which are introduced in the following. An important property of semiflexible rod-like colloids is the bending rigidity κ which defines the energy cost per length for bending a rod such that it has a local curvature of $1/R$. In a continuum description, a semiflexible rod with length L can be parametrized by $\mathbf{r}(s)$, where s is distance between one end of the rod and site $\mathbf{r}(s)$ measured along the rod contour (see Fig. 2.6). Consequently, s equals zero at one end of the rod and L at the other. The bending energy of the whole rod is

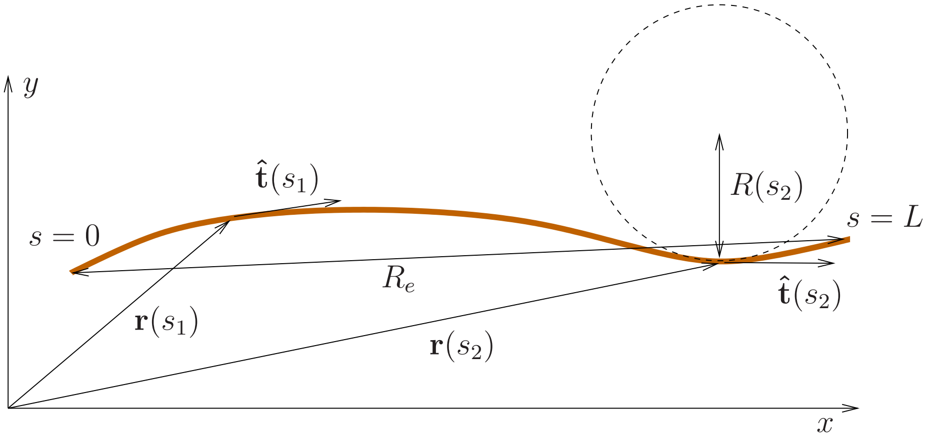

Figure 2.6: Important quantities for semiflexible rods.

$$U_{bend} = \frac{\kappa}{2} \int_0^L \left(\frac{\partial^2 \mathbf{r}}{\partial s^2} \right)^2 ds. \tag{2.20}$$

The tangential vector at a certain position of a rod is then

$$\hat{\mathbf{t}}(s) = \frac{\partial \mathbf{r}(s)}{\partial s}. \tag{2.21}$$

In thermal equilibrium, the correlation function $\left\langle \hat{\mathbf{t}}(0) \cdot \hat{\mathbf{t}}(s) \right\rangle$ depends on s like

$$\left\langle \hat{\mathbf{t}}(0) \cdot \hat{\mathbf{t}}(s) \right\rangle = \exp\left(-\frac{s}{l_p} \right), \tag{2.22}$$

where l_p is the persistence length. The persistence length l_p depends on κ by $l_p = \kappa/(k_B T)$. Alternatively, often the end-to-end distance R_e is used to quantify the semiflexibility. It is related to the persistence length l_p by

$$R_e^2 = 2 l_p \left\{ L - l_p \left[1 - \exp\left(-\frac{L}{l_p} \right) \right] \right\}. \tag{2.23}$$

2.6 Self diffusion

Diffusion is a spontaneous process which is the statistical outcome of random motion. Due to their thermal energy, Brownian particles always move with respect to the average velocity of its macroscopic environment. Collisions with solvent molecules change the trajectories of Brownian particles. After a certain time τ_B – the so called diffusive, Brownian, or Smoluchowski time scale – there

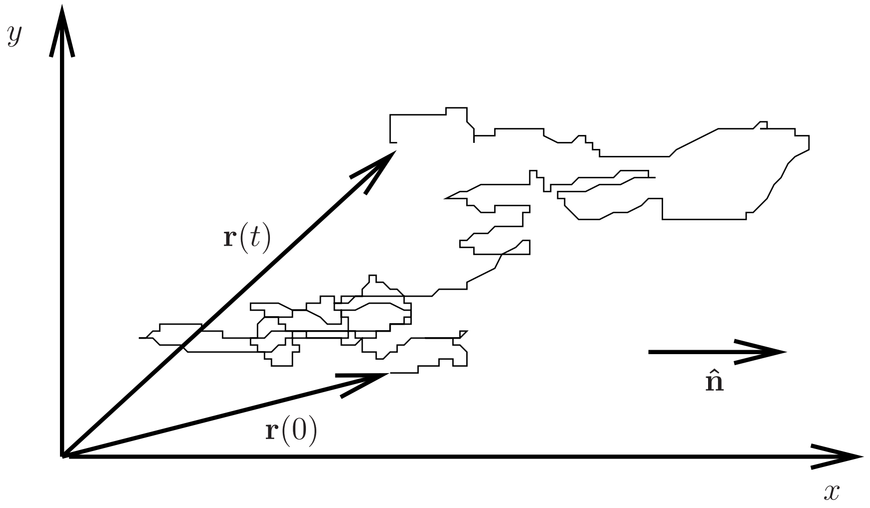

Figure 2.7: Trajectory of an anisotropically diffusing particle with $D_\parallel > D_\perp$.

are no memory effects any more, i.e. the motion of a Brownian particle is completely uncorrelated with its initial velocity. For a spherical colloid with radius a_s and mass M, the Brownian time is

$$\tau_B = \frac{M}{6\pi\eta a_s}. \tag{2.24}$$

τ_B is typically of the order of nanoseconds for micrometer sized colloids. Since there are no memory effects on the diffusive time scale, Brownian particles indeed perform a random walk and hence diffuse.
The mean square displacement (MSD) of a Brownian particle is defined by

$$W(t) := \left\langle (\mathbf{r}(t) - \mathbf{r}(0))^2 \right\rangle. \tag{2.25}$$

For diffusive motion, MSD increases linearly with time,

$$W(t) = \left\langle (\mathbf{r}(t) - \mathbf{r}(0))^2 \right\rangle = (2 \cdot d_{dim})Dt. \tag{2.26}$$

Here D is the so called diffusion constant. For the sake of generality, the dependence $(2 \cdot d_{dim})$ on the dimensionality d_{dim} is introduced.
However, in anisotropic (e.g. nematic) systems, diffusion depends on the direction of motion. Let us discuss the case of uniaxial anisotropy as in nematic systems. The colloid of interest (a rod among other rods or a sphere in rods) performs two independent random walks. A one-dimensional random walk in

the direction of the nematic director $\hat{\mathbf{n}}$ and a two-dimensional one in the two-dimensional subspace perpendicular to $\hat{\mathbf{n}}$. The diffusion constants are $D_\parallel$ and $D_\perp$ for parallel and perpendicular directions, respectively. The time dependence of mean square displacements $W_\parallel(t)$ and $W_\perp(t)$ is then

$$\begin{aligned} W_\parallel(t) &:= \left\langle (\mathbf{r}_\parallel(t) - \mathbf{r}_\parallel(0))^2 \right\rangle = 2D_\parallel t && (2.27) \\ W_\perp(t) &:= \left\langle (\mathbf{r}_\perp(t) - \mathbf{r}_\perp(0))^2 \right\rangle = 4D_\perp t. && (2.28) \end{aligned}$$

where $\mathbf{r}_\parallel(t) := (\hat{\mathbf{n}} \otimes \hat{\mathbf{n}})\mathbf{r}(t)$ and $\mathbf{r}_\perp(t) := (\hat{\mathbf{I}} - \hat{\mathbf{n}} \otimes \hat{\mathbf{n}})\mathbf{r}(t)$. Also in anisotropic systems, a three-dimensional diffusion constant D_{iso} can be defined – of course with the loss of information about the direction,

$$\begin{aligned} W(t) &= \left\langle (\mathbf{r}(t) - \mathbf{r}(0))^2 \right\rangle \\ &= \left\langle (\mathbf{r}_\parallel(t) - \mathbf{r}_\parallel(0))^2 \right\rangle + \left\langle (\mathbf{r}_\perp(t) - \mathbf{r}_\perp(0))^2 \right\rangle \\ &= W_\parallel(t) + W_\perp(t) = 2D_\parallel t + 4D_\perp t = 6D_{iso} t. && (2.29) \end{aligned}$$

From Eq. (2.29), we can directly identify the general relation

$$D_{iso} = \frac{1}{3}(D_\parallel + 2D_\perp). \tag{2.30}$$

Diffusion constants can be derived by statistical mechanics from microscopic interactions as it is nicely explained in Ref. [24].

Diffusion constants D of colloids are generally related to their friction constants γ by the Einstein relation [86]

$$D = \frac{k_B T}{\gamma}. \tag{2.31}$$

The friction constant γ of a colloid is defined by

$$\gamma = \frac{F}{v} \tag{2.32}$$

where F is the force which is necessary to pull the colloid with a velocity v through the surrounding media. The Einstein relation is an example of a fluctuation-dissipation relation. Hence it is equivalent to calculate friction constants and diffusion constants.

3 Methods

The relevant length scales in typical soft matter systems are mesoscopic, which means that they are significantly larger than the atomic scale, but still small enough that effects of thermal fluctuations like Brownian motion play a significant role. Typically this is the micrometer regime. These systems are difficult to simulate. Due to their complexity it is impossible to study them via the Navier-Stokes equations, and they are too large to treat each solvent molecule with Molecular Dynamics. Therefore, we use a novel simulation method which is called “Multi Particle Collision” (MPC) Dynamics. This method provides both hydrodynamic and thermodynamic properties which are essential for the dynamics in complex fluids. In the simulations, the dynamics of solute particles (colloids or vesicles), is solved by standard molecular dynamics (MD), whereas MPC is used to model the solvent. The combination of the MPC and the MD methods makes it possible to study long-time dynamics of colloids and vesicles.

3.1 Molecular Dynamics

We consider colloids and vesicles which are composed of point particles, called monomers. Their interaction is modelled by a combination of several potentials. Intra-particle potentials are used in order to maintain particle shapes, whereas repulsive inter-particle potentials are responsible for volume exclusion. The potential energy $\Phi(\mathbf{r}_1, ..., \mathbf{r}_N)$ of the whole system has to depend only on monomer positions. From this potential energy, the corresponding conservative force $\mathbf{F}_i$ acting on monomer i with position $\mathbf{r}_i$, mass m_i and velocity $\mathbf{v}_i$ can be calculated,

$$\mathbf{F}_i = -\nabla_{\mathbf{r}_i} \Phi(\mathbf{r}_1, ..., \mathbf{r}_N). \tag{3.1}$$

The potential $\Phi(\mathbf{r}_1, ..., \mathbf{r}_N)$ as well as the force $\mathbf{F}_i$ have to be continuous functions of the monomer positions. Otherwise energy conservation is violated. Although not used in our simulations, in principle also non-conservative forces can be used.

With the conservative forces (3.1), and given initial conditions $\mathbf{r}_i(t_0)$ and $\mathbf{v}_i(t_0)$, the Newtonian equation of motion

$$m_i \frac{d^2\mathbf{r}_i}{dt^2} = \mathbf{F}_i \tag{3.2}$$

is an initial value problem which can be solved numerically. There exist several iterative solvers for initial value problems [33]. Our choice is the Velocity Verlet algorithm [6] because of its good stability, low numerical costs and low memory requirement. In each iteration step, time is increased by a discrete time step h_{MD}, and positions $\mathbf{r}_i$ and velocities $\mathbf{v}_i$ are updated according to

$$\begin{aligned} \mathbf{r}_i(t+h_{MD}) &= \mathbf{r}_i(t) + h_{MD}\mathbf{v}_i(t) + \frac{h_{MD}^2}{2m_i}\mathbf{F}_i(t) && (3.3)\\ \mathbf{v}_i(t+h_{MD}) &= \mathbf{v}_i(t) + \frac{h_{MD}}{2m_i}\left(\mathbf{F}_i(t) + \mathbf{F}_i(t+h_{MD})\right) && (3.4) \end{aligned}$$

This time evolution is time reversible and accurate to an order of

$$\begin{aligned} \mathcal{O}\left(\left|\frac{d^3\mathbf{r}}{dt^3}\right| h_{MD}^3\right) &= \mathcal{O}\left(\left|\frac{d}{dt}\frac{d^2\mathbf{r}}{dt^2}\right| h_{MD}^3\right) && (3.5)\\ &= \mathcal{O}\left(\frac{1}{m}\left|\frac{d}{dt}\mathbf{F}\right| h_{MD}^3\right) = \mathcal{O}\left(\frac{1}{m}\left|\frac{d\mathbf{r}}{dt}\frac{\partial\mathbf{F}}{\partial\mathbf{r}}\right| h_{MD}^3\right) && (3.6)\\ &= \mathcal{O}\left(\frac{1}{m}\left|\frac{\partial^2\Phi}{\partial\mathbf{r}^2}\right| \cdot |\mathbf{v}|\, h_{MD}^3\right). && (3.7) \end{aligned}$$

The choice of a good time discretisation h_{MD} is important for the quality of the simulation. h_{MD} should be as large as possible in order save computation time, but on the other hand it has to be small enough to ensure energy conservation. Energy conservation is of particular importance in microcanonical equilibrium simulations like systems of rod-like colloids. Violating energy conservation would destroy time invariance, which has to hold in equilibrium. From Eq. (3.7) it can be seen, that the larger the typical curvature $\left|\frac{\partial^2\Phi}{\partial\mathbf{r}^2}\right|$ of the potential energy landscape and/or the larger the typical velocities $|\mathbf{v}|$, the smaller h_{MD} has to be. Since the potential-energy landscape is different for our different simulation systems, the time steps h_{MD} are chosen for each simulation individually by performing short test runs.

3.2 Multi Particle Collision Dynamics

Since we focus on hydrodynamic phenomena in several soft matter systems, a simulation technique is required which takes into account properly both hydrodynamic and thermodynamic effects of the solvent on the solute particles.

In the past, several simulation techniques for low Reynold number solvents have been developed. Among these are the widely used Lattice-Boltzmann [53, 54, 66] and the Dissipative Particle Dynamics (DPD) methods [32, 39, 41, 81]. A nice overview over the two above mentioned methods as well as the MPC method can be found in [80].

In the simulations presented below, the mesoscale, particle-based "Multi Particle Collision" (MPC) Dynamics algorithm is used for the solvent. The original version of this method was introduced by Malevanets and Kapral in 1999 [64]. In the following years, it has undergone several modifications and extensions. Among all these MPC versions, three are used in our simulations and hence explained below.

The MPC method was chosen because it has several advantages which makes it especially useful for our purpose. Since the MPC solvent is particle based, it directly incorporates fluctuations which are important in soft matter systems and even essential for the study of diffusion (see Chap. 4 and 6). Furthermore, it is numerically very efficient, easy to implement both in two and three dimensions, and the coupling between solvent and solute particles is straightforward. Further advantages are discussed in the following sections where the different MPC algorithms are explained.

3.2.1 MPC-SR

The "MPC-SR" method is used in the simulation of rod suspensions at equilibrium (see Chap. 4 - 6). The first three letters of this abbreviation stand for "Multi Particle Collision", and "SR" denotes "Stochastic Rotation". In literature, this method is also called Stochastic Rotation Dynamics (SRD), MPC or MPCD. Following the convention of Ref. [37], this method is called here "MPC-SR" in order to distinguish it from the other MPC solvents.

Except for the random shift, explained below, MPC-SR is the original version proposed by Malevanets and Kapral [64]. The solvent is composed of $N = V\varrho$ point particles. Here V is the volume of the simulation box, and ϱ is the number density of the point particles. These particles have mass m, continuous positions $\mathbf{r}_i$ $(1 \leq i \leq N)$ and continuous velocities $\mathbf{v}_i$. The time evolution of positions and velocities is discretized in small time steps h, the "collision time". In each time step, the dynamics of the MPC particles evolves in two steps.

Streaming step: All particles move ballistically for the "collision time" h according to their velocities. All particle positions $\mathbf{r}_i$ are then updated by

$$\mathbf{r}_i(t+h) = \mathbf{r}_i(t) + \mathbf{v}_i(t)h. \tag{3.8}$$

Since only positions are updated in the streaming step, kinetic energy and both linear and angular momentum are trivially conserved.

Collision step: All MPC particles are sorted into cubic "collision boxes" which partition the simulation volume. Each of the collision boxes has a linear size a, and the simulation volume has to have a cuboidal shape, such that each of the edges have lengths $L_{x,y,z} = n_{x,y,z}a$ ($n_{x,y,z} \in \mathbb{N}$) which is a multiple of a. The MPC particles are then sorted into the collision boxes according to their positions. For each box, all particle velocities are rotated by an angle α around a randomly chosen rotation axis in the center of mass system of the collision box. The velocities $\mathbf{v}_i$ are then updated by

$$\mathbf{v}_i(t+h) = \mathbf{v}_{cm}(t) + \mathcal{R}_\alpha(\hat{\mathbf{u}}_{ran})\left[\mathbf{v}_i(t) - \mathbf{v}_{cm}(t)\right] \tag{3.9}$$

where $\mathbf{v}_{cm}(t) = \mathbf{v}_{cm}(t+h)$ is the center of mass velocity of the box including particle i. $\mathcal{R}_\alpha(\hat{\mathbf{u}}_{ran})$ is a rotation matrix which performs the rotation of a vector by an angle α around the unit vector $\hat{\mathbf{u}}_{ran}$. In three-dimensional simulations, $\hat{\mathbf{u}}_{ran}$ is randomly taken from a unit sphere. In the two-dimensional case, $\hat{\mathbf{u}}_{ran}$ is chosen randomly from the two possibilities $\hat{\mathbf{u}}_{ran} = \pm\hat{\mathbf{z}}$, where $\hat{\mathbf{z}}$ is the out-off-plane unit vector. In contrast to the direction of the rotation axis, the angle α is fixed for the whole simulation. It has been shown that an angle of $\alpha = 130°$ in combination with a sufficiently small collision time $h \leq 0.1$ leads to a high Schmidt number (the Schmidt number is the ratio between viscous and diffusive momentum transport) and thereby to a fluid-like behavior [82, 83]. It can be easily shown that both kinetic energy and linear momentum are conserved also in the collision step [80]. However, angular momentum conservation is violated in the collision step, because the relative positions of the particles in a box do not enter into the calculation of the velocity update. This can lead to artifacts if the system has a preferred rotation direction [37]. The MPC-AT+a [74] method described in Sec. 3.2.3 avoids these problems.

In the original MPC method of Malevanets and Kapral [64], Galilei invariance is violated because the reference system of the collision box grid is fixed. In order to ensure Galilei invariance, Ihle and Kroll [42, 43] introduced a “random shift”. After each time increment, the collision box grid is shifted by a vector $\mathbf{b}$, whose components are randomly taken from a uniform distribution $b_{x,y,z} \in [0, a)$.

The system is generally initialized with uniformly randomly distributed particle positions $\mathbf{r}_i(t = 0)$ and with velocities $\mathbf{v}_i(t = 0)$ which are taken from a Maxwellian distribution with a width of $\sqrt{k_B T/m}$. Due to the momentum and kinetic energy conservation, a pure MPC-SR solvent in equilibrium is a microcanonical system which has an average temperature

$$\langle k_B T \rangle = \frac{2E_{kin}}{d_{dim}\, N} \tag{3.10}$$

Here $E_{kin} = \frac{m}{2} \sum v_i^2$ is the total kinetic energy, N the number of particles and d_{dim} is the dimensionality which can be either $d_{dim} = 2$ or $d_{dim} = 3$.

However, there are situations where the relation (3.10) does not hold. Often systems are not in equilibrium due to external fields or because of their initialization. Then additional thermostats are required in order to control temperature [11, 40]. In this case, the velocity-rescaling thermostat [11] is used boxwise. This thermostat works as follows. In each collision box, the thermal energy

$$E_{th} = \frac{m}{2} \sum_{i \in \text{box}} (\mathbf{v}_i - \mathbf{v}_{cm})^2 \tag{3.11}$$

is determined. Then the particle velocities in the center-of-mass system of the box are rescaled, such that the new thermal energy is $E'_{th} = \frac{d_{dim}}{2}(n-1)k_B T$ and momentum is conserved. The new particle velocities $\mathbf{v}'_i$ are then

$$\mathbf{v}'_i = \mathbf{v}_{cm} + (\mathbf{v}_i - \mathbf{v}_{cm}) \sqrt{\frac{E'_{th}}{E_{th}}}. \tag{3.12}$$

For the MPC-SR solvent, analytic expressions of the shear viscosity η were derived [44, 52]. The shear viscosity η has the two contributions η_{kin} and η_{coll}. The kinetic contribution η_{kin} arises from momentum transport by particle motion, and the collisional contribution η_{coll} originates from momentum transport due to collisions. The analytic expressions for the three-dimensional case are

$$\begin{aligned} \eta &= \eta_{kin} + \eta_{coll} && (3.13) \\ \eta_{coll} &= \frac{m(1-\cos\alpha)}{18ha}\left(\varrho a^3 - 1\right) && (3.14) \\ \eta_{kin} &= k_B T h \varrho \left(\frac{5\varrho}{(4 - 2\cos\alpha - 2\cos 2\alpha)(\varrho - a^{-3})} - \frac{1}{2} \right). && (3.15) \end{aligned}$$

For the two-dimensional expressions, see e.g. Ref. [52]. It can be easily seen that the viscosity η is dominated by the collisional contribution η_{coll} for small collision times h. The MPC-SR method was intensively tested in the recent years [4, 43, 52, 55, 56, 64]. The theoretical expression (3.13) for the shear viscosity can be compared with simulations. This is done in Sec. 5.3, where it can be seen that the theoretical expression (3.13) perfectly predicts the shear viscosity of all the simulations presented in Sec. 5.3.

All MPC versions can be easily used in hybrid MD-MPC simulations [65]. The coupling between solute and solvent particles is done by simply incorporating monomers into the collision step. The streaming step is only performed for the solvent particles. Also hybrid MD-MPC simulations have been carefully tested [69, 101]. For example, it was shown that polymer chains in MPC-SR solvent indeed show Zimm behavior, which has been predicted for polymers with hydrodynamically interacting monomers (see Refs. [101, 105], and [28], Chap. 4.2).

3.2.2 Random MPC solvent

The MPC-SR can be slightly modified to the "random MPC" solvent. Using this solvent, hydrodynamic interactions between monomers are switched off, but all thermodynamic solvent properties are the same as long as the same system settings are used. Simulations using the random MPC solvent are particularly useful in comparison with MPC-SR simulations. Since the only difference between both solvents is the absence of hydrodynamic interactions in the random MPC simulations, the effect of hydrodynamics in MPC-SR can be directly seen.

In the random MPC method, each monomer is related to a virtual collision box containing $n = \varrho a^{d_{dim}}$ virtual particles. The velocity components $v_{x,y,z}$ of these virtual particles should be distributed according to a Maxwellian distribution with a width of $\sqrt{\left\langle v_{x,y,z}^2 \right\rangle} = \sqrt{k_B T/m}$ and a mean $\langle v_{x,y,z} \rangle = 0$. In practice, an equivalent description is used, where the n virtual particles are replaced by only one virtual cluster particle with mass $m_{box} = mn$, whose velocity components $v_{box_{x,y,z}}$ are taken from an Maxwellian distribution with zero mean and a smaller width of $\sqrt{\left\langle v_{box_{x,y,z}}^2 \right\rangle} = \sqrt{\left\langle v_{x,y,z}^2 \right\rangle}/\sqrt{n}$. The collision step is then performed like in the MPC-SR solvent. The monomer velocity $\mathbf{v}_i$ is rotated by the fixed collision angle α around a random direction in the center of mass system of its virtual box. Thus the velocity update is

$$\mathbf{v}_i(t+h) = \mathbf{v}_{cm}(t) + \mathcal{R}_\alpha(\hat{\mathbf{u}}_{ran})\left[\mathbf{v}_i(t) - \mathbf{v}_{cm}(t)\right] \tag{3.16}$$

where the center of mass velocity $\mathbf{v}_{cm}(t) = \mathbf{v}_{cm}(t+h)$ is calculated by

$$\mathbf{v}_{cm}(t) = \frac{\mathbf{v}_i(t)m_i + \mathbf{v}_{box}(t)m_{box}}{m_i + m_{box}}. \tag{3.17}$$

The difference between random MPC and MPC-SR solvents is that in random MPC, the monomer always feels a friction force relative to the resting frame, whereas in MPC-SR, the friction forces are related to the velocity of the local solvent environment. Since the convectional flow velocity in the vicinity of a monomer is typically similar to the monomer velocity, the friction forces are often smaller in the presence of hydrodynamic interactions. Therefore, the dynamics of hydrodynamically interacting particles is typically faster.

As the friction forces in the random MPC solvent make the monomers always stick to the resting frame, Galilei invariance is of course violated. Also momentum and energy is not conserved. On the other hand, random MPC directly serves as a thermostat, because the thermal velocities of the virtual particles are taken from a Maxwellian distribution according to a particular temperature.

Although there is no flow in a random MPC solvent, its shear viscosity η can be of interest because it is for example important for the calculation of friction and diffusion constants. The shear viscosity of the random MPC solvent can be calculated by the same expressions (3.13 - 3.15) as in the case of MPC-SR.

3.2.3 MPC-AT+a

The violation of local angular-momentum conservation in the MPC-SR solvent can lead to problems, if the system has a preferred rotation direction. Götze, Noguchi and Gompper [37] could show that unphysical torques appear in Couette flow, where two concentric cylinders rotate with same angular velocity.

Also in shear flow, there is a preferred rotation direction, since shear flow is composed of an elongational and an rotational part (see Sec. 7.1.2). For the study on vesicles in shear flow (see Chap. 7) it is therefore essential to use an angular-momentum conserving solvent. This led to the development of another MPC version, called MPC-AT+a by Noguchi, Kikuchi and Gompper [74]. The abbreviation MPC-AT+a stands for "Multi Particle Collision with Andersen Thermostat", and "+a" emphasizes that angular momentum is conserved locally – in contrary to a similar method MPC-AT-a [74], where only linear-momentum conservation holds.

The differences between MPC-SR and MPC-AT+a only appear in the collision step. The streaming step and also the way how MPC particles are sorted into boxes are the same as in MPC-SR. The collision rule (3.9) of MPC-SR is replaced by

$$\mathbf{v}_i(t+h) = \mathbf{v}_{cm}(t)+\mathbf{v}_i^{ran}-\sum_{j\in\text{cell}}\frac{\mathbf{v}_j^{ran}}{N_c}-m\Pi^{-1}\sum_{j\in\text{cell}}\left[\mathbf{r}_{j,c}(t)\times\left(\mathbf{v}_j(t)-\mathbf{v}_j^{ran}\right)\right]\times\mathbf{r}_{i,c}(t). \tag{3.18}$$

Here $\mathbf{v}_{cm}(t) = \mathbf{v}_{cm}(t+h)$ denotes the center of mass velocity of the box, N_c the number of particles in that box, $\mathbf{r}_{i,c}(t)$ are the particle positions relative to the center of mass of the box, Π is the moment-of-inertia tensor (in two-dimensional simulations it reduces to a scalar) and the $\mathbf{v}_i^{ran}$ are random velocities which are taken from a Maxwellian distribution with zero mean and a width corresponding to the desired temperature. Hence this solvent serves as a thermostat – called the Anderson thermostat [7]. Since the randomly chosen velocities $\mathbf{v}_i^{ran}$ generally change linear and angular momentum, two correction terms are required. The third term on the right-hand side of Eq. (3.18) substracts the linear momentum which arises from the random velocities $\mathbf{v}_i^{ran}$ and the forth term substracts the corresponding angular momentum. Thus linear and angular momentum conservation is restored.

There are also theoretical expressions for the shear viscosity of the MPC-AT+a solvent [74],

$$\eta = \eta_{kin} + \eta_{coll} \tag{3.19}$$

$$\eta_{kin} = \varrho k_B T h\left(\frac{\varrho}{\varrho - a^{-d_{dim}}} - \frac{1}{2}\right) \tag{3.20}$$

$$\eta_{coll} = \frac{m(\varrho a^{d_{dim}} - 1)}{12 a^{d_{dim}-2} h}. \tag{3.21}$$

The MPC-AT+a will be used in the two-dimensional simulations of vesicles under shear (see Chap. 7).

3.3 Boundary conditions

Depending on the physical problem different types of boundaries are encountered. In computer simulations, periodic, open, absorbing, reflecting or no-slip wall boundary conditions are commonly used. Each of these boundary conditions can be applied to each boundary independently.

Since system size in computer simulations is limited, it is difficult to investigate bulk behavior. A wide-spread technique to approximate bulk behavior even for a finite system is to use periodic boundary conditions. This technique has been used in many molecular dynamics and Monte Carlo simulations and is nicely explained in Ref. [6] and hence not explained here. Also the application to MPC simulations is straightforward.

No-slip wall boundary conditions describe the physical situation where the relative velocity between a wall and the fluid layer directly at the wall vanishes. These boundary conditions are far less used in computer simulations, and the realization in MPC simulations is very specific. If during the ballistic streaming step (3.8) the trajectory of a MPC particle crossed a wall, the particle is bounced back, i.e. its velocity is inverted in the rest frame of the possibly moving wall. In contrast, for slip boundary conditions only the component perpendicular to the wall is inverted. In Chap. 7, moving walls will be used in order to generate a linear shear flow.

It has turned out that MPC solvents still have a small slip even if MPC particles are bounced back [56]. In order to avoid this problem, Lamura et al. [56] have introduced "virtual wall particles" in MPC-SR simulations. This concept was also applied to the MPC-AT+a solvent [37] and will be used in the two-dimensional simulations of vesicles under shear. The incorporation of virtual particles works as follows. Collision boxes crossing a wall often contain less particles than in the bulk. Therefore, $N_{virt} =< N_c > -N_c$ virtual particles are added to the box, where n is the current number of MPC particles in the considered box, and $< N_c >= \varrho a^{d_{dim}}$ is the average number in a box in bulk. The velocities of the N_{virt} virtual particles are taken from a Maxwellian distribution with a mean equal to the wall velocity and a width according to the desired temperature $k_B T$. In practice, all the N_{virt} are replaced by one virtual cluster particle as it is done also in the random MPC solvent (see Sec. 3.2.2).

3.4 Units

For convenience, masses are expressed in units of MPC particle masses m, lengths in units of the collision box size a and energies in units of the system temperature $k_B T$. This convention is particularly useful, because most of the quantities expressed in these units are of the order of unity (in contrast to e.g. the thermal energy $k_B T = 1.38 \cdot 10^{-23} J/K$ in SI units). E.g. times are then expressed in units of $a\sqrt{m/k_B T}$ or viscosities in units of $\sqrt{k_B T m}/a^{d_{dim}-1}$.

4 Self diffusion of rods

4.1 Scientific Background

Since the diffusion constants are generally related to their friction constants γ by the Einstein relation (2.31), we are able obtain diffusion constants by deriving the corresponding friction constants.

In the following, we distinguish between two relevant rod diameters. The diameter d introduced in Sec. 2.4 is called the steric diameter. It is the diameter of the cylindrical volume which is excluded for other colloids. Static properties of rod suspensions, like phase transitions or nematic order parameters, depend on rod aspect ratios L/d. In our simulations, we set d by an excluded volume potential which will be explained below.

However, there is also an other diameter, called the hydrodynamic diameter d_{hyd} which determines the rod volume that is excluded for solvent particles. This quantity is important for hydrodynamic properties like diffusion constants. Without hydrodynamic correlations between different rod segments, the friction/diffusion constant of a single rod with an aspect ration L/d_{hyd} is simply

$$\gamma_0 = 3\pi\eta L \qquad \text{and} \qquad D_0 = \frac{k_B T}{3\pi\eta L} \tag{4.1}$$

(compare Eq. (2.31)). The derivation of this expression is straightforward. We model the rod according to the "shish-kebab model" (see Fig.4.1). In this de-

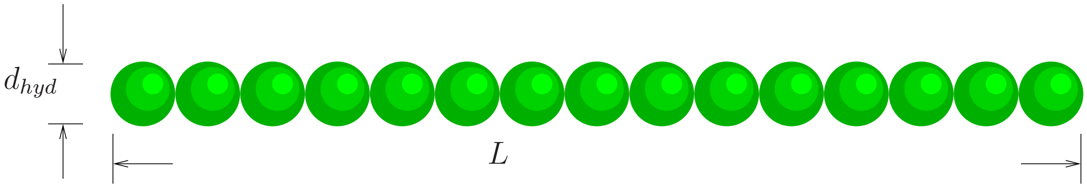

Figure 4.1: In the "shish-kebab model", a rod with an aspect ratio of L/d_{hyd} consists of $n = L/d_{hyd}$ spheres, each with a diameter d_{hyd}.

scription, the rod with an aspect ratio of L/d_{hyd} consists of $n = L/d_{hyd}$ spheres, each with a diameter d_{hyd}. These spheres are positioned on a line, such that they touch each other. The force required to pull the whole rod through the surrounding solvent is then n times the pulling force for a sphere with diameter d_{hyd}. It is known, that the friction constant γ_s and diffusion constant D_s of a sphere with diameter d_{hyd} are given by

$$\gamma_s = 3\pi\eta d_{hyd} \qquad \text{(Stokes friction)} \tag{4.2}$$

$$D_s = \frac{k_B T}{3\pi\eta d_{hyd}} \qquad \text{(Stokes diffusion).} \tag{4.3}$$

From this, we get directly $\gamma_0 = \gamma_s L/d_{hyd}$ and thus Eq. (4.1). In this calculation, it is assumed that all rod segments have to be pulled through a resting solvent. However, as soon as a rod is immersed into a solvent, its different rod segments interact hydrodynamically via the surrounding solvent. A rod segment moves into the same direction as the flow field induced by the other segments of the rod. Since friction forces are proportional to velocities relative to the surrounding fluid, a smaller force is required to pull the whole rod with a certain velocity if hydrodynamic interactions are present. Friction constants with hydrodynamic interactions are consequently smaller and the corresponding diffusion constants larger. This effect is called the "hydrodynamic enhancement" in the following.
Moreover, hydrodynamic interactions lead to anisotropic diffusion. Diffusion in the direction parallel to the rod is faster than in the perpendicular direction. Using the Oseen tensor approximation (2.6), the diffusion constants $D_\parallel$ and $D_\perp$ were calculated by Doi and Edwards (see Ref. [28], Chap. 8.3) in the limit of infinitely long rigid rods

$$D_\parallel = \frac{k_B T}{\gamma_\parallel} = \frac{k_B T \ln(L/d_{hyd})}{2\pi\eta L} \tag{4.4}$$

$$D_\perp = \frac{k_B T}{\gamma_\perp} = \frac{k_B T \ln(L/d_{hyd})}{4\pi\eta L}. \tag{4.5}$$

Comparing Eq. (4.4) and (4.5) with Eq. (4.1), shows, that diffusion is indeed faster in systems where hydrodynamic interactions are present.
For finite aspect ratios L/d_{hyd}, end effects lead to deviations from the diffusion constants (4.4) and (4.5) of the Doi-Edwards theory. Due to end effects, the exact geometric realization of the rod is crucial for a correct expressions of $D_\parallel$ and $D_\perp$. For spherocylinders, de la Torre et al. [21, 94] have calculated

additional correction terms to the Doi-Edwards theory

$$\begin{aligned} D_{\parallel} &= \frac{k_B T}{2\pi\eta L}\left[\ln\frac{L}{d_{hyd}} - 0.207 + 0.980\frac{d_{hyd}}{L} - 0.133\left(\frac{d_{hyd}}{L}\right)^2\right] && (4.6)\\ D_{\perp} &= \frac{k_B T}{4\pi\eta L}\left[\ln\frac{L}{d_{hyd}} + 0.839 + 0.185\frac{d_{hyd}}{L} + 0.233\left(\frac{d_{hyd}}{L}\right)^2\right] && (4.7)\\ D_{iso} &= \frac{k_B T}{3\pi\eta L}\left[\ln\frac{L}{d_{hyd}} + 0.312 + 0.565\frac{d_{hyd}}{L} - 0.100\left(\frac{d_{hyd}}{L}\right)^2\right] && (4.8) \end{aligned}$$

These diffusion constants provide a more precise description for the relatively small aspect ratios investigated here ($15 \leq L/d_{hyd} \leq 60$). In the limit of large aspect ratios, the expressions (4.6 - 4.8) of de la Torre et al. are equal to those of Doi and Edwards, Eqs. (4.4 - 4.5). For intermediate aspect ratios, the logarithmic term is dominating.

At finite rod concentrations, self-diffusion constants of rods are generally reduced for two reasons:

Steric interaction: Steric or direct repulsive interactions between rods ensure their volume exclusion. Due to steric interactions between neighbors, rods are hindered in their motion.

Hydrodynamic interactions: Even if two rods are not in direct contact, they can interact hydrodynamically via the solvent. The forces acting on one rod influence the flow field at the position of another rod and hence affect its diffusive behaviour.

The influence of steric interactions has been taken into account in other computer simulation studies [5, 18]. There is also an attempt to incorporate hydrodynamic effects into computer simulations [63] where the hydrodynamically caused diffusion anisotropy at infinite dilution (see Eqs. (4.6 - 4.8)) is transferred to dense rod systems by an anisotropic step size in Brownian-Dynamics simulations. However, hydrodynamic interactions with neighboring rods are neglected in Ref. [63]. All previous simulations give different or even contradicting predictions of diffusion constants. The reason is that diffusion constants depend very sensitively on the details of the model employed in the simulations.

In our computer simulations, we are able to take into account all (i.e. both inter and intra-colloidal) hydrodynamic interactions, because we simulate the solvent explicitly. There are no theories of translational rod-self diffusion at high concentrations which include hydrodynamic interactions. On the other hand, in real colloidal systems, hydrodynamic effects are always present. With computer simulations, we are able to bridge the gap between theory and experiments, because we can take into account the solvent explicitly using the MPC-SR method. For comparison, also simulations with same settings can be performed with the random MPC solvent, which does not mediate any hydrodynamic interactions between colloids. Thus, it is possible to compare simulations with and without hydrodynamics directly, and to distinguish between steric and hydrodynamic effects on colloid dynamics.

Of course, there is no easy way in experiments to simply switch off hydrodynamic interactions. On the first glance it might appear that it is even impossible to separate hydrodynamic from steric effects in experiments. However, our cooperation partner M. P. Lettinga of the experimental "Soft Matter" group of J. K. G. Dhont of the Research Center Jülich has developed a way to gradually tune the ratio of intra-rod to inter-rod hydrodynamic interactions [60]. Even if hydrodynamics cannot be switched off completely, one can approach to this situation. Our simulation data will be compared with the experimental results in Sec. 4.4.

4.2 Simulation details

We model rods by the "shish-kebab" model, see Fig. 4.1. A rod is composed of n point-like monomers, each of the same mass M.

The rods are not completely stiff but slightly flexible. This is in agreement with the experimental situation of the *fd*-virus, but it is also necessary in order to be handled by Molecular Dynamics. In Sec. 3.1, it was discussed that the MD time step has to be the smaller the more curved the potential energy landscape. Completely stiff rods correspond to δ-like potentials with an infinite curvature, i.e. there is no finite MD time step h_{MD} which can lead to stable simulations (see Eq. (3.7)).

When $\mathbf{r}_i$ denotes the position of the monomer i in the rod, we define the two adjacent bond vectors $\mathbf{R}_i^+ := \mathbf{r}_{i+1} - \mathbf{r}_i$ and $\mathbf{R}_i^- := \mathbf{r}_i - \mathbf{r}_{i-1}$. Two neighboring monomers are connected by a harmonic spring potential which controls the bond length. The spring potential U_{sp} for one rod is

$$U_{sp} = \frac{k_{sp}}{2} \sum_{i=1}^{n-1} (|\mathbf{R}_i^+| - l)^2 \tag{4.9}$$

where l is the equilibrium bond length and k_{sp} is the spring constant.

A bending potential U_{bend} provides stiffness to the rods. For one rod, this potential reads

$$U_{bend} = \frac{\kappa}{l^2} \sum_{i=2}^{n-1} (|\mathbf{R}_i^-| \, |\mathbf{R}_i^+| - \mathbf{R}_i^- \cdot \mathbf{R}_i^+), \tag{4.10}$$

where κ is the bending rigidity of the rod. This potential depends on the angle between the orientation of two neighboring bonds and has its minimum when both bonds have the same orientation.

For the stiffness of a rod, we require that the end-to-end distance of a single rod in thermal equilibrium is 98% of its contour length which corresponds to a persistence length of $l_p = 8.3L$. This determines κ for a given rod length L uniquely, which has to be calculated numerically as described in Sec. 3A of Ref. [100]. The *fd* virus used in experiments is slightly more flexible, with a persistence length of $l_p = 2.5L$. However, since the I-N phase transition is shifted to higher volume fractions with decreasing l_p/L (see [35, 102]), we decided to use comparably stiff rods in order to reach the nematic phase for smallest possible volume fractions.

U_{bend} has also a dependence on the bond lengths $|\mathbf{R}_i^-|$ and $|\mathbf{R}_i^+|$ which tends to contract the bonds if $\measuredangle\left(\mathbf{R}_i^-, \mathbf{R}_i^+\right) \neq 0$. We use this potential because of its numerical efficiency. However, this effect is very small for bending angles $\measuredangle\left(\mathbf{R}_i^-, \mathbf{R}_i^+\right) \ll 1$. With an equilibrium end-to-end distance of 98%, bending angles are so small that a contraction can be prevented by a sufficiently large spring constant k_{sp}. To ensure this, we set $k_{sp} = 4\kappa/l^2$ in our simulations. It should be mentioned that in vesicle simulations of Chap. 7, a less efficient bending potential is used, which does not have a bond-length dependence. This is necessary because far larger bending angles occur in vesicles.

In order to account for excluded volume interactions in dense rod suspensions, a shifted, truncated Lennard-Jones potential

$$U_{LJ}(r) = \begin{cases} 4\varepsilon \left[\left(\frac{\sigma}{r}\right)^{12} - \left(\frac{\sigma}{r}\right)^{6} \right] + \varepsilon, & r \leq \sqrt[6]{2}\sigma \\ 0, & \text{otherwise} \end{cases} \tag{4.11}$$

is applied between two monomers which are separated by a distance r.

In simulations of rod-like colloids, the MPC-SR and the random MPC solvents are used. The parameters used in our simulations are $h = 0.1a\sqrt{m/k_BT}$, $\alpha = 130°$, $\varrho = 10a^{-3}$, $l = a = d = \sqrt[6]{2}\sigma$, $M = 10m$, $h_{MD} = 0.005a\sqrt{m/k_BT}$ and $\varepsilon = 10k_BT$. We chose $M = \varrho a^3 m = 10m$ (m being the MPC particle mass) as it has been shown that for this value, the coupling between solvent and solute is optimal [83]. In Sec. 4.1, the hydrodynamic diameter d_{hyd} was defined as the diameter of the volume of a rod which is excluded for solvent particles. Since our simulation model does not repell MPC-SR particles from rods, there is no d_{hyd} in our simulations according to that definition. However, the MPC-SR method has the size a of the collision boxes as an intrinsic length which causes an effective hydrodynamic diameter d_{hyd}. d_{hyd} can be used in order to calculate diffusion or friction constants. According to Ripoll et al. [83], the diffusion constant D_p of one single rod monomer is in good approximation given by

$$D_p = \frac{k_BT}{M} h \left(\frac{3}{2} \frac{(m\varrho + M/a^3)}{m\varrho(1-\cos\alpha)} - \frac{1}{2} \right). \tag{4.12}$$

Inserting the parameters of our simulations, D_p agrees very well with the diffusion constant corresponding to the Stokes diffusion constant (4.3) with $d_{hyd} = a$. That this also holds for rods will be checked in Sec. 4.3, where diffusion constants of single rods are determined by simulations.

As explained in Sec. 2.4, rods are oriented isotropically for small dimensionless concentrations ρ, whereas above ρ_N (see Eq. (2.16)) a nematic phase is formed. The initialization of the rod system depends on whether an isotropic or a nematic phase is expected for the given dimensionless concentration ρ, Eq. (2.15), see Refs. [35, 102].

In order to minimize finite-size effects, the systems have to be sufficiently large. For isotropic systems, we chose cubic simulation boxes with linear sizes $L_x = L_y = L_z$ of slightly more then two rod lengths L. Rods are inserted by the following Monte Carlo scheme:

1. The center-of-mass position $\mathbf{r}_{cm}$ of the rod to be inserted is taken from a uniform random distribution $r_{cm,\alpha} \in [0, L_\alpha)$ with $\alpha \in \{x, y, z\}$.
2. The orientation $\hat{\mathbf{u}}$ of the rod is taken from a uniform distribution on a unit sphere.
3. According to $\mathbf{r}_{cm}$ and $\hat{\mathbf{u}}$, a trial insertion of a straight rod is done. The total potential energy cost E_{pot} due to overlaps with previously inserted rods is calculated.

4. A random variable x_{ran} is chosen from a uniform distribution $x_{ran} \in [0, 1)$.
5. If $\exp(-E_{pot}) > x_{ran}$, the trial insertion of the rod is accepted. Otherwise, we try to insert the rod at another position.

For nematic systems, we take advantage of the uniaxial anisotropy. Thus only in the direction of the nematic director $\hat{\mathbf{n}} = \hat{\mathbf{x}}$ the system has a linear size L_x slightly larger than $2L$, but the sizes of the other two dimensions (y and z) are only $L_y = L_z \approx L$. The insertion procedure is similar to that of isotropic systems, only step 2 differs, where the rod orientation is fixed to $\hat{\mathbf{u}} = \hat{\mathbf{n}} = \hat{\mathbf{x}}$.

When all rods are inserted, the system is of course still far from an equilibrium situation, because all intra-particle potentials U_{sp} and U_{bend} are at their minima. Therefore the system has to be equilibrated with the use of a thermostat. The thermostat is required to counteract the cooling caused by an increase of the potential energy due to the excitation of internal degrees of freedom. Since the static phase behavior of rods does not depend on hydrodynamics, it is convenient to use the random MPC solvent. This solvent has far lower numerical costs than MPC-SR, and it directly serves as a thermostat (see Sec. 3.2).

That the system is in equilibrium can be verified by monitoring the total potential energy and, in nematic systems, the nematic order parameter, until stable values are reached.

Equilibrated systems are taken as input configurations for MPC-SR or random MPC simulations of rods, from which data are recorded. Additionally, in the beginning of each simulation run, temperature is controlled by the velocity-rescaling thermostat, Eq. (3.12), over a short period of a few hundreds MPC time steps. The simulation continues under NVE conditions, and data recording is started after a further few hundreds MPC time steps. Monomer positions are written to files periodically in time intervals Δt. From this data, mean square displacement and other desired quantities can be obtained.

In order to determine long-time self-diffusion constants of rod-like colloids, rod positions have to be recorded over a time which has to be sufficiently long that the regime is reached, where the linear time dependence (2.26 - 2.28) of the mean square displacement holds, so that diffusion constants can be extracted with good accuracy. We will see in Sec. 4.4 that this regime is typically reached when the mean square displacement is of the order of L^2. The dependence of the required computational time on rod lengths L can be roughly estimated:

- The required computational time for one simulation time step is proportional to the volume of the system, which is proportional to L^3 (the linear system sizes L_x, L_y, and L_z were chosen to be proportional to L).

- Without hydrodynamic and network effects, the diffusion constant of a rod decreases like $1/L$.
- The required simulated time to reach a mean square displacement of L^2 also depends on rod length like L^2.

These three effects lead to computational times, which depends on rod lengths like L^6. Hence we are restricted to determine self-diffusion constants of rods with aspect ratios $L/d \leq 40$.

4.3 Single rods

In order to point out the influence of finite density of rod-like colloids on diffusion, also diffusion constants of rods at infinite dilution have to be determined. With single rods, we have the advantage that theoretical expressions exist both with hydrodynamic interaction [21, 94] between rod segments, Eq. (4.6 - 4.8), and without them, Eq. (4.1). Most of the quantities entering these theoretical expressions are given by the simulation parameters. These are the temperature k_BT, the rod length L and the solvent viscosity η. The latter can be calculated from Eq. (3.13). Furthermore, we choose all parameters, which should influence the diffusive behavior of single rod monomers, in such a way that the rod monomer diffusion constant D_p (see Eq. (4.12)) agrees with the diffusion constant D_0 (see Eq. (4.1)) corresponding to $d_{hyd} = d = a$.

These results can only be directly transferred to rod diffusion constants in random MPC solvents, because in this case $D_0 = \frac{D_p}{N}$. However, we have to confirm that $d_{hyd} = a$ by simulations of single rods. For this purpose, we performed several single-rod simulations for both kinds of solvents, the MPC-SR and the random MPC solvent.

We begin with simulations without HI, i.e. with the use of the random MPC solvent. For each of the rod aspect ratios $L/d = 15$, $L/d = 20$ and $L/d = 40$, six simulations are run, each over 10^7 MPC time steps.

The mean square displacement $W(t)$ is calculated according to Eq. (2.26). The average $\langle ... \rangle$ in Eq. (2.26) is calculated from all possible time differences between recorded monomer positions. With the total simulated time $t_{tot} = N_f \Delta t$ with N_f the number of recorded monomer configurations, the mean square displacement

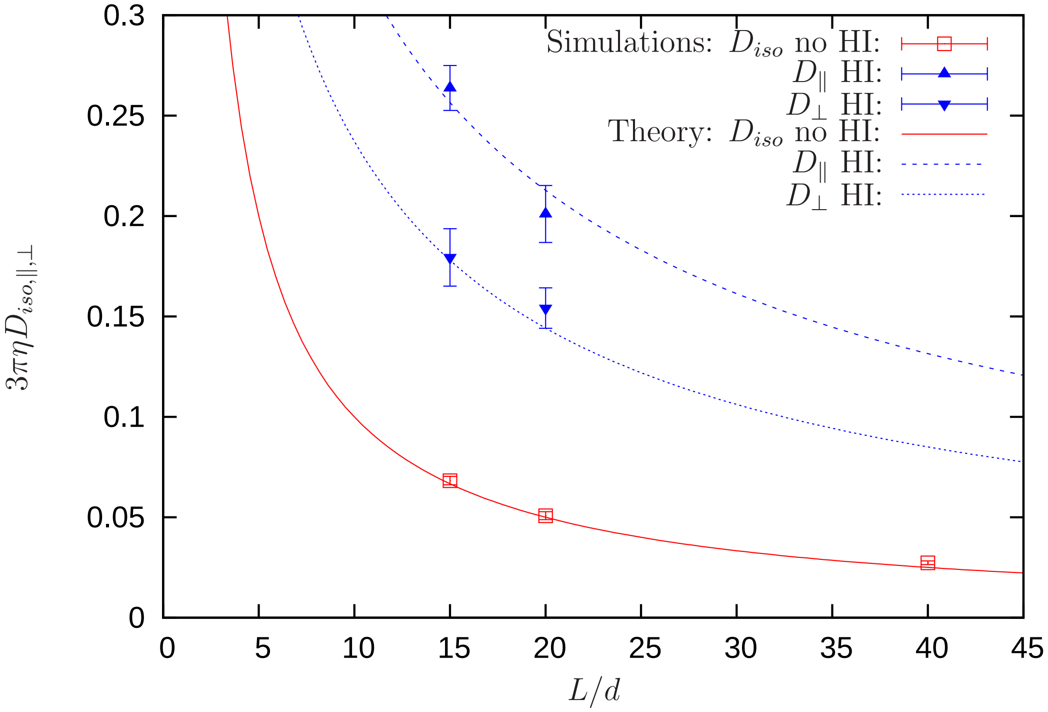

Figure 4.2: Simulation data and theoretical values for diffusion constants of single rods with $d_{hyd} = a$. Blue theoretical lines are calculated by Eqs. (4.6) and (4.7). The red theoretical line is calculated by Eq. (4.1). Simulation data are obtained from independent runs.

$W(t)$ is then calculated according to

$$W(t = j\Delta t) = \frac{1}{N_f - j} \sum_{i=0}^{N_f - j - 1} \left[\mathbf{r}_{cm}((j+i)\Delta t) - \mathbf{r}_{cm}(i\Delta t)\right]^2 . \qquad (4.13)$$

Since there are many time differences $j\Delta t$ available for $j \ll N_f$, the accuracy of $W(t = j\Delta t)$ is higher for small time differences. Particularly for single rod simulations, where we cannot average over different rods, many frames ($N_f \approx 10^4$) are required in order to get reasonable accuracy for time differences up to $t \approx 50\Delta t$. The resulting diffusion constants D_0 are shown in Fig. 4.2 (red open squares). Also the theoretical curve corresponding to Eq. (4.1) with $d_{hyd} = a$ is plotted without adjustable parameters (red solid line). We conclude from these results that $d_{hyd} = a$ is a very good estimate of the effective hydrodynamic diameter. In the following we will use the expression (4.1) with $d_{hyd} = a$ whenever infinite dilution diffusion constants of rods without hydrodynamic interactions are needed.

In contrast to random MPC, the MPC-SR solvent takes also into account hydrodynamics. Accordingly, an anisotropy in diffusion should be seen even at infinite dilution (see expressions (4.6 - 4.8)). Unfortunately, such simulations are very time consuming, since the dynamics of $N = \varrho V$ additional MPC particles has to be calculated. To avoid hydrodynamic interactions with the periodic images, a sufficiently large simulation box is required. Winkler et al. [101] did a systematic study of the length dependence of total rod diffusion constants D_{iso} in MPC-SR. They could show that their simulations are in good agreement with the theoretical description for box sizes $L_x = L_y = L_z \gtrsim 2L$. Therefore, we decided to use the same rod-length dependent system sizes for our single-rod simulations. We chose rods with $L/d = 15$ and $L/d = 20$ and performed four simulations for each of the two aspect ratios over 10^6 MPC time steps. Larger aspect ratios are computationally not feasible.

In Sec. 2.6, the diffusion constants $D_\parallel$ and $D_\perp$ were shown to be related to the mean square displacements $W_\parallel(t)$ and $W_\perp(t)$ by Eqs. (2.27) and (2.28), respectively. For single rods, the calculation of $W_\parallel(t)$ and $W_\perp(t)$ is not straightforward, as a rod undergoes also rotational diffusion, and the direction of the rod axis $\hat{\mathbf{u}}$ changes during the simulation. Reasonable mean-square-displacement curves $W_\parallel(t)$ and $W_\perp(t)$ in a co-rotating frame can be obtained by the following procedure. The time Δt between two consecutive frames has to be short enough that the change in rod orientation $\hat{\mathbf{u}}(t + \Delta t) - \hat{\mathbf{u}}(t)$ is small. Then the translational displacement $\mathbf{r}_{cm}(t+\Delta t) - \mathbf{r}_{cm}(t)$ of the center of mass of the rod is transformed into a co-rotating frame S' by

$$\mathbf{r}'_{cm}(t + \Delta t) - \mathbf{r}'_{cm}(t) = \mathcal{R}_{\hat{\mathbf{u}}(t)\to\hat{\mathbf{x}}} \left[\mathbf{r}_{cm}(t + \Delta t) - \mathbf{r}_{cm}(t)\right]. \tag{4.14}$$

In the co-rotating frame S', the $\hat{\mathbf{x}}$ direction corresponds to the $\parallel$ direction and the yz plane correspond to the plane perpendicular to the rod axis. The rotation matrix $\mathcal{R}_{\hat{\mathbf{u}}\to\hat{\mathbf{x}}}$ is defined by

$$\mathcal{R}_{\hat{\mathbf{u}}\to\hat{\mathbf{x}}} = \begin{pmatrix} u_x & u_y & u_z \\ -u_y & \frac{u_x u_y^2 + u_z^2}{u_y^2 + u_z^2} & (u_x - 1) u_y u_z \\ -u_z & (u_x - 1) u_y u_z & \frac{u_x u_z^2 + u_y^2}{u_y^2 + u_z^2} \end{pmatrix} \tag{4.15}$$

which rotates a vector around the axis parallel to $\hat{\mathbf{x}} \times \hat{\mathbf{u}}$ such that $\mathcal{R}_{\hat{\mathbf{u}}\to\hat{\mathbf{x}}}\hat{\mathbf{u}} = \hat{\mathbf{x}}$. There are several possibilities how to define the unit vector $\hat{\mathbf{u}}$ for a semiflexible rod. Our convention is the following. We calculate the gyration tensor of the rod

$$\mathbf{G} = \sum_{i=1}^{N} (\mathbf{r}_i - \mathbf{r}_{cm}) \otimes (\mathbf{r}_i - \mathbf{r}_{cm}), \tag{4.16}$$

where the $\mathbf{r}_i$ are the monomer positions. $\hat{\mathbf{u}}$ is then that normalized eigenvector of $\mathbf{G}$ with the largest eigenvalue $\Lambda_\parallel$,

$$\mathbf{G}\hat{\mathbf{u}} = \Lambda_\parallel \hat{\mathbf{u}}. \tag{4.17}$$

With this definition of $\hat{\mathbf{u}}$, we are also able to calculate nematic order parameters $\langle P_2 \rangle$ in multi-rod systems by Eq. (2.13).
Thus the trajectory $\mathbf{r}'_{cm}(t)$ in the co-rotating frame S' is

$$\mathbf{r}'_{cm}(t = j\Delta t) = \sum_{i=0}^{j-1} \mathcal{R}_{\hat{\mathbf{u}}(i\Delta t) \to \hat{\mathbf{x}}} \left[\mathbf{r}_{cm}\left((i+1)\Delta t\right) - \mathbf{r}_{cm}\left(i\Delta t\right)\right]. \tag{4.18}$$

With these $\mathbf{r}'_{cm}(t)$, the mean square displacements $W_\parallel(t)$ and $W_\perp(t)$ are calculated according to Eqs. (2.27) and (2.28). In practice, the average appearing in Eqs. (2.27) and (2.28) is calculated analogously to Eq. (4.13),

$$W_{\parallel,\perp}(t = j\Delta t) = \frac{1}{N_f - j} \sum_{i=0}^{N_f - j - 1} \left[\mathbf{r}'_{cm_{\parallel,\perp}}((j+i)\Delta t) - \mathbf{r}'_{cm_{\parallel,\perp}}(i\Delta t) \right]^2 \tag{4.19}$$

with $\mathbf{r}'_{cm_\parallel}(t) := (\hat{\mathbf{x}} \otimes \hat{\mathbf{x}})\mathbf{r}'_{cm}(t)$ and $\mathbf{r}'_{cm_\perp}(t) := (\hat{\mathbf{I}} - \hat{\mathbf{x}} \otimes \hat{\mathbf{x}})\mathbf{r}'_{cm}(t)$. In Fig. 4.2, the simulation results are shown together with the theoretical curves according to Eqs. (4.6 - 4.8). Within error bars, the few data points for MPC-SR simulations agree with Eqs. (4.6 - 4.8). The anisotropic single rod diffusion constants confirm that hydrodynamics is obviously reproduced by MPC-SR simulations and that $d_{hyd} \approx a$ is a reasonable value for the hydrodynamic diameter. This fact allows us to use the expressions (4.6 - 4.8) of de la Torre et al. [21, 94] for the infinite dilution values of diffusion constants.

4.4 Dense rod suspensions

We have performed a systematic study for $L/d = 20$ and $L/d = 40$ in order to follow the concentration dependence of rod self-diffusion constants $D_{iso,\parallel,\perp}$. In Fig. 4.3, two snapshots of such rod systems are shown. Fig. 4.3.a shows a system in the isotropic phase, and Fig. 4.3.b a system in the nematic phase.

The dependence of the nematic order parameter $\langle P_2 \rangle$ on the normalized volume fraction ρ in our computer simulations is shown in Fig. 4.4 for both aspect ratios. All data falls on a master curve $\langle P_2 \rangle (\rho)$, independent of the aspect ratios.
Self-diffusion constants $D_{iso,\parallel,\perp}$ were calculated from mean square displacements defined by Eqs. (2.26), (2.27) and (2.28). In practice, the averages in expressions (2.26) - (2.28) for the mean square displacements are calculated similarly to the case of single rods, but taking advantage of having N rods. Since the amount of rods in our simulations is of the order of $10^2 < N < 10^3$, the accuracy of the mean square displacement $W(t = j\Delta t)$ is typically sufficient for fitting diffusion constants for times $t = j\Delta t \lesssim \frac{3}{4} t_{tot}$.
In Fig. 4.5, examples of typical mean-square-displacement curves for isotropic and nematic systems are shown. We see that the time dependence of $W_{iso,\parallel,\perp}(t)$ is linear for these simulations. Only for very long times, data points deviate from the expected linear behavior, because for $t \gtrsim t_L$ statistics is not sufficient. The regime of linear dependence, the long-time diffusive regime, has to be reached in order to fit diffusion constants. It has turned out that for $t_{tot} \approx t_L$ most simulations have reached the long-time diffusive regime.
Fig. 4.6 shows the concentration dependence of rod self-diffusion constants D_{iso}, $D_\parallel$ and $D_\perp$ for the two aspect ratios $L/d = 20$ (Fig. 4.6.a) and $L/d = 40$ (Fig. 4.6.b). For both aspect ratios, results of simulations with MPC-SR (i.e. with HI) and with random MPC solvents (i.e. without HI) are shown. Diffusion constants are normalized by the infinite dilution value (4.1) of rods in absence of hydrodynamic interactions. Thus, the curves without HI have to extrapolate to unity in the limit $\rho \to 0$.
Several interesting conclusions can be drawn from Fig. 4.6. For nematic systems, there is a strong anisotropy in diffusion, with higher parallel diffusion constant, $D_\parallel$, than perpendicular, $D_\perp$. In contrast to infinite dilution, this anisotropy can even be found in systems without any hydrodynamic interactions. Accordingly, steric interactions with the rod network cause an anisotropy in diffusion. We will discuss the diffusion anisotropy in detail in Sec. 4.4.2.

4.4.1 Hydrodynamic enhancement

From Fig. 4.6, we see that diffusion constants in the presence of hydrodynamic interactions are generally larger. Obviously, the hydrodynamic enhancement is still present even in very dense systems. In Sec. 4.1, it was discussed that

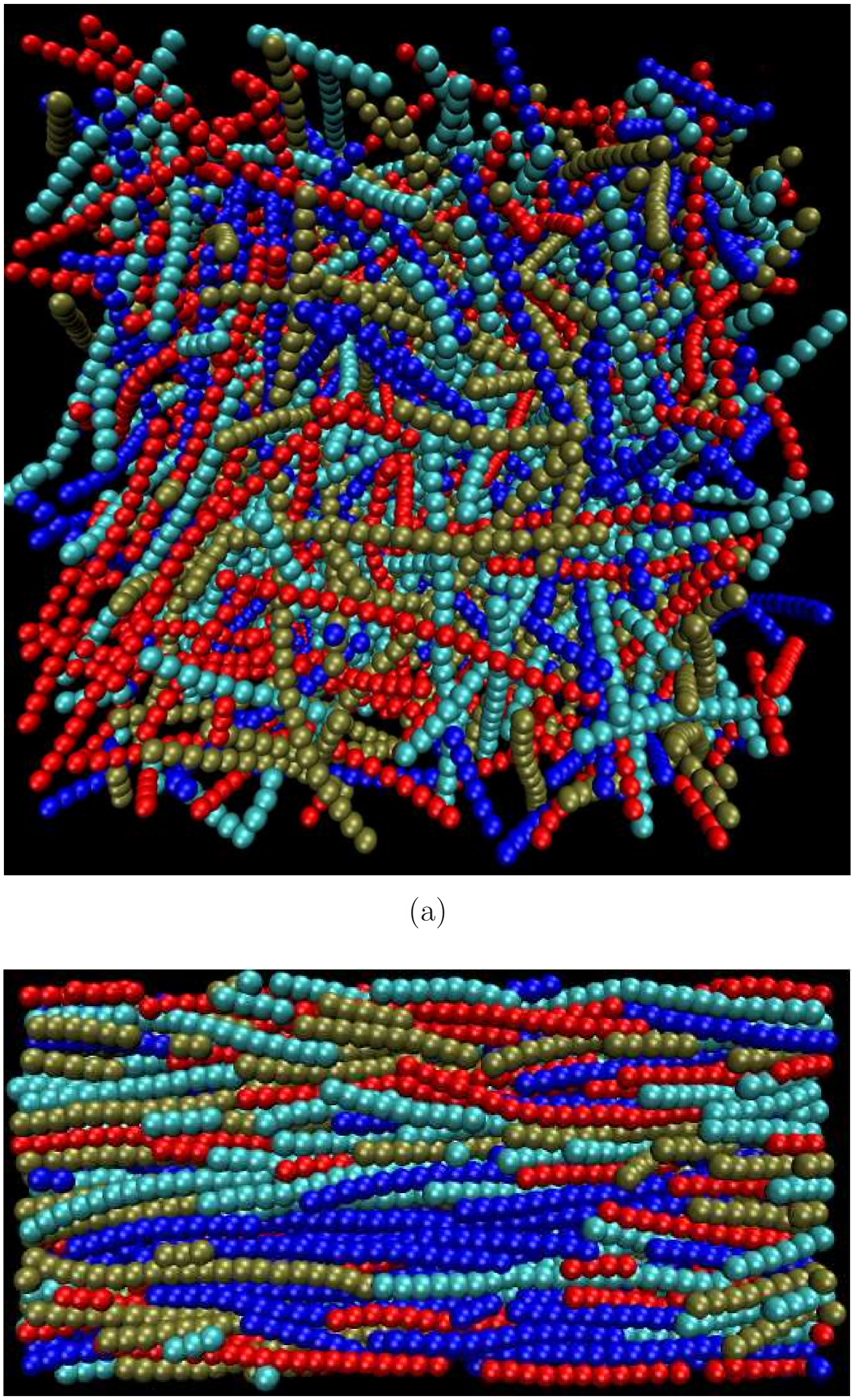

(a)

(b)

Figure 4.3: Snapshots of rod systems with $L/d = 20$ in (a) the isotropic phase ($\phi = 0.12$) and (b) the nematic phase ($\phi = 0.27$).

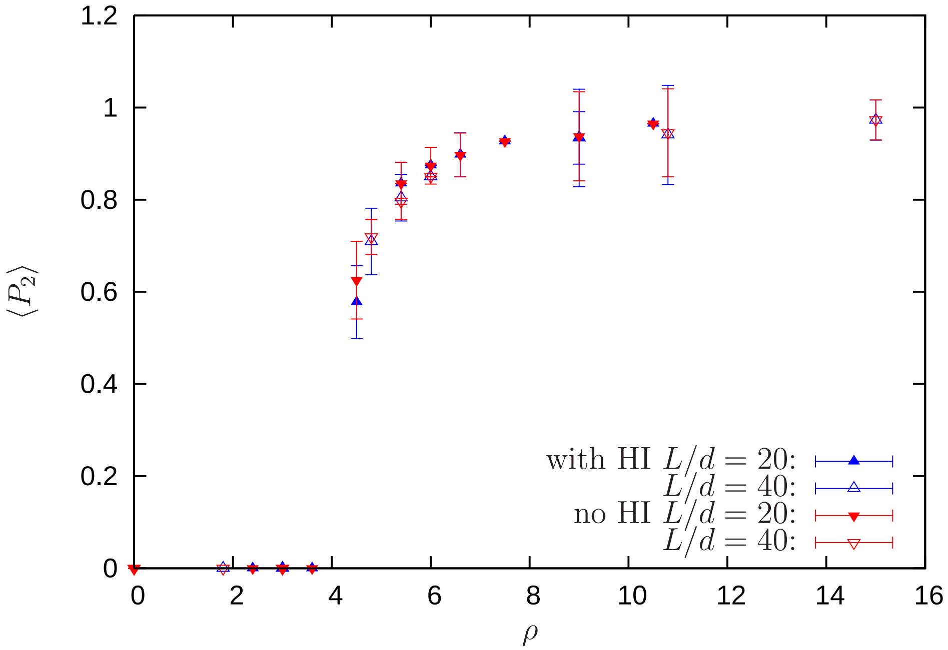

Figure 4.4: The dependence of the nematic order parameter $\langle P_2 \rangle$ on the normalized volume fraction ρ for aspect ratios $L/d = 20$ and $L/d = 40$.

the hydrodynamic enhancement of single rods arises from hydrodynamic interactions between different parts of the rod. Since in MPC-SR simulations all hydrodynamic interactions are present – also those with rod segments of other rods, hydrodynamic enhancement is expected to be diminished with increasing concentration. Hydrodynamic interactions with neighboring rod monomers can be therefore stronger than the interaction of two different monomers of one rod which are far apart. Therefore we expect that rod diffusion in MPC-SR solvents is slowed down not only due to steric effects, but also due to hydrodynamic friction with neighboring rods. Diffusion constants

$$\widehat{D}_{iso,\|,\perp}(\rho) := \frac{D_{iso,\|,\perp}(\rho)}{D_{iso}(0)} \tag{4.20}$$

normalized by the values at infinite dilution $D_{iso}(0)$ are shown in Fig. 4.8.a for $L/d = 20$. The infinite-dilution diffusion constants $D_{iso}(0)$ are calculated from Eq. (4.8) for MPC-SR systems. For random MPC systems, D_0 (see Eq. (4.1)) is used. In this representation, the non-hydrodynamic curves lie above the corresponding hydrodynamic curves – as well in the isotropic as in the nematic phase.

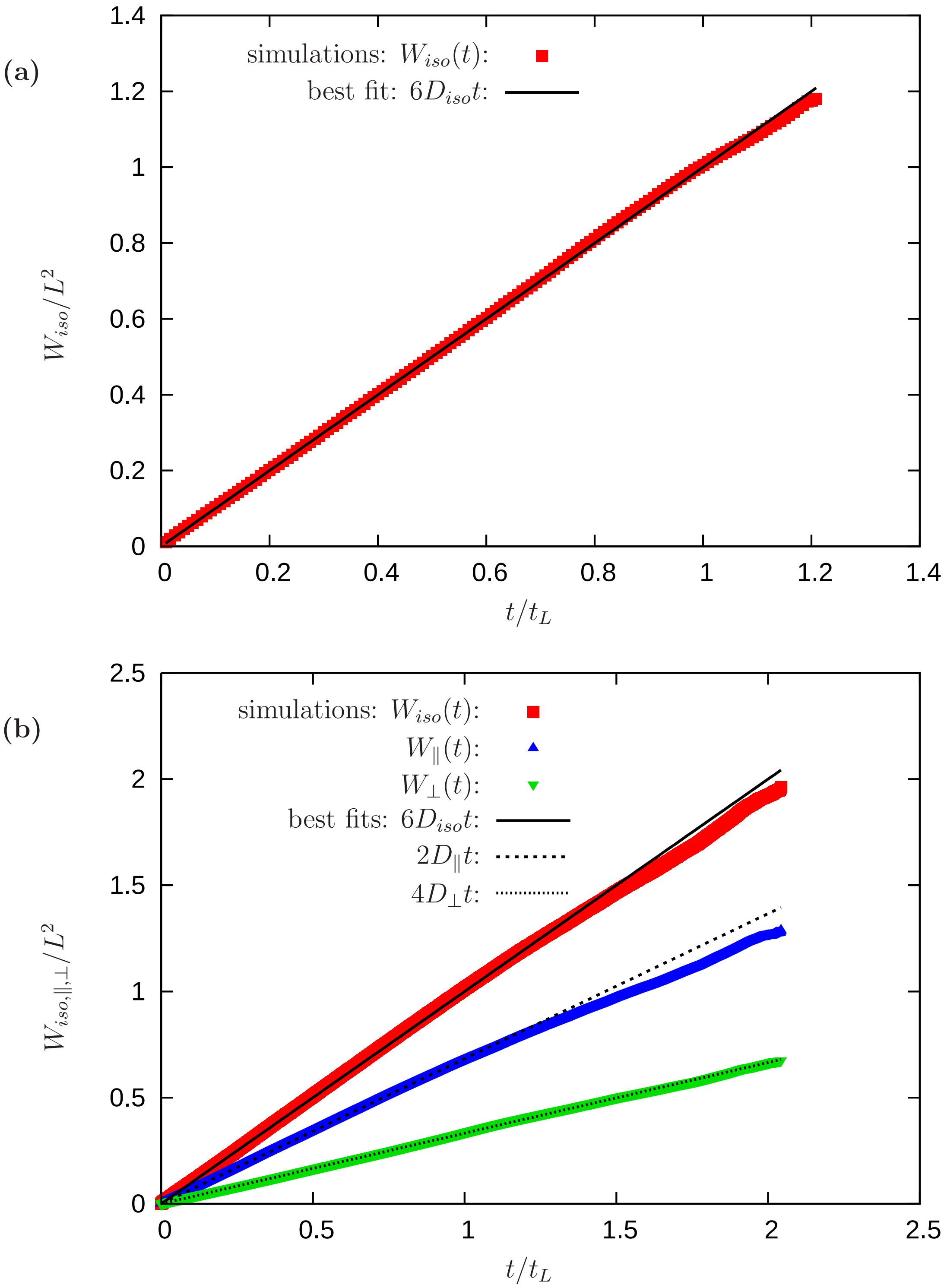

Figure 4.5: Typical MSD curves $W_{iso,\parallel,\perp}$ normalized by L^2 for (a) $L/d = 20$ and $\phi = 0.18$ (isotropic) and (b) $L/d = 20$ and $\phi = 0.27$ vs. time t normalized by t_L, the time for which $W_{iso}(t) = L^2$.

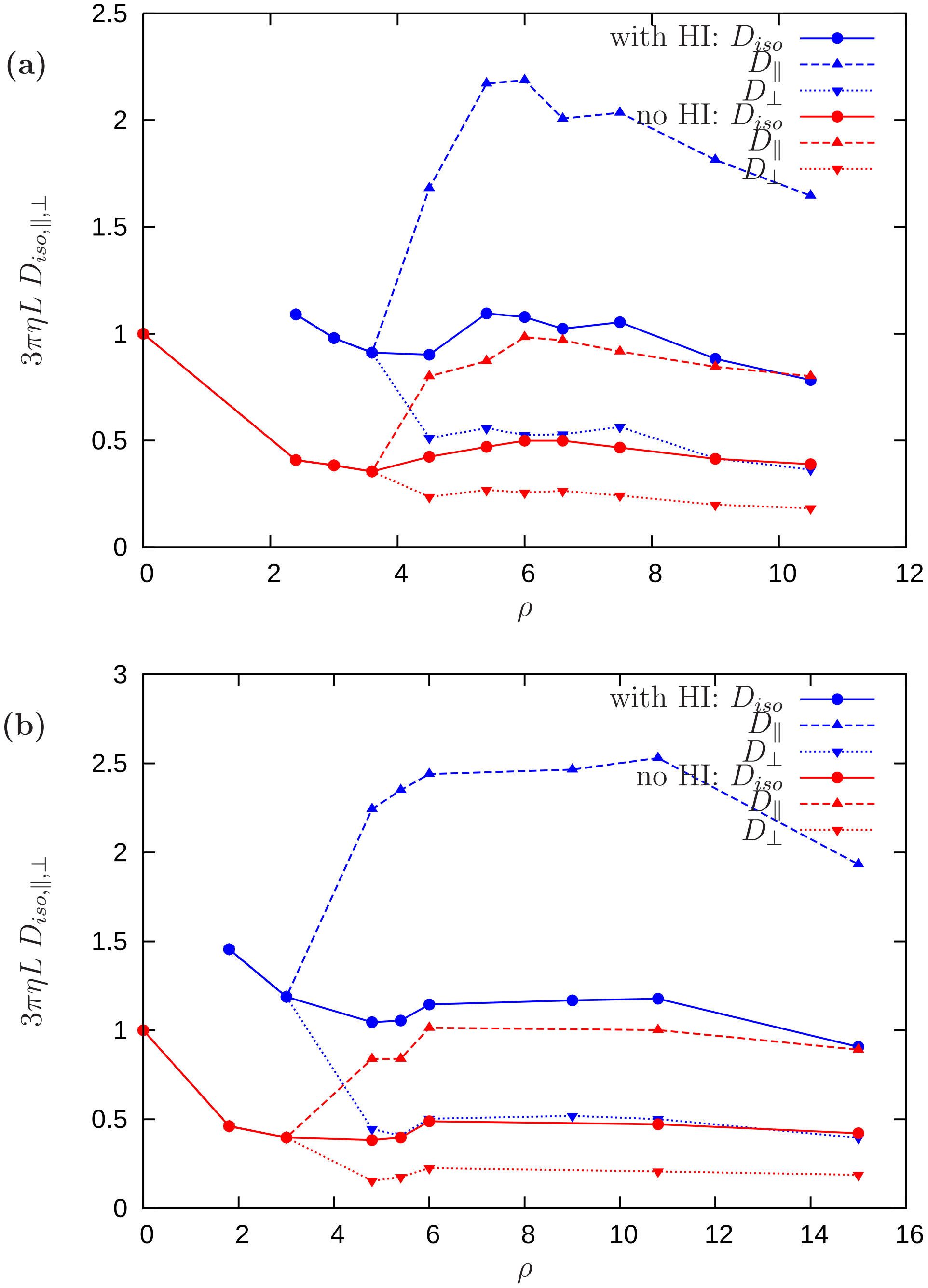

Figure 4.6: Dependence of diffusion constants D_{iso}, $D_{\parallel}$ and $D_{\perp}$ on the normalized volume fraction $\rho = \phi L/d$ for (a) $L/d = 20$ and (b) $L/d = 40$. For both plots, results with (blue curves) and without (red curves) hydrodynamic interactions are shown. The I-N phase transitions is located at $\rho \approx 4$, as predicted by Onsager [77].

This shows that hydrodynamic friction indeed reduces the diffusion constants. Such a comparison between systems with and without hydrodynamics is not possible in experiments, because hydrodynamic interactions cannot be switched off in real systems. However, our experimental cooperation partner M. P. Lettinga developed a way to gradually lower the effect of hydrodynamic friction due to neighboring rods and thereby to approach the situation without hydrodynamic interactions. In the following, his experimental strategy will be briefly explained. Since *fd* viruses are charged, Coulomb interactions lead to an effective steric diameter d which is larger than the hydrodynamic diameter d_{hyd} (see Fig. 4.7.a). By adding salt to the solvent, it is possible to lower the steric diameter d, because salt ions lead to electrostatic screening (see Fig. 4.7.b).

A modification of the hydrodynamic diameter is more difficult, but also possible. By coating *fd* viruses with the water soluble polymers poly-ethylene oxide (PEO), the solvent is caught in the polymer mesh (compare Ref. [85]) as it is shown in Fig. 4.7.c. This leads to an effective increase in the hydrodynamic diameter d_{hyd}, as the solvent particles in the polymer mesh do not contribute to hydrodynamic flow. For two *fd* virus systems with the same steric diameters d (and thereby with same steric aspect ratios L/d) but with different hydrodynamic diameters d_{hyd}, friction with neighboring rods is smaller for the system with smaller d_{hyd}. In Fig. 4.8.b, experimentally measured normalized diffusion constants $\widehat{D}_{iso}(\rho)$ are plotted vs. the reduced volume fraction ρ. Both curves correspond to systems of differently modified *fd* viruses with same steric aspect ratios $L/d \approx 25$, but with different hydrodynamic diameters. *fd* systems with $d = d_{hyd}$ were realized by coating *fd* viruses with 5 kg/mol PEO such that the polymer brush prevents both other rods as well as the flow field to come closer than $d = d_{hyd}$ to the rod. *fd* systems with $L/d_{hyd} = 5.3L/d > L/d$ (i.e. $d = 5.3d_{hyd}$) correspond to uncoated viruses (wild type), where the ionic strength was adjusted to have the same effective diameter d. Since in suspensions of uncoated *fd* viruses there is more space for the solvent to develop flow fields between rods, friction with neighboring rods is typically smaller than for coated viruses. Due to this effect, normalized diffusion constants for $L/d_{hyd} = L/d$ are smaller than those of $L/d_{hyd} = 5.3L/d$ (see Fig. 4.8.b).

Inspired by these experiments, we performed three simulations with $\frac{1}{2}L/d_{hyd} = L/d = 20$ in order to compare them with simulations with $L/d_{hyd} = L/d = 20$. In contrast to experiments, where the length of the *fd* virus is fixed, in MPC-SR simulations, the hydrodynamic diameter d_{hyd} is fixed. However, the rod length

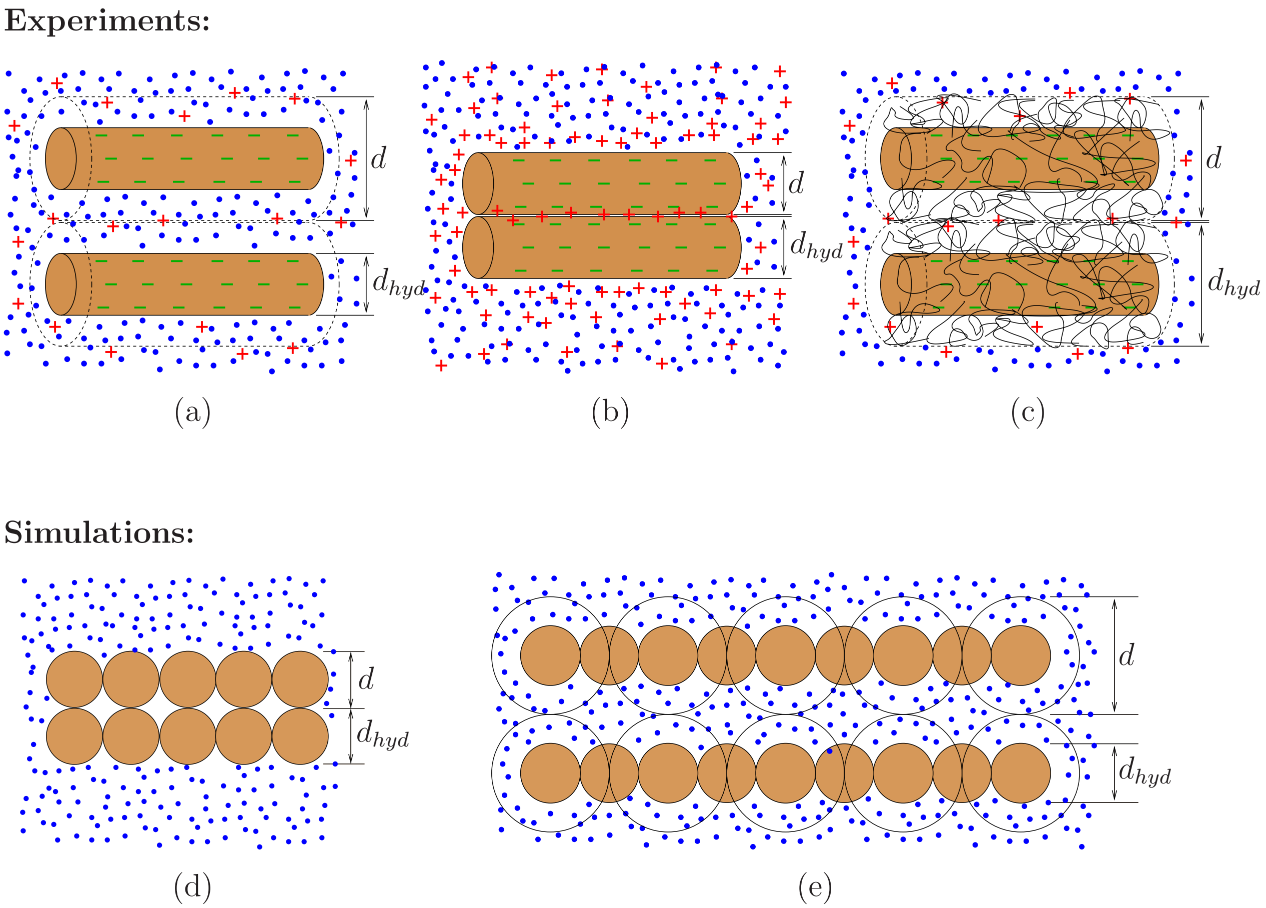

Figure 4.7: Schematical drawings how different hydrodynamic d_{hyd} and steric diameters d are realized in experiments (a-c) and simulations (d,e). (a) The wild-type *fd* virus is charged, and electrostatic repulsion lead to $d > d_{hyd}$. (b) High concentration of salt ions screen electrostatic repulsions such that $d \approx d_{hyd}$. (c) Coating *fd* viruses with PEO, the hydrodynamic diameter is increased. (d, e) Rods in simulations have a fixed hydrodynamic diameter, whereas the steric diameter can be varied.

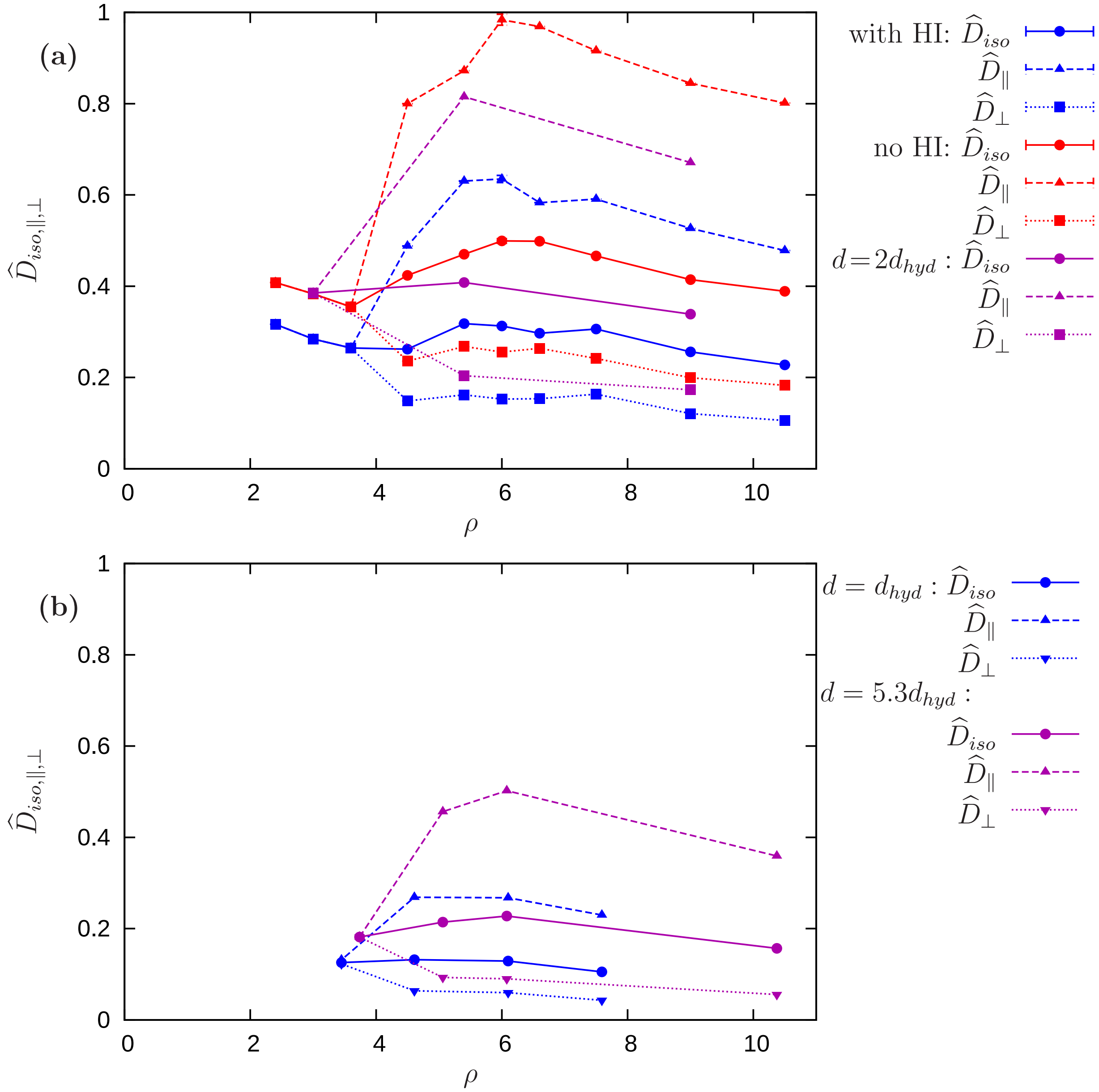

Figure 4.8: Dependence of the normalized diffusion constants $\widehat{D}_{iso,\parallel,\perp}(\rho)$ on the normalized volume fraction. (a) Simulation results of rods with steric aspect ratio $L/d = 20$, but different hydrodynamic diameters. Blue and red curves correspond to systems with and without hydrodynamics, respectively. Magenta curves correspond to HI simulations with $d = 2d_{hyd}$. (b) Experimental data of Lettinga et al. [60] for differently modified *fd* viruses which all have $L/d = 25$, but different d_{hyd}. Blue curves correspond to coated *fd* viruses with 20 kg/mol PEO leading to $d = d_{hyd}$. Magenta curves show results of charged wild-type *fd* viruses at 2 mM salt ($d = 5.3d_{hyd}$).

L and the steric diameter d can be easily varied in our simulations. L can be changed using a different number of monomers while keeping the bond length l, and $d = \sqrt[6]{2}\sigma$ is changed by changing the interaction length scale σ of the Lennard-Jones potential (see Eq. (4.11)). In order to realize that systems with same L/d but different d have the same static properties, also some other system properties like the bending rigidity κ have to be scaled. Except for the Lennard-Jones potential, this leads to identical settings as in the above presented simulations with $L/d = 40$ (and $d = d_{hyd}$). The Lennard-Jones potential is only applied to every second monomer in the shish-kebab rod (see Fig. 4.7.e). The results are also shown in Fig. 4.8.a. Curves which belong to simulations with $d = 2d_{hyd}$, are located between the corresponding curves of MPC-SR and random MPC systems. This systematic dependence is in qualitative agreement with the experimental results of M. P. Lettinga et al. [60].

4.4.2 Diffusion anisotropy

Since anisotropy in diffusion is found also in the absence of hydrodynamic interactions – in contrast to infinite dilution – steric interactions with the anisotropic rod network are obviously sufficient to cause an anisotropy in diffusion. In Fig. 4.9, the anisotropy $D_{\|}/D_{\perp}$ in diffusion is plotted for the two aspect ratios $L/d = 20$ and $L/d = 40$ – both with the MPC-SR and random MPC solvents. Also the experimentally obtained anisotropy $D_{\|}/D_{\perp}$ in *fd* virus suspensions with comparable aspect ratios $L/d = 25$ and $L/d = 52$ are shown in Fig. 4.9. From the simulation data, no significant difference in diffusion anisotropy between systems with and without hydrodynamics can be found. In Sec. 4.4.1, we have shown that hydrodynamics has a strong influence on absolute diffusion constants. Obviously, this hydrodynamic enhancement is equally strong for parallel and perpendicular diffusion constants, such that the anisotropy $D_{\|}/D_{\perp}$ does not differ from that without hydrodynamics. The diffusion anisotropy in dense systems is thereby mainly caused by steric interactions. The influence of steric interactions with the anisotropic rod network on the diffusion anisotropy has an intuitive explanation. The free volume for a rod to move into the direction of its long axis $\hat{\mathbf{u}}$ is much larger than that one for the direction perpendicular to $\hat{\mathbf{u}}$. This results in an anisotropic diffusion which is caused only by entropic reasons. Moreover, a systematic increase of the diffusion anisotropy with increasing rod

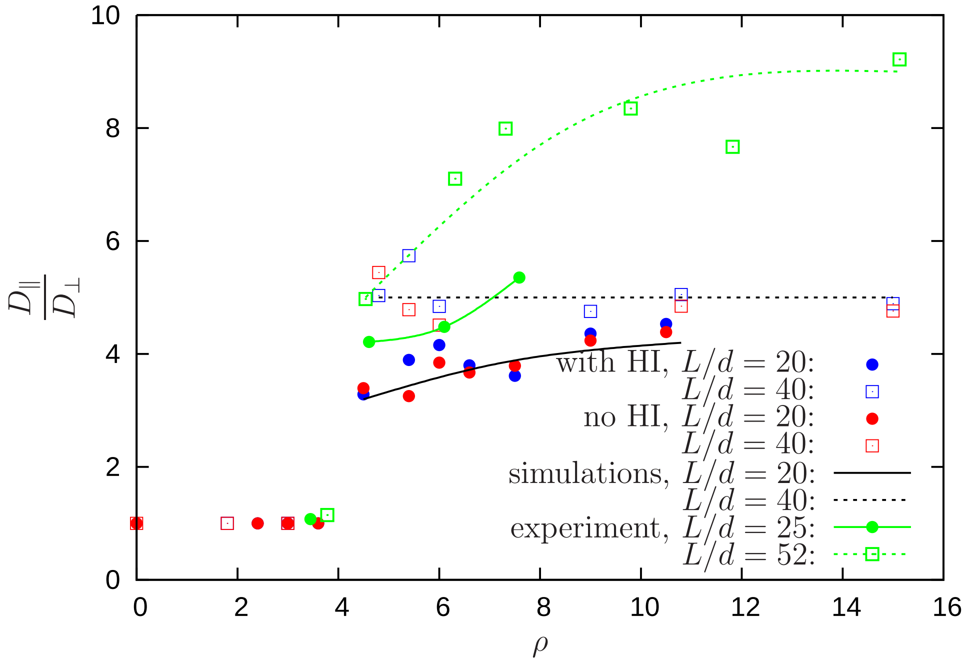

Figure 4.9: ρ dependence of the diffusion anisotropy $D_{\parallel}/D_{\perp}$ of simulations and experiments of *fd* viruses at different rod aspect ratios. For simulations, results of both solvent (MPC-SR and random MPC solvents) are shown. Lines are guides to the eyes.

aspect ratios can be seen in Fig. 4.9. This systematic trend is in agreement with the experiments of M. P. Lettinga. However, other computer simulations [5, 18, 63] on comparably short rods do not find such a dependence on rod aspect ratios. They rather find that the diffusion anisotropy depends only on the nematic order parameter $\langle P_2 \rangle$. A convenient representation for a comparison of our simulations with other studies is therefore that of Fig. 4.10, where the diffusion anisotropy $D_{\parallel}/D_{\perp}$ is plotted vs. nematic order parameter $\langle P_2 \rangle$. In particular for relatively high order parameters of $\langle P_2 \rangle \gtrsim 0.9$, the diffusion anisotropy of our computer simulations is smaller than those of the other studies [5, 18, 63]. In order to understand this discrepancy, it is necessary to have a closer look to the simulation models of the other studies.

Allen [5]: Allen performed MD simulations of elongated ellipsoids with $L/d = 5$ and 10. These ellipsoids do not have any friction, and collisions with other ellipsoids are reflecting, corresponding to slip boundary conditions. In

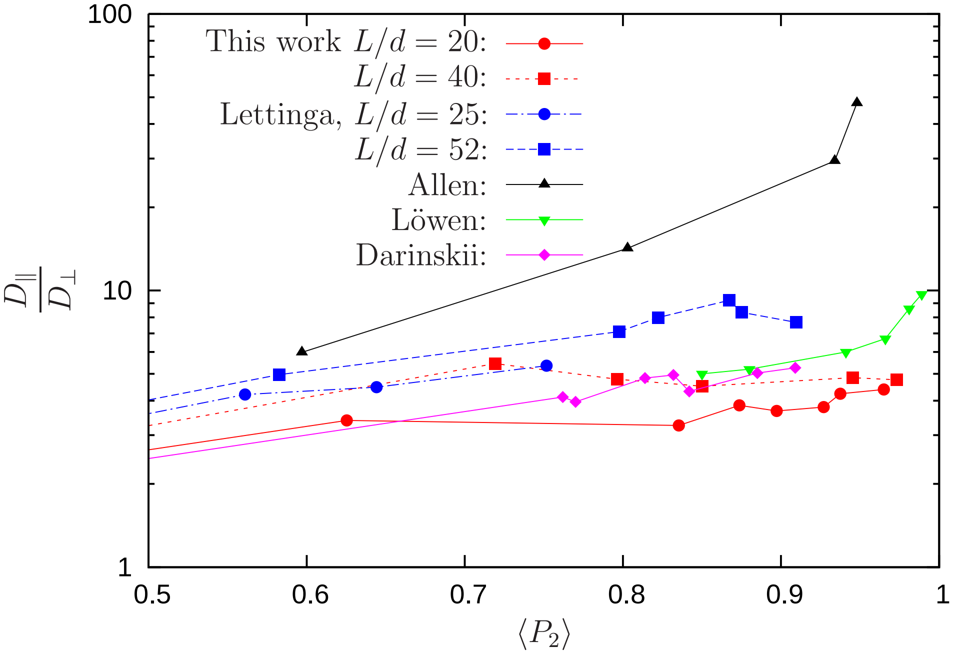

Figure 4.10: Diffusion anisotropy vs. $\langle P_2 \rangle$ of our simulations, *fd* viruses and simulations by Allen [5], Löwen [63] and Darinskii [18].

this model, ellipsoids are strongly hindered to move perpendicular to the nematic director, whereas an unphysically high inertia for parallel motion leads to a very high anisotropy.

Löwen [63]: Löwen performed Brownian-Dynamics simulations of hard spherocylinders with aspect ratios $4.8 \leq L/d \leq 16$. In this simulation model, friction with the solvent is taken into account. Hydrodynamic interactions are considered only on the level of an anisotropic friction. He chose anisotropic step sizes for trial moves in parallel and perpendicular directions such that diffusion constants at infinite dilutions agree with those of de la Torre et al. [21, 94] (see Eqs. (4.6 - 4.8)). Löwen thereby took into account hydrodynamic interactions along the whole contour of a rod, but the hydrodynamic influence of neighboring rods is disregarded. However, the latter interactions can be far stronger in dense systems, so that the diffusion anisotropy is over-estimated. A comparison with our simulations shows that there is no hydrodynamic effect on the diffusion anisotropy, if all (intra- and inter-rod) hydrodynamic interactions are taken into account.

Darinskii et al. [18]: In the work of Darinskii et al., the dynamics of semiflexible shish-kebab rods with an aspect ratio of $L/d = 8$ was studied by MD simulations. While friction with solvent particles is not included in their model, collisions with other rods do not have perfect slip. As rods are composed of interacting spheres, the rod surface is not perfectly smooth. This leads to lower diffusion anisotropies than those of Allen [5], but it turns out that the absence of solvent friction leads to higher diffusion anisotropies than in our simulations with the aspect ratio of $L/D = 20$. They find that the diffusion anisotropy only depends on the nematic order parameter $\langle P_2 \rangle$, independent of the flexibility.

A yet open question is why in our computer simulations as well as for *fd* viruses, an increase in diffusion anisotropy can be observed with increasing aspect ratio L/d for a fixed nematic order parameter. We can at least qualitatively explain this increase by simple scaling arguments. We assume that the nematic order parameter $\langle P_2 \rangle$ is a function which only depends on $\rho = \phi L/d$ rather than on ϕ and L/d independently. Fig. 4.4 shows that this assumption is justified in our computer simulations – at least in the considered range of aspect ratios. For a fixed nematic order parameter $\langle P_2 \rangle$, the corresponding volume fraction $\phi(\langle P_2 \rangle, L/d)$ therefore depends on the rod aspect L/d ratio like

$$\phi(\langle P_2 \rangle, L/d) \propto \frac{d}{L}. \tag{4.21}$$

We assume that for a given nematic order parameter $\langle P_2 \rangle$, the hindrance in the rod motion in parallel direction does not play a significant role. The motion in perpendicular direction, however, is strongly hindered due to the presence of other rods. In order to perform a step of a certain length in perpendicular direction, the rod has to find an appropriate gap in the cage of neighboring rods. The probability p_{gap} of finding such a gap decreases monotonically with the average number n_b of other rods which can block the path through this gap. This number n_b is proportional to $\phi(\langle P_2 \rangle, L/d)/\phi^*$

$$n_b \propto \frac{\phi(\langle P_2 \rangle, L/d)}{\phi^*} \tag{4.22}$$

where ϕ^* is the overlap volume fraction (2.17) which depends on L/d like

$$\phi^* \propto \left(\frac{L}{d}\right)^{-2}. \tag{4.23}$$

Inserting Eq. (4.21) and Eq. (4.23) into Eq. (4.22) yields

$$n_b \propto \frac{L}{d}. \tag{4.24}$$

Since the probability that a rod is able to move a certain distance in perpendicular direction decays with $n_b \propto L/d$, the anisotropy increases with increasing aspect ratio L/d.

4.5 Summary and Conclusions

Simulations of rod-like colloids were performed both with HI (using the MPC-SR solvent) and without HI (using the random MPC solvent). Single-rod simulations show that the model is in accordance with theoretical expressions for single-rod diffusion constants. In MPC-SR simulations, the hydrodynamic enhancement as well as the predicted anisotropic diffusion of single rods was found. Dense rod systems were studied both in the isotropic and the nematic phases, and diffusion constants were calculated. The hydrodynamic enhancement was found to be present even in dense rod suspensions. Moreover, simulations as well as experiments have shown that the larger the hydrodynamic diameter the more strongly is diffusion diminished with increasing concentration. In the nematic phase, diffusion constants are strongly anisotropic. We found that the diffusion anisotropy increases with rod aspect ratio, which is in contradiction to other studies of short rods, where diffusion anisotropy seems to be a function of the nematic order parameter only. However, the aspect-ratio dependence of the diffusion anisotropy was also found in experiments with *fd* viruses. We could explain this observation by simple scaling arguments.

5 The hydrodynamic mobility tensor

In Sec. 2.1, the mobility tensor was introduced. For solvents which can be well described by the Stokes equation (2.4), we found that the mobility tensor is the Oseen tensor $\mathbf{T}_O(\mathbf{r})$ (2.6). In this chapter, we present a way how the Fourier transform (FT) of the mobility tensor can be directly determined in MPC simulations. This concept is then applied to several systems in order to gain insights into hydrodynamic interactions. In Sec. 5.3, the FT of the mobility tensor of a free MPC-SR solvent is calculated and compared to the solution of the Stokes equation (2.4). From these simulations, the "hydrodynamic cutoff" can be determined. In Sec. 5.4.1, the FT of the mobility tensor is calculated for MPC-SR systems containing rod-like colloids. It will turn out that hydrodynamic interactions are strongly screened due to the presence of the rods. Hydrodynamic screening can be quantified by the hydrodynamic "screening length" $\varkappa^{-1}$, a characteristic distance over which hydrodynamic interactions decay. For anisotropic systems, we determine two different screening lengths, $\varkappa_{\parallel}^{-1}$ and $\varkappa_{\perp}^{-1}$.

5.1 Derivation of the anisotropic screened mobility tensor

The mobility tensor $\mathbf{T}(\mathbf{r}-\mathbf{r}')$ of solvent particles in equilibrium relates the velocity field $\mathbf{v}(\mathbf{r})$ to an external body force $\mathbf{f}(\mathbf{r}')$ by

$$\mathbf{v}(\mathbf{r}) = \int \mathbf{T}(\mathbf{r}-\mathbf{r}') \cdot \mathbf{f}(\mathbf{r}') d\mathbf{r}' \tag{5.1}$$

(see Sec. 2.1). For a simple fluid, in the limit of vanishing Reynold numbers, $\mathbf{T}(\mathbf{r}-\mathbf{r}') = \mathbf{T}_O(\mathbf{r}-\mathbf{r}')$ is the Green's function of the Stokes equation (2.4), known as Oseen tensor.

Once an arbitrary force distribution $\mathbf{f}(\mathbf{r})$ is known, the corresponding velocity field can be calculated using Eq. (5.1). The problem is that the force distribution is not a priori known in most soft matter systems. Let us discuss this very general problem of soft matter systems considering the example of rod-like colloids. Each rod segment is coupled to other rod segments due to the stiffness. Therefore a rod monomer cannot follow the surrounding fluid flow and hence exerts a force on the fluid. This force induces a further contribution to the velocity field. In order to get a consistent force distribution $\mathbf{f}(\mathbf{r})$, generally a linear integral equation has to be solved, compare Ref. [79]. Alternatively, if only point particles are considered, like in the shish kebab model (see Chap. 4.1), the continuous force distribution $\mathbf{f}(\mathbf{r})$ becomes a set of discrete forces $\mathbf{F}_i$, and the integral equation reduces to a set of linear algebraic equations. Even in the discretized case, it is often not feasible to solve the set of equations numerically, because the required computational effort restricts us to systems with $N < 500$ (N being the number of point particles) which is far less than needed e.g. in dense rod suspensions. We have done such a calculation for a single long rod ($L/d = 400$). The resulting velocity field induced by a point force a small distance away from a rod is shown in Fig. 5.1. Comparing Fig. 5.1 with a corresponding flow field without the rod (see Fig. 2.1), one can clearly see that the rod strongly influences the velocity field. Even in the presence of only one rod, the effect of hydrodynamic screening becomes obvious: flow velocities on the rear side of the rod are far smaller than in the case of a free solvent (Fig. 2.1). However, even if it were possible to calculate the velocity field for all desired systems, the resulting flow field always depends strongly on the current microscopic configuration. Since we are only interested in statistical averages, another (phenomenological) approach is desirable.

Brinkman [10] and Debye and Büche [22] suggested a phenomenological equation which takes into account hydrodynamic screening. They extended the Stokes equation (2.4) by an additional friction term $-\eta\varkappa^2\mathbf{v}(\mathbf{r})$ proportional to the flow velocity $\mathbf{v}(\mathbf{r})$. This equation is called the Debye-Büche-Brinkman equation

$$\eta\nabla^2\mathbf{v}(\mathbf{r}) - \nabla p(\mathbf{r}) - \eta\varkappa^2\mathbf{v}(\mathbf{r}) = \mathbf{f}(\mathbf{r}) \qquad (5.2)$$

$$\nabla \cdot \mathbf{v}(\mathbf{r}) = 0. \qquad (5.3)$$

The strength of the screening is given by the “screening constant” $\varkappa$. The reciprocal of $\varkappa$ is the “hydrodynamic screening length” $\varkappa^{-1}$. We denote the Green’s function of the Debye-Büche-Brinkman equation (5.2) the “isotropic

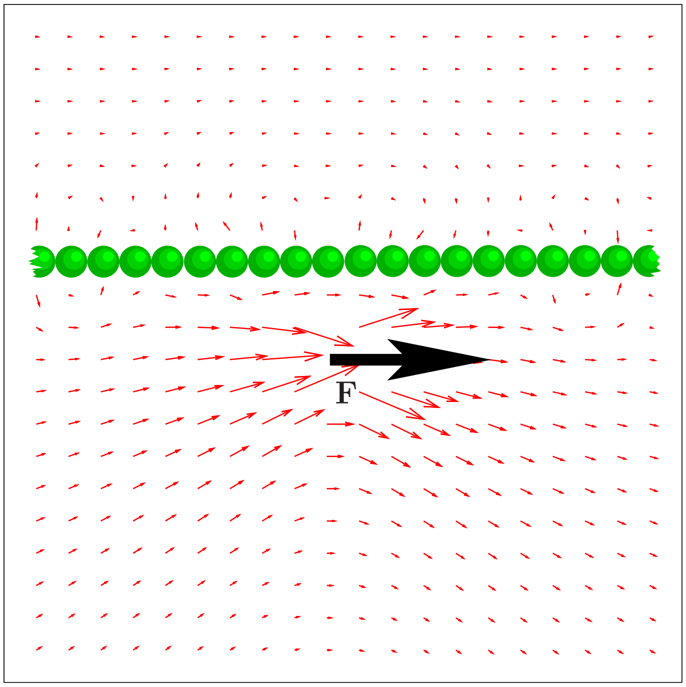

Figure 5.1: The velocity field due to a point force **F** in the vicinity of a long rod ($L/d = 400$). The presence of the rod strongly influences the flow field. On the upper side of the rod it can be clearly seen that hydrodynamics is screened by the rod.

screened hydrodynamic mobility tensor" $\mathbf{T}_s(\mathbf{r})$. Its explicit form is [47]

$$\begin{aligned} \mathbf{T}_s(\mathbf{r}) &= \frac{1}{4\pi\eta r}\left(h_1(\varkappa r)\hat{\mathbf{I}} + h_2(\varkappa r)\frac{\mathbf{r}\otimes\mathbf{r}}{r^2}\right) && (5.4)\\ \text{with} \quad h_1(x) &= -x^{-2} + \left(1 + x^{-1} + x^{-2}\right)e^{-x} && (5.5)\\ \text{and} \quad h_2(x) &= 3x^{-2} - \left(1 + 3x^{-1} + 3x^{-2}\right)e^{-x}. && (5.6) \end{aligned}$$

In contrast to the long-ranged Oseen-tensor, the mobility tensor of the isotropic screened hydrodynamic mobility tensor is short-ranged and decays like a Yukawa potential where the characteristic decay length is the hydrodynamic screening length $\varkappa^{-1}$. The mobility tensor (5.4) of the Debye-Büche-Brinkman equation reduces to the Oseen tensor in the limit of $\varkappa \to 0$.

The Debye-Büche-Brinkman equation has shown to be a good phenomenological description in isotropic complex fluids. However, in very dense rod suspensions, rods form a nematic phase which is anisotropic. Accordingly, one can expect that also screening is anisotropic, i.e. that there are different inverse screening lengths

$\varkappa_\parallel$ and $\varkappa_\perp$, for parallel and perpendicular directions, respectively. We generalize the Debye-Büche-Brinkman equation (5.2) to incorporate anisotropic screening. This is done by replacing $\varkappa^2$ by a screening tensor **S**. Let us consider the more general case with different screening lengths for all three dimensions. For simplicity we assume that the screening tensor **S** is diagonal (this can allways be achieved by transforming into a proper coordinate system). Thus the screening tensor reads

$$\mathbf{S} = \begin{pmatrix} \varkappa_x^2 & 0 & 0 \\ 0 & \varkappa_y^2 & 0 \\ 0 & 0 & \varkappa_z^2 \end{pmatrix}. \tag{5.7}$$

With this definition we constitute an equation which we call the **A**nisotropic **S**creened **C**reeping **F**low **E**quation (ASCFE)

$$\begin{aligned} \eta\nabla^2\mathbf{v}(\mathbf{r}) - \nabla p(\mathbf{r}) - \eta\mathbf{S}\mathbf{v}(\mathbf{r}) &= \mathbf{f}(\mathbf{r}) && (5.8) \\ \nabla\cdot\mathbf{v}(\mathbf{r}) &= 0. && (5.9) \end{aligned}$$

In the following, the Green' function of the ASCFE, the "anisotropic screened mobility tensor" $\mathbf{T}_a(\mathbf{r})$ will be calculated in Fourier space ($\mathbf{T}_a(\mathbf{r}) \rightarrow \widetilde{\mathbf{T}}_a(\mathbf{k})$). Fourier transforming the ASCFE yields

$$\begin{aligned} -\eta k^2\tilde{\mathbf{v}}(\mathbf{k}) + i\mathbf{k}\tilde{p}(\mathbf{k}) - \eta\mathbf{S}\tilde{\mathbf{v}}(\mathbf{k}) &= \tilde{\mathbf{f}}(\mathbf{k}) && (5.10) \\ \mathbf{k}\cdot\tilde{\mathbf{v}}(\mathbf{k}) &= 0. && (5.11) \end{aligned}$$

This algebraic equation can be written in matrix form as

$$\underbrace{\begin{pmatrix} -\eta(k^2+\varkappa_x^2) & 0 & 0 & ik_x \\ 0 & -\eta(k^2+\varkappa_y^2) & 0 & ik_y \\ 0 & 0 & -\eta(k^2+\varkappa_z^2) & ik_z \\ -k_x & -k_y & -k_z & 0 \end{pmatrix}}_{=:\,\mathbf{A}} \begin{pmatrix} \tilde{v}_x \\ \tilde{v}_y \\ \tilde{v}_z \\ \tilde{p} \end{pmatrix} = \begin{pmatrix} \tilde{f}_x \\ \tilde{f}_y \\ \tilde{f}_z \\ 0 \end{pmatrix}. \tag{5.12}$$

The ASCFE can be solved by matrix multiplication with the inverse matrix $\mathbf{A}^{-1}$,

$$\begin{pmatrix} \tilde{v}_x \\ \tilde{v}_y \\ \tilde{v}_z \\ \tilde{p} \end{pmatrix} = \mathbf{A}^{-1} \begin{pmatrix} \tilde{f}_x \\ \tilde{f}_y \\ \tilde{f}_z \\ 0 \end{pmatrix}. \tag{5.13}$$

This can be compared with the FT of Eq. (5.1). Since our simulations have periodic boundary conditions, the FT of Eq. (5.1) can be easily expressed using the convolution theorem for periodic functions

$$\begin{aligned} \mathbf{v}(\mathbf{r}) &= \int \mathbf{T}_a(\mathbf{r}-\mathbf{r}')\cdot\mathbf{f}(\mathbf{r}')d\mathbf{r}' && (5.14)\\ \Leftrightarrow \qquad \tilde{\mathbf{v}}(\mathbf{k}) &= V\widetilde{\mathbf{T}}_a(\mathbf{k})\tilde{\mathbf{f}}(\mathbf{k}). && (5.15) \end{aligned}$$

Here, $V = L_xL_yL_z$ is the volume of the periodic simulation box, and the linear sizes of the simulation box are L_x, L_y and L_z for x, y and z-direction, respectively. By comparing Eq. (5.13) with Eq. (5.15), the upper left 3×3 submatrix of $\mathbf{A}^{-1}/V$ by $\widetilde{\mathbf{T}}_a(\mathbf{k})$ can be identified with the FT of the mobility tensor. The elements of this upper left submatrix are calculated by Cramer's rule. We introduce the abbreviations $X := -\eta(k^2+\varkappa_x^2)$, $Y := -\eta(k^2+\varkappa_y^2)$ and $Z := -\eta(k^2+\varkappa_z^2)$.

$$\begin{aligned} \widetilde{\mathbf{T}}_a(\mathbf{k}) &= \frac{1}{V\det(\mathbf{A})}\begin{pmatrix} \det\begin{pmatrix} Y & 0 & ik_y\\ 0 & Z & ik_z\\ k_y & k_z & 0\end{pmatrix} & -\det\begin{pmatrix} 0 & 0 & ik_y\\ 0 & Z & ik_z\\ k_x & k_z & 0\end{pmatrix} & \det\begin{pmatrix} 0 & Y & ik_y\\ 0 & 0 & ik_z\\ k_x & k_y & 0\end{pmatrix}\\ -\det\begin{pmatrix} 0 & 0 & ik_x\\ 0 & Z & ik_z\\ k_y & k_z & 0\end{pmatrix} & \det\begin{pmatrix} X & 0 & ik_x\\ 0 & Z & ik_z\\ k_x & k_z & 0\end{pmatrix} & -\det\begin{pmatrix} X & 0 & ik_x\\ 0 & 0 & ik_z\\ k_x & k_y & 0\end{pmatrix}\\ \det\begin{pmatrix} 0 & 0 & ik_x\\ Y & 0 & ik_y\\ k_y & k_z & 0\end{pmatrix} & -\det\begin{pmatrix} X & 0 & ik_x\\ 0 & 0 & ik_y\\ k_x & k_z & 0\end{pmatrix} & \det\begin{pmatrix} X & 0 & ik_x\\ 0 & Y & ik_y\\ k_x & k_y & 0\end{pmatrix} \end{pmatrix}\\ &= \frac{1}{V(k_x^2YZ+k_y^2ZX+k_z^2XY)}\begin{pmatrix} k_y^2Z+k_z^2Y & -k_xk_yZ & -k_xk_zY\\ -k_xk_yZ & k_x^2Z+k_z^2X & -k_yk_zX\\ -k_xk_zY & -k_yk_zX & k_y^2X+k_x^2Y \end{pmatrix} \qquad (5.16) \end{aligned}$$

We have calculated the FT of this very general hydrodynamic mobility tensor (5.16), because it includes as special cases the FT's of all the other mobility tensors which will be needed below. The solution of the Stokes equation is obtained for $\varkappa_x = \varkappa_y = \varkappa_z = 0$, the case of the Debye-Büche-Brinkman equation (isotropic screening) is found for $\varkappa_x = \varkappa_y = \varkappa_z \neq 0$, and the solution of the uniaxially anisotropic screened creeping flow equation (like in nematic systems) is obtained for $\varkappa_x =: \varkappa_\parallel \neq \varkappa_y = \varkappa_z =: \varkappa_\perp$. The simplified expressions of the mobility tensor are presented in the appropriate sections below.

In the next section, a procedure is described, how hydrodynamic mobility tensors in Fourier space $\widetilde{\mathbf{T}}(\mathbf{k})$ can be determined in simulations. By fitting the measured $\widetilde{\mathbf{T}}(\mathbf{k})$ to the solution (5.16) of the ASCFE, screening lengths can be obtained.

5.2 The mobility tensor from simulations

It is possible to determine the Fourier transform of the mobility tensor from MPC-SR simulations. We follow the same procedure as Dünweg and Kremer in Ref. [30, 31]. In the following, the procedure is explained in detail. The mobility tensor is related to the fluctuations of the particle velocities in equilibrium by the Green-Kubo Formula [20, 38]

$$\mathbf{T}(\mathbf{r}) \quad = \quad \frac{1}{k_B T} \int_0^\infty dt \frac{1}{V} \int_V d\mathbf{r}' \left\langle \mathbf{v}(\mathbf{r}', 0) \otimes \mathbf{v}(\mathbf{r} + \mathbf{r}', t) \right\rangle \tag{5.17}$$

Since in equilibrium systems, time correlation functions like the integrand of Eq. (5.17) only depend on time differences, the ensemble average $\langle ... \rangle$ can be replaced by a time average

$$\langle \mathbf{v}(\mathbf{r}', 0) \otimes \mathbf{v}(\mathbf{r} + \mathbf{r}', t) \rangle = \frac{1}{N(t)} \sum_{i=1}^{N(t)} \mathbf{v}(\mathbf{r}', t_i) \otimes \mathbf{v}(\mathbf{r} + \mathbf{r}', t + t_i) \tag{5.18}$$

in simulations. Here, $N(t)$ is the number of possibilities to create pairs of t_i and $t + t_i$ from the recorded data which are separated by a time difference t. Since only a finite number of values $\mathbf{v}(\mathbf{r}', t_i)$ can be stored in simulations, also $N(t)$ is limited.

Fourier transformation of Eq. (5.17) with respect to space coordinates ($\mathbf{r} \rightarrow \mathbf{k}$) and the use of the convolution theorem implies

$$\widetilde{\mathbf{T}}(\mathbf{k}) \quad = \quad \frac{1}{k_B T} \int_0^\infty dt \left\langle \tilde{\mathbf{v}}^*(\mathbf{k}, 0) \otimes \tilde{\mathbf{v}}(\mathbf{k}, t) \right\rangle . \tag{5.19}$$

The particle-based MPC-SR algorithm for the solvent used in our simulations allows us to measure the Fourier transforms $\tilde{\mathbf{v}}(\mathbf{k}, t)$ of the velocity field directly,

$$\tilde{\mathbf{v}}(\mathbf{k}, t) \quad = \quad \frac{1}{N} \left(\hat{\mathbf{I}} - \hat{\mathbf{k}} \otimes \hat{\mathbf{k}} \right) \sum_{i=1}^{N} \mathbf{v}_i(t) \exp(-i\mathbf{k} \cdot \mathbf{r_i}(t)). \tag{5.20}$$

Since for an incompressible fluid, longitudinal modes do not contribute to the hydrodynamic mobility tensor, the operator $(\hat{\mathbf{I}} - \hat{\mathbf{k}} \otimes \hat{\mathbf{k}})$ is applied in order to consider only transversal modes. The Fourier transform $\tilde{\mathbf{v}}(\mathbf{k}, t)$ can be understood as the amplitude of the shear wave with wave vector $\mathbf{k}$ at time t. With the calculated $\tilde{\mathbf{v}}(\mathbf{k}, t)$ of Eq. (5.20), we calculate $\widetilde{\mathbf{T}}(\mathbf{k})$ according to Eq. (5.19). The accessible range of $\mathbf{k}$-vectors is discrete due to the system periodicity and limited for small values by the sizes L_α ($\alpha = x, y, z$) of the periodic simulation box.

The range of $\mathbf{k}$, with physical meaning is limitted for large $\mathbf{k}$-vectors since the continuum description of the solvent breaks down as soon as the corresponding wave lengths are of the order of particle distances. We call this typical length scale the "hydrodynamic cutoff" λ_c. In Sec. 5.3, the hydrodynamic cutoff will be studied in dependence on the collision time h for MPC-SR systems. Since only a limited amount of $\mathbf{k}$-vectors can be sampled, a smallest wavelength λ_{min} has to be chosen which gives an upper threshold for $\mathbf{k}$-vectors to be sampled. Hence, we determine shear waves only for

$$k_\alpha = (2\pi/L_\alpha) i_\alpha \tag{5.21}$$

where i_α is an integer with $0 < |i_\alpha| \leq L_\alpha/\lambda_{min}$.
With this method, $\widetilde{\mathbf{T}}(\mathbf{k})$ can be determined numerically for each accessible $\mathbf{k}$-vector and compared to its theoretical prediction (5.16).

5.3 Hydrodynamic cutoff

Since the MPC-SR solvent is widely used in computer simulations of low Reynold number fluids, it is essential to see how good it reproduces hydrodynamic behavior, i.e. that the flow field obeys the Stokes equation. We study this problem by performing simulations of a free MPC-SR solvent.
By setting $\varkappa_x = \varkappa_y = \varkappa_z = 0$, Eq. (5.16) reduces to the FT of the Oseen tensor (i.e. the Green's function of the Stokes equation)

$$\widetilde{\mathbf{T}}_O(\mathbf{k}) = \frac{1}{\eta V} \frac{1}{k^2} \left(\hat{\mathbf{I}} - \hat{\mathbf{k}} \otimes \hat{\mathbf{k}} \right). \tag{5.22}$$

Since the free MPC-SR solvent is an isotropic system, the trace of $\widetilde{\mathbf{T}}_O(\mathbf{k})$ should only depend on the length of $\mathbf{k}$, and all essential information about hydrodynamics are included in the following quantity

$$\begin{aligned} \widetilde{T}_O(k) &:= \frac{1}{2} \mathrm{Tr}\, \widetilde{\mathbf{T}}_O(\mathbf{k}) = \frac{1}{\eta V} \frac{1}{k^2} && (5.23) \\ \eta V \widetilde{T}_O(k) &= \frac{1}{k^2}. && (5.24) \end{aligned}$$

Hence a plot of $\eta V \widetilde{T}_O(k)$ vs. k in a double logarithmic representation should give a straight line with a slope of -2 for all solvents which obey the Stokes equation.

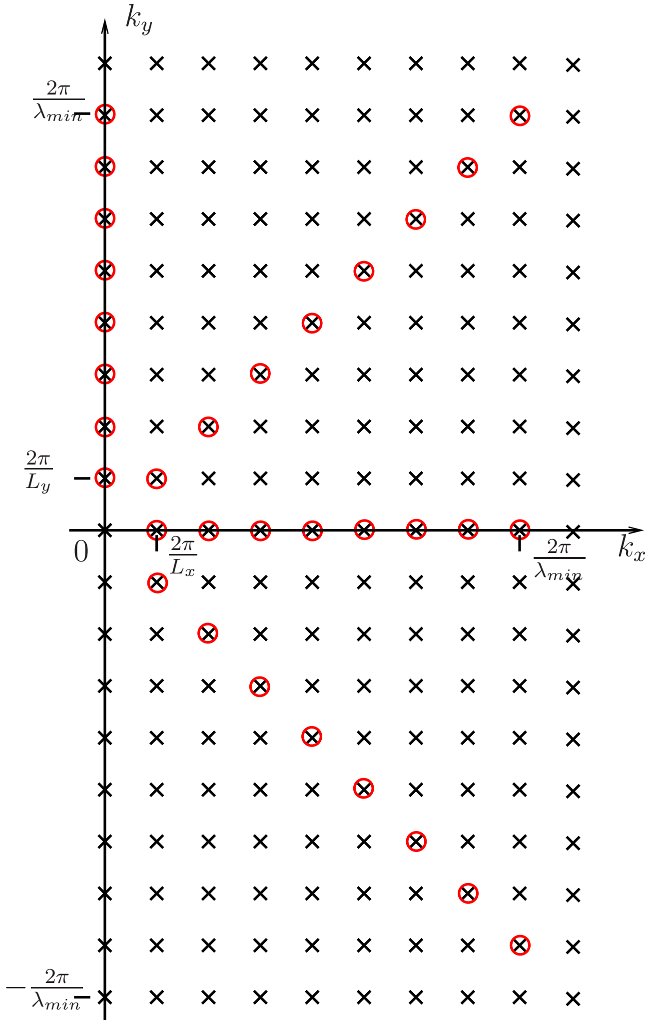

Figure 5.2: The pattern how **k** space is sampled for isotopic systems. The crosses show the accessible **k**-vectors and red circles are those used for the evaluation of Eq. (5.19) and (5.20).

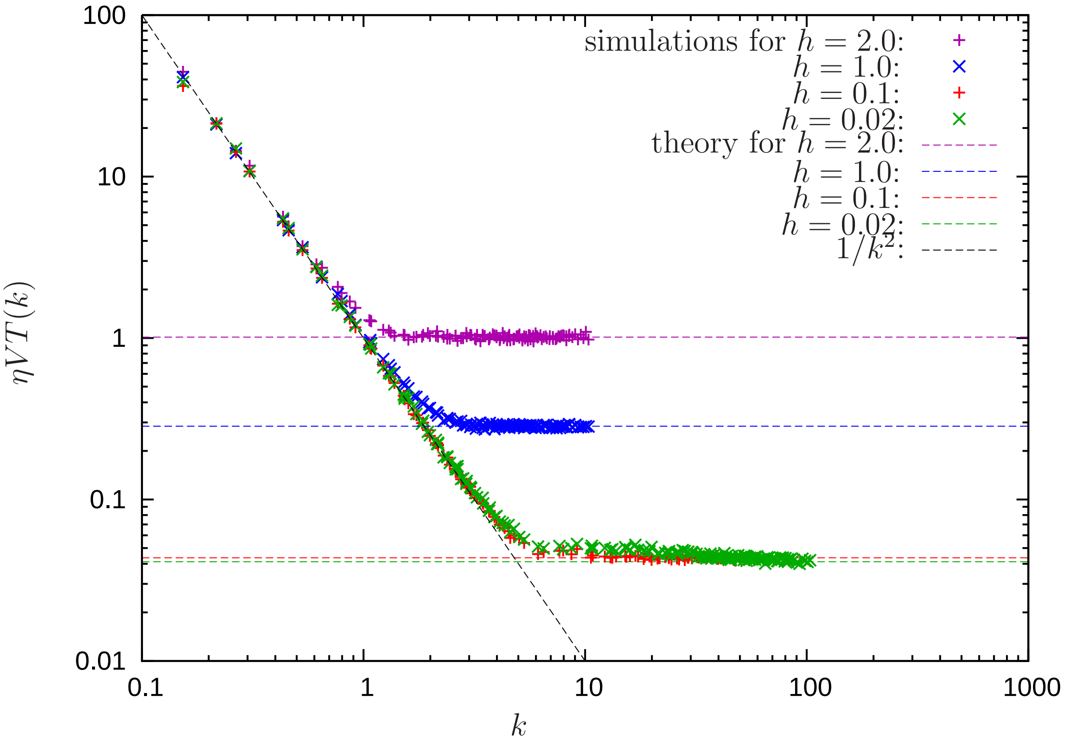

Figure 5.3: k dependence of $\widetilde{T}(k)$ of simple MPC-SR fluids with different collision times h. The black dashed line is the $1/k^2$ dependence expected from the Stokes equation (2.4). The colored horizontal lines are the theoretical predictions of Eq. (5.25) assuming molecular chaos. Symbols correspond to simulation results.

For these simulations, we use a cubic simulation box, i.e. $L_x = L_y = L_z =: L_{iso}$ In principle, $\widetilde{\mathbf{T}}(\mathbf{k})$ could be calculated for all accessible $\mathbf{k}$'s given by Eq. (5.21). However, the quantity of interest is $\widetilde{T}(k)$ which only depends on $k = |\mathbf{k}|$. The average amount of accessible data points between k and $k+\Delta k$ increases quadratically with k. Since we want to calculate $\widetilde{\mathbf{T}}(\mathbf{k})$ for all k's with the same accuracy, and each data point requires the same computational effort, we do not evaluate all the possible $\widetilde{\mathbf{T}}(\mathbf{k})$'s for large $\mathbf{k}$-vectors. Instead, high-symmetry lines in $\mathbf{k}$ space are considered, for which $\mathbf{k} = 2\pi/L_{iso} i_\alpha \mathbf{m}$ with $0 < |i_\alpha| \leq L_\alpha/\lambda_{min}$ and

- $\mathbf{m} \in \{(1,0,0), (0,1,0), (0,0,1)\}$
- $\mathbf{m} \in \{(1,\pm1,0), (1,0,\pm1), (0,1,\pm1)\}$
- $\mathbf{m} \in \{(1,\pm1,\pm1), (1,\pm1,\mp1)\}$.

Fig. 5.2 shows a cut of the **k** space along the xy-plane which demonstrates how **k** space is sampled.

In Fig. 5.3, simulation data for four MPC-SR solvents with different collision times h are shown. For the viscosity η, the analytic expressions (3.13 - 3.14) where used. The fact that data points for small wave numbers k lie on the predicted master curve $1/k^2$ confirms that the MPC-SR solvents do obey the Stokes equation (2.4) for all corresponding wave vectors. Furthermore, it verifies once more that the expressions (3.13 - 3.14) are indeed a very good description of the shear viscosity. However, data points for large wave numbers k deviate from the $1/k^2$ prediction of the Stokes equation and approach a plateau instead. The physical interpretation of this fact is that for length scales of the order of particle interaction radii, a hydrodynamic description of the solvent does no longer hold. In appendix A, the plateau value $\eta V\widetilde{T}(k)$ is calculated for a MPC-SR solvent which is obtained by assuming molecular chaos, where all correlations among particles are absent. This calculation finally gives (see Eq. (A.24))

$$\eta V\widetilde{T}_{mc}(k) = \frac{\eta h}{2m\varrho}. \tag{5.25}$$

Note that this expression is independent of k. Here we used the subscript "mc" for "molecular chaos" in order to distinguish it from the other regimes. In Fig. 5.3 can be seen that the expression (5.25) agrees perfectly with the simulated data points at the plateau. Consequently, the crossover from $1/k^2$ to a constant value given by Eq. (5.25) is caused by a crossover from a hydrodynamic regime to molecular chaos. Therefore, the wave number k_c where the two lines given by $1/k^2$ and the plateau value intercept can be used to define the "hydrodynamic cutoff length" $\lambda_c = 2\pi/k_c$. Since analytic expressions of both lines are known, and the agreement between simulations and theory is perfect (see Fig. 5.3), we can calculate the hydrodynamic cutoff λ_c analytically. The wave number k_c at the intercept is

$$\begin{aligned} k_c &= \sqrt{\frac{2m\varrho}{\eta h}} \\ \lambda_c &= \frac{2\pi}{k_c} = \pi\sqrt{\frac{2\eta h}{m\varrho}} \end{aligned} \tag{5.26}$$

Using the analytic expressions (3.13 - 3.14) for the shear viscosity η of the MPC-SR solvent, we are able to calculate numerical values of λ_c depending on h.

The limit of λ_c for $h \to 0$ can even be predicted analytically. According to

Eq. (3.14), the shear viscosity η is dominated by η_{coll} in the limit of $h \to 0$. Replacing η in Eq. (5.26) by the analytic expression (3.15) for η_{coll} yields

$$\lim_{h\to 0} \lambda_c = \frac{\pi}{3}\sqrt{\left(1 - \frac{1}{\varrho}\right)(1 - \cos\alpha)}. \tag{5.27}$$

Inserting the parameters $\alpha = 130.0°$ and $\varrho = 10.0$ of our simulations, we find

$$\lim_{h\to 0} \lambda_c\,(\alpha = 130.0°, \varrho = 10.0) = 1.2733. \tag{5.28}$$

This is consistent with expectation, since at small length scales, we know that hydrodynamics must break down, because momentum is only conserved on the length scale of a collision box a and not particle-wise.

From Eq. (5.27) it can be concluded that the continuum limit $\lambda_c \to 0$ can be reached by lowering $\alpha \to 0$. This is also intuitively clear, since a vanishing collision angle hardly violates momentum conservation of each particle. However, since simulations of hydrodynamic systems require a sufficiently high Schmidt number, the double limit $h \to 0$ and $\alpha \to 0$ cannot be taken independently, but the condition $\alpha/h^2 \gg 1$ has to be fullfilled, as shown by Ripoll et al. [83]. With such small h, it is computationally not feasible to study the dynamics over long time scales.

5.4 Hydrodynamic screening in rod suspensions

There is no analytical theory which is able to predict hydrodynamic screening lengths for rod suspension. Screening length are also difficult to access in experiments. In Ref. [47], hydrodynamic screening lengths in dense rod suspensions are indirectly deduced from diffusion constants of tracer spheres. This experimental study will be discussed in more detail in Chap. 6. Calculating the hydrodynamic mobility tensor in Fourier space $\widetilde{\mathbf{T}}(\mathbf{k})$ during simulations of dense rod systems, we are now able to determine screening lengths very precisely.

The same model is used as in the simulations of Chap. 4 where self-diffusion constants of rod-like colloids are calculated. Details about the model can be found in Sec. 4.2.

Due to the presence of the rods, we expect hydrodynamic screening. Furthermore, we expect that hydrodynamic screening can be well described by the phenomenological ASCFE (5.8). This point is not trivially true, but it will turn out later that the simulation data indeed fit very well to the predictions of the

ASCFE – at least for a wide range of length scales.
Unfortunately, it is not straightforward to extract the screening lengths $\varkappa_\alpha^{-1}$ from $\widetilde{\mathbf{T}}(\mathbf{k})$ for all $\mathbf{k}$-vectors in the general anisotropic case. However, if one measures $\widetilde{\mathbf{T}}(\mathbf{k})$ only for those $\mathbf{k}$-vectors which are eigenvectors of $\mathbf{S}$, we are able to extract $\varkappa_x$, $\varkappa_y$ and $\varkappa_z$. In the case of our MPC-SR simulations of rod-like colloids, there are two different situations, which are discussed separately below.

Isotropic systems

For low concentrations, rods are oriented isotropically. In this case, there is only a single screening length $\varkappa^{-1}$, and hydrodynamics can be described by the isotropic Debye-Büche-Brinkman equation (5.2). This simple case is included in the more general description of the ASCFE, where $\mathbf{S}$ has a three-fold degenerated eigenspace with eigenvalue $\varkappa^2$. The expression (5.16) reduces to

$$\widetilde{\mathbf{T}}_s(\mathbf{k}) = \frac{1}{\eta V}\frac{1}{k^2+\varkappa^2}\left(\hat{\mathbf{I}} - \hat{\mathbf{k}}\otimes\hat{\mathbf{k}}\right) \tag{5.29}$$

Hence it follows that

$$\widetilde{T}_s(k) := \frac{1}{2}\mathrm{Tr}\,\widetilde{\mathbf{T}}_s(\mathbf{k}) = \frac{1}{\eta V}\frac{1}{k^2+\varkappa^2}. \tag{5.30}$$

On the other hand, for the trace of the numerically calculated $\widetilde{\mathbf{T}}(\mathbf{k})$, it follows from Eq. (5.19) that

$$\widetilde{T}(k) = \frac{1}{2}\mathrm{Tr}\,\widetilde{\mathbf{T}}(\mathbf{k}) = \frac{1}{2k_BT}\int_0^\infty dt\,\langle\tilde{\mathbf{v}}^*(\mathbf{k},0)\cdot\tilde{\mathbf{v}}(\mathbf{k},t)\rangle\,. \tag{5.31}$$

A rearrangement of Eq. (5.30) yields

$$\frac{1}{\eta V\widetilde{T}(k)} = k^2+\varkappa^2. \tag{5.32}$$

A plot of $1/(\eta V\widetilde{T}(k))$ vs. k^2 should give a straight line with slope 1 and an axis intercept of

$$b := \varkappa^2. \tag{5.33}$$

This line can be fitted, where the only fitting paramater is the axis intercept b. From b it is straightforward to get the screening length

$$\varkappa^{-1} = \frac{1}{\sqrt{b}}. \tag{5.34}$$

Since every possible **k**-vector is an eigenvector of **S**, one could, in principle, measure $\widetilde{\mathbf{T}}(\mathbf{k})$ for all accessible **k**'s given by (5.21). However, hydrodynamic screening influences the Fourier transformed mobility tensor $\widetilde{\mathbf{T}}(\mathbf{k})$ only significantly for small wave vectors. Therefore, the simulation box has to be large enough in order to get sufficient data points for $\widetilde{\mathbf{T}}(\mathbf{k})$ which are influenced by hydrodynamic screening. Furthermore, sampling all accessible **k**'s (given by Eq. (5.21)), one would end up with the same problem as in Sec. 5.3 that the statistical accuracy is not uniformly distributed for all $k = |\mathbf{k}|$. We decided to use the same sampling pattern of **k** space as used in Sec. 5.3 and visualized in Fig. 5.2.

Since all modes can be assumed to be statistically independent, the error $\Delta(\varkappa^{-1})$ of $\varkappa^{-1}$ can be obtained from the standard error Δb by error propagation using the relation (5.34),

$$\Delta(\varkappa^{-1}) = \Delta b \left| \frac{\partial}{\partial b} \frac{1}{\sqrt{b}} \right| = \frac{\Delta b}{2\sqrt{b}^3}. \tag{5.35}$$

An example of such a plot is shown in Fig. 5.4.a, where simulation data of $1/(\eta V \widetilde{T}(k))$ as well as the best fit to the theoretical curve (5.32) are plotted vs. k^2. The fitted line has clearly a positive axis intercept. Note that the slope of the line is given and not a fitting parameter. For large k ($k^2 > 10.0$), the data points don't lie on the expected line anymore since the continuous hydrodynamic description breaks down for too large wave vectors, as discussed in Sec. 5.3.

Also data points for very small k ($k^2 < 0.5$) don't lie on the line. They rather lie on another line with a larger slope and no axis intercept, as highlighted in Fig. 5.4.b. The explanation of this result is that on large scales, the distinction between solvent and colloids is not longer relevant, but the whole rod suspension can be considered as an unscreened fluid with an effective (macroscopic) viscosity η_{eff} which is larger than the solvent viscosity η. Therefore these data points are described by an "effective" mobility tensor $\widetilde{T}_{eff}(k)$ which is not screened ($\varkappa_{eff} = 0$) and corresponds to the effective (macroscopic) viscosity η_{eff}. Dhont and Briels [25] calculated the effective viscosity of a rod suspension. In the limit of zero shear, they predict an effective viscosity

$$\eta_{eff} = \eta \left(1 + \frac{8}{45} \frac{(L/d)^2}{\ln(L/d)} \phi \right) \tag{5.36}$$

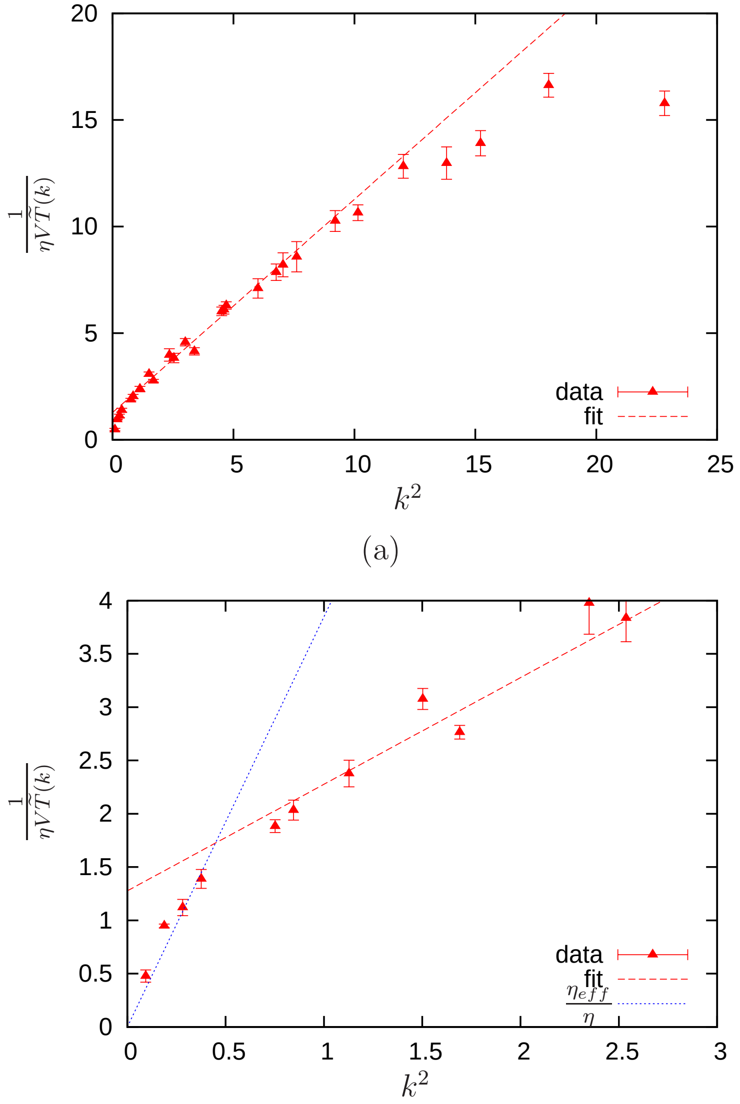

(a)

(b)

Figure 5.4: $1/(\eta V\widetilde{T}(k))$ vs. k^2 for a simulation of an isotropic rod system. Rods have an aspect ratio $L/d = 20$ and a volume fraction of $\phi = 0.18$. (a) Data points as well as the best fit to the theoretical curve $1/(\eta V\widetilde{T}_s(k)) = k^2 + \varkappa^2$ are shown for $0 < k^2 < 25$. From the axis intercept, the screening length $\varkappa^{-1}$ can be extracted. For the fit, only data points for $0.5 < k^2 < 10$ are taken into account. For $10 < k^2$, the onset of non-hydrodynamic behavior can be seen. (b) shows a magnification of (a) for small k^2 together with line η_{eff}/η, where η_{eff} is the effective viscosity predicted by Dhont and Briels [25].

where η is the solvent viscosity, L/d is the rod aspect ratio and ϕ is the volume fraction of the rods. In Fig. 5.4.b, also the corresponding line

$$\frac{1}{\eta V \widetilde{T}(k)} = \frac{\eta_{eff}}{\eta} k^2 \tag{5.37}$$

is plotted. One can see that the data points for $k^2 < 0.5$ can be well described by this curve.

Of course, these data points must not be taken into account for the calculation of the screening length $\varkappa^{-1}$. Therefore, only data points for $0.5 < k^2 < 10.0$ are used for the $\varkappa^{-1}$-fit.

Nematic systems

For higher concentrations, where rods form a nematic phase, the system has a preferential direction represented by the nematic director $\hat{\mathbf{n}}$. The two perpendicular directions in 3D space are equivalent. Due to this uniaxial anisotropy, hydrodynamic screening for shear waves with $\mathbf{k} \parallel \hat{\mathbf{n}}$ differs from hydrodynamic screening for waves with $\mathbf{k} \perp \hat{\mathbf{n}}$. Accordingly, there are two screening lengths $\varkappa_{\parallel}^{-1}$ and $\varkappa_{\perp}^{-1}$. In our simulations we have the possibility to set the nematic director $\hat{\mathbf{n}}$ to a desired direction. We have chosen $\hat{\mathbf{n}}$ to be the x-direction. Therefore the anisotropic screening tensor reads

$$\mathbf{S} = \begin{pmatrix} \varkappa_{\parallel}^2 & 0 & 0 \\ 0 & \varkappa_{\perp}^2 & 0 \\ 0 & 0 & \varkappa_{\perp}^2 \end{pmatrix} \tag{5.38}$$

which has the yz-plane as a two-fold degenerate eigenspace. The Fourier transformed hydrodynamic mobility tensor $\widetilde{\mathbf{T}}_a(\mathbf{k})$ still looks quite complicated for general $\mathbf{k}$. When only those $\mathbf{k}$ are considered which lie in one of the two eigenspaces of $\mathbf{S}$, $\widetilde{\mathbf{T}}_a(\mathbf{k})$ can be simplified drastically. Therefore we determine $\widetilde{\mathbf{T}}_a(\mathbf{k})$ only for those $\mathbf{k}$ which are either parallel or perpendicular to $\hat{\mathbf{n}}$. Also for nematic systems we have the problem that there are only few modes for long wave lengths but (in the case of $\mathbf{k} \perp \hat{\mathbf{n}}$) many modes for small wave length. Therefore we consider only those $\mathbf{k}$-vectors which fulfill Eq. (5.21) and lie on one of the lines:

- positive x, y, and z axes
- $y = \pm z$, with $x = 0$ and $y >= 0$

Let us now consider both eigenspaces independently:

$\mathbf{k} \parallel \hat{\mathbf{n}}$:

Eq. (5.16) simplifies in this case to

$$\widetilde{\mathbf{T}}_a(\mathbf{k}) = \frac{1}{V\eta(k^2 + \varkappa_\perp^2)} \begin{pmatrix} 0 & 0 & 0 \\ 0 & 1 & 0 \\ 0 & 0 & 1 \end{pmatrix}. \tag{5.39}$$

From this one can define

$$\widetilde{T}_\parallel(k) := \frac{1}{2}\mathrm{Tr}\,\widetilde{\mathbf{T}}_a(\mathbf{k}) = \frac{1}{2}\left(\widetilde{\mathbf{T}}_{\mathbf{a,yy}}(\mathbf{k}) + \widetilde{\mathbf{T}}_{\mathbf{a,zz}}(\mathbf{k})\right) = \frac{1}{V\eta(k^2 + \varkappa_\perp^2)}. \tag{5.40}$$

In simulations, $\widetilde{T}_\parallel(k)$ can be determined by

$$\widetilde{T}_\parallel(k) = \frac{1}{2k_BT}\int_0^\infty dt\,\left\langle \tilde{v}_y^*(\mathbf{k},0)\tilde{v}_y(\mathbf{k},t) + \tilde{v}_z^*(\mathbf{k},0)\tilde{v}_z(\mathbf{k},t)\right\rangle. \tag{5.41}$$

Plotting $1/(\eta V\widetilde{T}_\parallel(k))$ vs. k^2 for $\mathbf{k} \parallel \hat{\mathbf{n}}$, one expects again a straight line, which can be fitted similarly to the isotropic case. Thus the perpendicular screening length $\varkappa_\perp^{-1}$ together with its error can be extracted.

$\mathbf{k} \perp \hat{\mathbf{n}}$:

Eq. (5.16) similarly simplifies in this case to

$$\widetilde{\mathbf{T}}_a(\mathbf{k}) = \frac{1}{V\eta} \begin{pmatrix} \frac{1}{k^2+\varkappa_\parallel^2} & 0 & 0 \\ 0 & \frac{k_z^2}{k^2(k^2+\varkappa_\perp^2)} & -\frac{k_yk_z}{k^2(k^2+\varkappa_\perp^2)} \\ 0 & -\frac{k_yk_z}{k^2(k^2+\varkappa_\perp^2)} & \frac{k_y^2}{k^2(k^2+\varkappa_\perp^2)} \end{pmatrix}. \tag{5.42}$$

We define the quantity

$$\widetilde{T}_\perp(k) := \widetilde{\mathbf{T}}_{\mathbf{a,xx}}(\mathbf{k})) = \frac{1}{V\eta(k^2 + \varkappa_\parallel^2)}. \tag{5.43}$$

In simulations, $\widetilde{T}_\perp(k)$ is determined by

$$\widetilde{T}_\perp(k) = \frac{1}{k_BT}\int_0^\infty dt\,\langle \tilde{v}_x^*(\mathbf{k},0)\tilde{v}_x(\mathbf{k},t)\rangle \tag{5.44}$$

Plotting $1/(\eta V\widetilde{T}_\perp(k))$ vs. k^2 for $\mathbf{k} \perp \hat{\mathbf{n}}$, one expects again a straight line, which can be fitted similarly to the isotropic case. Thus the parallel screening length $\varkappa_\parallel^{-1}$ together with its error can be extracted.

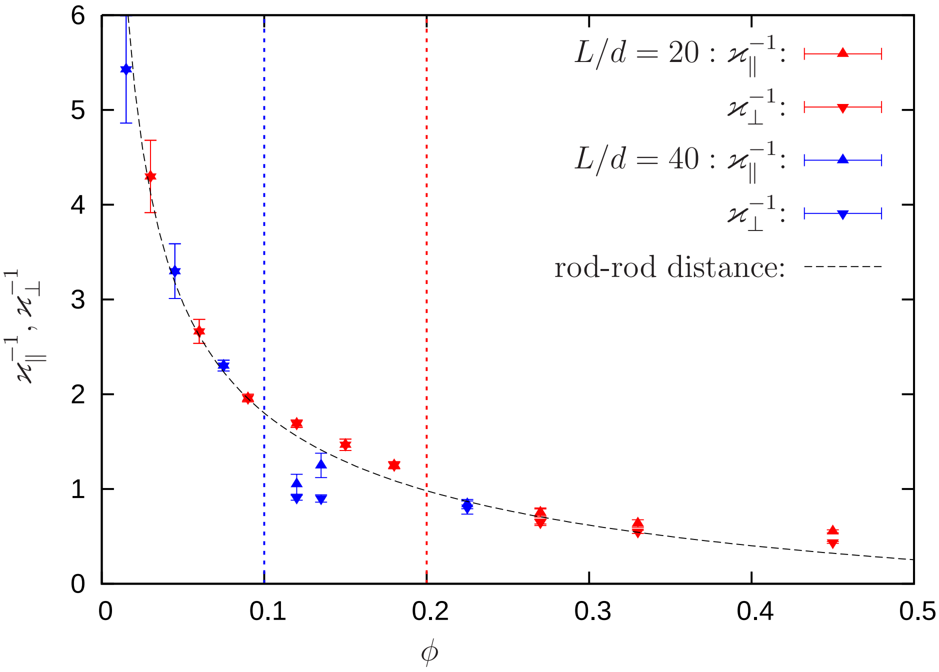

Figure 5.5: Concentration dependence of screening lengths $\varkappa_\parallel^{-1}$ and $\varkappa_\perp^{-1}$ for rods with $L/d = 20$ and $L/d = 40$. The dashed vertical lines indicate the I-N phase transition for $L/d = 20$ (red line) and $L/d = 40$ (blue line).

5.4.1 Concentration dependence of screening

We have performed a systematic study of the concentration dependence of screening lengths in rod suspensions for the two aspect ratios $L/d = 20$ and $L/d = 40$. In both cases, simulations of isotropic and nematic systems were carried out. The resulting screening lengths $\varkappa_\parallel^{-1}$ and $\varkappa_\perp^{-1}$ are shown in Fig. 5.5 as a function of the volume fraction ϕ. Since we expect the screening length to be of the order of typical rod-rod distances, also the concentration dependent length scale

$$B(\phi) := d\left(\sqrt{\frac{\pi}{4\phi}} - 1\right) \tag{5.45}$$

is plotted in Fig. 5.5, which is a rough estimate of the average lateral rod-rod distance in a very simplified model which is visualized in Fig. 5.6. If the rods are laterally aligned on a square grid, and the longitudinal distance A between rods vanishes, $B(\phi)$ is the perpendicular distance between two neighboring rods.

For small volume fractions ($\phi \leq 0.18$ for $L/d = 20$ and $\phi \leq 0.075$ for $L/d = 40$), the rod systems are in the isotropic phase and hence $\varkappa_{\parallel}^{-1}$ and $\varkappa_{\perp}^{-1}$ are identical, $\varkappa^{-1} = \varkappa_{\parallel}^{-1} = \varkappa_{\perp}^{-1}$. The simulated screening lengths $\varkappa^{-1}$ in the isotropic phase have a concentration dependence which agrees very well with that of the average rod-rod distance B. This confirms our expectation that screening lengths are of the order of typical rod-rod distances. The almost perfect agreement can be regarded as a coincidence, since the definition of a typical rod-rod distance $B(\phi)$ contains of course some arbitrariness.

For larger volume fractions, rods are in the nematic phase, where a small anisotropy in screening can be seen. For all our nematic systems, the parallel screening lengths $\varkappa_{\parallel}^{-1}$ lie above the perpendicular ones $\varkappa_{\perp}^{-1}$. In order to explain the anisotropy in screening, one has first to understand, how one stiff rod influences shear waves. The stiffness of the rod tends to keep solvent velocities constant along its whole length. For a particular shear wave with wave vector $\mathbf{k}$, the crucial length ξ_c over which velocities are coupled is of the order of $\xi_c \approx L\hat{\mathbf{u}} \cdot \hat{\mathbf{k}}$ which is the projection of the rod on the propagation direction $\hat{\mathbf{k}}$ of the shear wave. This becomes obvious when two special cases are considered. For shear waves perpendicular to the rod, each rod segment has the same phase in the wave such that it does not distort the velocity field. The other extreme is a rod with $\hat{\mathbf{u}} \parallel \hat{\mathbf{k}}$, for which the distortion of the velocity field is largest, and hence ξ_c and screening are maximal. A graphical explanation for this anisotropy is given in Fig. 5.7 where $\alpha = \measuredangle(\hat{\mathbf{u}}, \hat{\mathbf{n}})$. In contrast to the isotropic phase, screening lengths $\varkappa_{\parallel,\perp}^{-1}$ in the nematic phase decay only weakly with increasing concentration, see Fig. 5.5.

5.4.2 Effect of nematic order on screening

From Fig. 5.7.b, it can be expected that the parallel screening length $\varkappa_{\parallel}^{-1}$ strongly depends on the orientational order parameter $\langle P_2 \rangle$, since $\xi_c \approx L \sin\alpha$ is very sensitive to small changes in α for small angles deviations from the nematic director. Due to the weak α dependence of $L\cos\alpha$, for small α, perpendicular screening lengths $\varkappa_{\perp}^{-1}$ should be less sensitive to orientational disorder.

Indeed, our experimental cooperation partners of the group of J. K. G. Dhont [47] found an increase of the parallel screening length $\varkappa_{\parallel}^{-1}$ with increasing concentration in *fd* virus suspensions. This effect must be due to the increase in

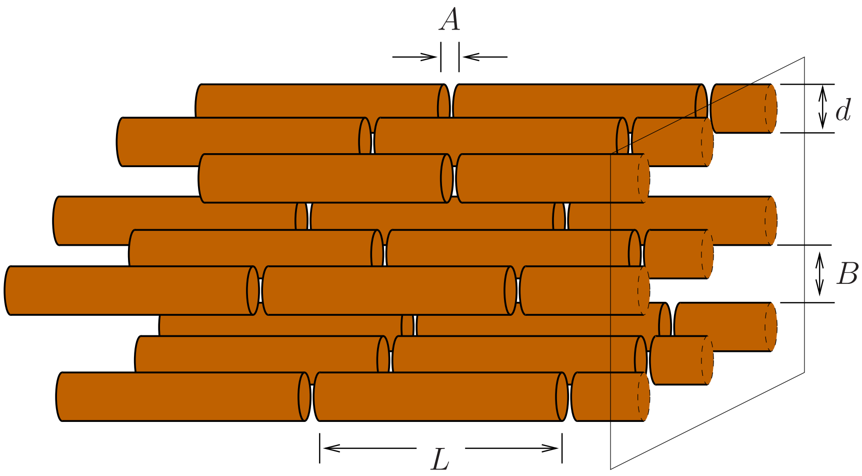

Figure 5.6: Visualization of the simple model, from which the average rod-rod distance $B(\phi)$ is derived.

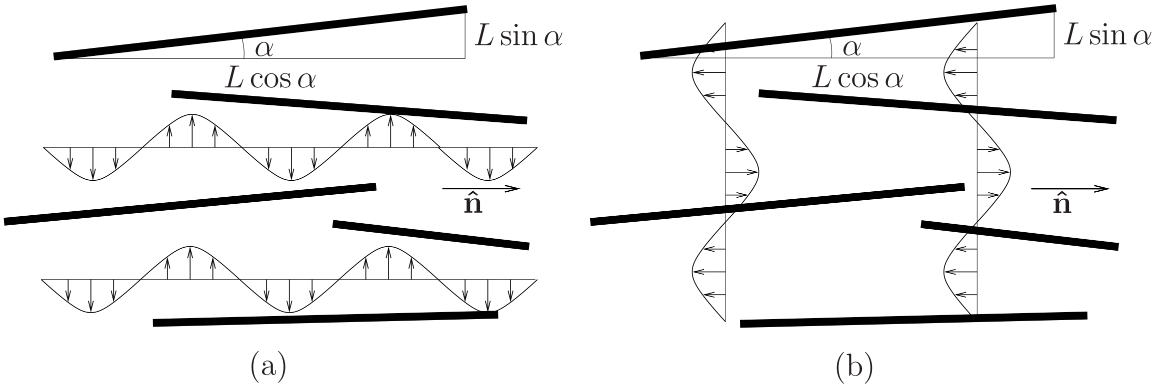

Figure 5.7: Origin of the anisotropy in hydrodynamic screening: Shear waves propagating (a) in a direction perpendicular to $\hat{\mathbf{n}}$ are hindered by rods more strongly than (b) those parallel to $\hat{\mathbf{n}}$. The stiffness of the rods couples solvent velocities over typical distances $\xi_c \approx L\cos\alpha$ for perpendicular shear waves and $\xi_c \approx L\sin\alpha (\ll L\cos\alpha)$ for parallel ones. Therefore, parallel screening length $\varkappa_{\parallel}^{-1}$ are typically larger than perpendicular ones $\varkappa_{\perp}^{-1}$.

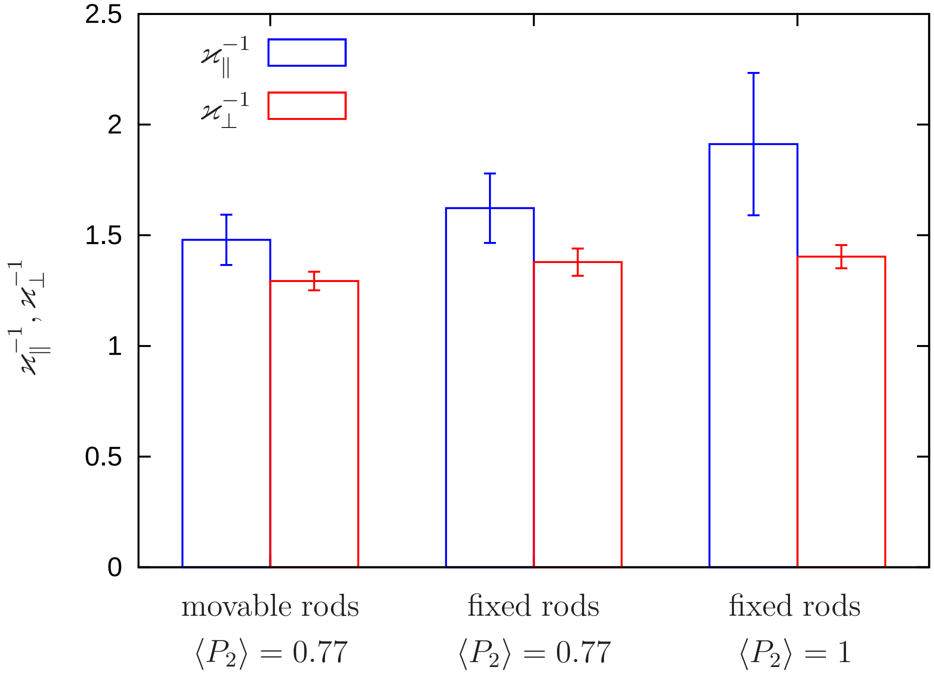

Figure 5.8: Parallel $\varkappa_{\parallel}^{-1}$ and perpendicular $\varkappa_{\perp}^{-1}$ screening lengths from simulations of rod suspensions with $L/d = 60$ and $\phi = 0.09$ with movable and fixed rods and different orientational order.

orientational order which is a consequence of increasing concentration.

We have not seen such an effect in the simulations presented in the previous Sec. 5.4.1. A possible reason is that, for the aspect ratios $L/d \leq 40$, orientational order only increases at comparably high volume fractions ϕ. For these high volume fractions, the average rod-rod distances are smaller than the hydrodynamic cutoff $\lambda_c(h = 0.1) = 1.31$ of our simulations. This means that there is not enough space between parallel rods to completely build up hydrodynamic interactions. Our results might be therefore dominated by thermal solvent motion rather than hydrodynamics for high ϕ.

In order to investigate the dependence of anisotropic screening on $\langle P_2 \rangle$, we decided to perform three extensive simulations using rods with $L/d = 60$ at a volume fraction of $\phi = 0.09$. For this volume fraction, we expect that neighboring rods are far enough from each other that hydrodynamic correlations between them are sufficiently developed. One simulation is done in the same way as the simulations of the previous section. The average nematic order parameter of rods with $L/d = 60$ at a volume fraction of $\phi = 0.09$ is $\langle P_2 \rangle = 0.77$.

In order to investigate rod systems with different orientational order, we take advantage of the fact that the nematic order parameter $\langle P_2 \rangle$ can be controlled independent of temperature and concentration. As an extreme case, we use perfectly parallel rods (i.e. $\langle P_2 \rangle = 1$) with fixed positions. Although rods do not move, their velocities are of interest, since they have to be coupled to the solvent in the collision step. The monomer velocities are therefore taken from a Maxwellian distribution with zero mean and a width of $\sqrt{k_B T/2M}$ (M being the monomer mass). This avoids cooling of solvent near the rods.

Of course, results of such simulations are not directly comparable with moving rods. In particular for long wave length (small k), we expect deviations from freely moving rods, since the rod suspension is artificially stuck to the resting frame for all wave lengths. For free rods, we saw in Sec. 5.4.1 that at long wave length, rods and solvent move collectively, and that the rod suspension can be regarded as an effective fluid with an effective viscosity η_{eff} which is generally higher than the solvent viscosity. In the suspension with fixed rods, there is no crossover to a different linear regime which would correspond to an unscreened fluid with $\eta_{eff} \neq \eta$.

In order to compare screening lengths of moving and fixed rods anyway, it has be checked, that the difference between the two systems does not influence hydrodynamic screening lengths. Therefore, we have performed a third simulation with fixed rods of the same aspect ratio $L/d = 60$ at the same volume fraction $\phi = 0.09$, where the order parameter has its equilibrium value $\langle P_2 \rangle = 0.77$. For this purpose, monomer positions where taken from one representative configuration of the simulation with freely moving rods. The results of these three simulations (with $L/d = 60$ and $\phi = 0.09$) are shown in Fig. 5.8. The screening lengths $\varkappa_{\parallel}^{-1}$ and $\varkappa_{\perp}^{-1}$ of simulations with $\langle P_2 \rangle = 0.77$ do not show any significant differences. Hence, the assumption is justified that dynamics of small wave length is not influenced by fixing the positions of the rods.

However, the simulation with $\langle P_2 \rangle = 1$ shows a distinctly more pronounced anisotropy in screening. In particular, the parallel screening length $\varkappa_{\parallel}^{-1}$ is larger, whereas the perpendicular one is unchanged (within the error bars). Even if the accuracy is not satisfactory, this implies that the experimentally observed increase in anisotropic screening [47] can be also seen in our simulations. Furthermore, this result is in agreement with the explanation depicted in Fig. 5.7.

5.4.3 Effect of volume exclusion on screening

Ahlrichs et al. [3] have shown by computer simulations that there is no hydrodynamic screening in semidilute solutions of phantom flexible polymers. They stated that hydrodynamic screening can only be caused by entanglements arising from excluded volume interactions.

However, our explanation of hydrodynamic screening (see Sec. 5.4.1) in rod suspensions does not rely on any non-hydrodynamic inter-rod interactions, but it is solely caused by the stiffness of rods. Therefore, hydrodynamic screening is also expected to occur in dense suspensions of phantom rods. In order to study the effect of excluded volume (EV) interactions on screening in rod suspensions, we performed three simulations of phantom rods with aspect ratio $L/d = 20$. The chosen volume fractions were $\phi = 0.12$, $\phi = 0.18$ and $\phi = 0.27$, because corresponding data of EV rod suspension exist. The results are shown in Fig 5.9.

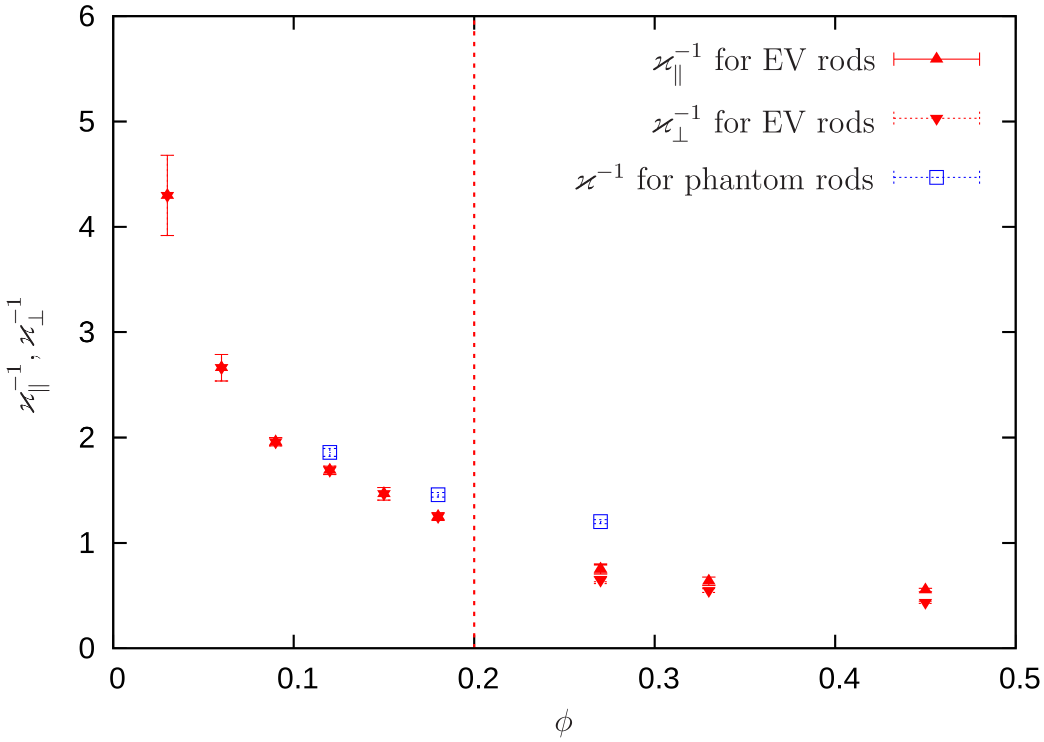

Figure 5.9: Screening lengths for suspensions of phantom (blue points) and EV rods (red points) with $L/d = 20$. The dashed perpendicular line indicates the I-N phase transition.

Since phantom rods cannot form a nematic phase, the data points for EV and phantom rods at $\phi = 0.27$ belong to different phases. Common for all three pairs of simulations is that screening lengths of phantom systems lie above those of the corresponding EV systems. Even if the difference is not strong, it is significant. The stronger hydrodynamic screening in EV systems arises from the fact that rods entangle. Thus it they can less easily follow the solvent flow which leads to higher hydrodynamic screening.

5.5 Summary and Conclusions

We constituted a phenomenological hydrodynamic equation, the ASCFE, which takes into account anisotropic hydrodynamic screening. The ASCFE was solved in Fourier space to give a theoretical expression for the Fourier transform of the hydrodynamic mobility tensor. Moreover, a procedure was introduced to calculate the Fourier transform of the hydrodynamic mobility tensor $\widetilde{\mathbf{T}}(\mathbf{k})$ from MPC-SR simulations. This concept was applied to different systems. Thus, we could show that the hydrodynamic cutoff in simple MPC-SR solvents obeys our theoretical prediction. From the simulated hydrodynamic mobility tensor of dense rod suspensions, we could extract hydrodynamic screening lengths by comparing it with the solution of the ASCFE. We found that hydrodynamic screening lengths decrease like typical rod-rod distances with increasing concentration. For nematic systems, a weak anisotropy in hydrodynamic screening was found which increases with increasing nematic order. Simulations of phantom rods led to the conclusion that hydrodynamic screening is weaker in the absence of steric rod-rod interactions.

The results of this chapter have consequences also for other chapters below. Based on our calculated screening lengths, theoretical expressions for tracer-sphere diffusion constants in rod suspensions will be evaluated in the next chapter. The good agreement between theory and simulations nicely confirms the validity of the screening-length determination. From a comparison between simulations of fixed and moving rods we could conclude that hydrodynamic screening on length scales far smaller than the rod length is independent of rod dynamics. Consequently, the tracer-sphere diffusion constants should be valid for a broad range of suspensions of rod-like macromolecules and colloids, such that they can be also transferred to, e.g., crossed-linked filament networks.

On large length scales, a crossover to a hydrodynamic regime could be found in simulations of moving rods, where rods and solvent can be regarded as one effective fluid which is not screened and has an effective viscosity larger than that of the pure solvent. The observed effective viscosity is in accordance with theory. The high effective viscosity of rod suspensions has the consequence that biological cells typically have a higher viscosity in their inside, as the cytoplasm often contains many filaments.

6 Diffusion of spheres in rod suspensions

The diffusion of spherical particles in crowded environment of filamentous structures is encountered in many soft materials and biological systems, like in F-actin networks. As a model system, we consider the diffusion of spheres in dense rod suspensions, where we focus on the regime of tracer sphere radii a_s which are considerably smaller than the mesh size ξ (see Eq. (2.18)) of the rod network and comparable to the rod diameter. Since these tracer particles are far smaller than the rods, sphere dynamics is much faster than the dynamics of the rod network. Therefore many details of rods, which are crucial for rod diffusion, are of minor importance for sphere diffusion. For example, a not too strong polydispersity of rods should not affect sphere dynamics significantly, as long as the static phase behavior is not influenced. Even tracer diffusion among cross-linked filaments should have comparable diffusion constants.

Another interesting aspect of tracer diffusion is that it offers insights into hydrodynamics of rod suspensions. In contrast to rod diffusion, there is a hydrodynamic theory of sphere diffusion [47, 48] which was developed by our cooperation partners in the group of J. K. G. Dhont. The theoretical predictions of sphere diffusion constants strongly depend on hydrodynamic screening lengths. In experiments, hydrodynamic screening lengths cannot be determined from fluctuations of shear waves of the solvent as it was done in our simulations (see Sec. 5.4). Therefore, the theory of Ref. [47, 48] was used to fit experimentally obtained sphere diffusion constants to hydrodynamic screening lengths. In contrast to experiments, computer simulations have the advantage that two strategies can be followed to obtain screening lengths: analyzing fluctuations of shear waves in the solvent as described in Sec. 5.4, and analyzing sphere diffusion constants. As we will see below, the simulated sphere diffusion constants can be predicted very well by the theory of Dhont et al. [47, 48] if screening lengths calculated in Sec. 5.4 are used. This consistency confirms both the theory and the validity of our computer simulations.

6.1 Scientific Background

The theory of Dhont et al. [47, 48] predicts diffusion constants of tracer spheres in dense rod suspensions taking into account both hydrodynamic and steric contributions. Since our simulations will be compared to the theory described in Ref. [47], its main results are summarized here.

In Sec. 2.6, it was discussed that in dense rod suspension with a rod volume fraction ϕ, sphere diffusion is not always isotropic – in contrast to infinite dilution. In nematic suspensions, two diffusion constants $D_{\|}(\phi)$ and $D_{\perp}(\phi)$ are expected due to the broken symmetry, whereas in isotropic systems, there is only one isotropic diffusion constant $D_{iso}(\phi)$.

In Ref. [47], it is shown that the ratio $D_{iso,\|,\perp}(\phi)/D_0$ between diffusion constants at finite volume fraction ϕ and that at infinite dilution is a product of a hydrodynamic, $1/(1+\phi\alpha^h_{iso,\|,\perp})$, and a steric contribution, $1-\phi\alpha^s_{iso,\|,\perp}$,

$$\frac{D_{iso,\|,\perp}(\phi)}{D_0} = \frac{1}{1+\phi\alpha^h_{iso,\|,\perp}}\left(1-\phi\alpha^s_{iso,\|,\perp}\right). \tag{6.1}$$

This apparently simple expression depends on the yet unknown coefficients $\alpha^h_{iso,\|,\perp}$ and $\alpha^s_{iso,\|,\perp}$. Their derivation is not straightforward. The final expressions for the steric coefficients $\alpha^s_{iso,\|,\perp}$ depend on the sphere radius a_s, the rod diameter d and for nematic systems also on the nematic order parameter $\langle P_2\rangle$:

$$\begin{aligned}
\alpha^s_{iso}\left(a_s,d\right) &= \frac{2}{3\nu}\left(1+\frac{2a_s}{d}\right)^2 && (6.2)\\
\alpha^s_{\|}\left(a_s,d,\langle P_2\rangle\right) &= \frac{2}{3\nu}\left(1+\frac{2a_s}{d}\right)^2\left(1-\langle P_2\rangle\right) && (6.3)\\
\alpha^s_{\perp}\left(a_s,d,\langle P_2\rangle\right) &= \frac{2}{3\nu}\left(1+\frac{2a_s}{d}\right)^2\left(1+\frac{1}{2}\langle P_2\rangle\right) && (6.4)\\
\text{with}\qquad \nu &= \frac{1}{2}\left(1+\sqrt{5}\right)=1.618... && (6.5)
\end{aligned}$$

The coefficients $\alpha^h_{iso,\|,\perp}$ do not have a closed analytic expression. Like $\alpha^s_{iso,\|,\perp}$, also the coefficients $\alpha^h_{iso,\|,\perp}$ depend on the sphere radius a_s, the rod diameter d, and the nematic order parameter $\langle P_2\rangle$. Furthermore, the $\alpha^h_{iso,\|,\perp}$ depend very sensitively on the hydrodynamic screening length $\varkappa^{-1}$. In Ref. [47], the procedure is explained how to calculate the coefficients $\alpha^h_{iso,\|,\perp}$. Since we have to perform this calculation for our particular system parameters, the procedure how to evaluate $\alpha^h_{iso,\|,\perp}$ in practice is explained in detail in appendix B. It should be mentioned that in Ref. [48] a closed analytic approximation for $\alpha^h_{iso,\|,\perp}$ has been developed which holds for suspensions of charged rods where the steric rod diameter is by far larger than the hydrodynamic diameter. However, it turns out that these expression do not apply to the conditions of our simulations.

6.2 Simulation details

Computer simulations using both the MPC-SR and the random MPC solvents allow us to determine the hydrodynamic and steric contributions to $D_{iso,\|,\perp}(\phi)/D_0$ independently. The simulation model used for pure rod systems (see Sec. 4.2) has been extended by addition of a small amount of spherical tracer particles. Such a spherical particle consists of a single monomer which has the same mass M as a rod monomer and interacts with other monomers (other spheres or other rod monomers) by the same shifted truncated Lennard-Jones potential $U_{LJ}(r)$ as defined by Eq. (4.11). This interaction is switched off in simulation of phantom spheres (see below).

As discussed in Sec. 4.3, the hydrodynamic sphere diameter which arises from our MPC parameters is $2a_s = a$ (a being the collision box size).

The amount of tracer spheres has to be very small, such that spheres hardly distort the rod network, and direct sphere-sphere interactions do not have a significant contribution to tracer dynamics. On the other hand, a not too small density of spheres is desirable in order to extract diffusion constants with good statistics. We chose a sphere density of $1/(7a)^3$. For higher densities, we found that spheres start to cluster, although no deviation in nematic order is noticeable.

For each pair of parameters L/d and ϕ, three different types of simulation were performed which allow us to study the hydrodynamic and steric contributions to $D_{iso,\|,\perp}(\phi)/D_0$ independently.

EV+HI spheres: The notation indicates that spheres interact with other colloids (other spheres or rods) both hydrodynamically (“+HI”) as well as by steric interactions due to their excluded volume (“EV”). Hydrodynamic interactions are taken into account by the MPC-SR solvent whereas steric interactions are realized by a repulsive Lennard-Jones potential (4.11) for the spheres. Diffusion constants obtained from simulations of EV+HI spheres will be denoted by $D^{hs}_{iso,\|,\perp}(\phi)$ in this chapter. Because of their frequent use, it is convenient to introduce additional symbols for the normalized diffusion constants

$$\widehat{D}^{hs}_{iso,\|,\perp}(\phi) := \frac{D^{hs}_{iso,\|,\perp}(\phi)}{D_0}. \tag{6.6}$$

We expect that $\widehat{D}^{hs}_{iso,\|,\perp}(\phi)$ can be described by Eq. (6.1)

$$\widehat{D}^{hs}_{iso,\|,\perp}(\phi) = \frac{D_{iso,\|,\perp}(\phi)}{D_0} = \frac{1}{1+\phi\alpha^{h}_{iso,\|,\perp}}\left(1-\phi\alpha^{s}_{iso,\|,\perp}\right) \tag{6.7}$$

EV–HI spheres: Using the random MPC solvent, all hydrodynamic interactions are switched off ("–HI") but the repulsive Lennard-Jones potential (4.11) is still applied to spheres such that steric excluded-volume (EV) interactions are taken into account. Thus we are able to isolate the steric contribution to $D_{iso,\|,\perp}(\phi)/D_0$ in Eq. (6.1). Diffusion constants obtained from simulations with EV–HI spheres are denoted by $D^{s}_{iso,\|,\perp}(\phi)$ and their normalized values are

$$\widehat{D}^{s}_{iso,\|,\perp}(\phi) := \frac{D^{s}_{iso,\|,\perp}(\phi)}{D_0}. \tag{6.8}$$

According to [47], it is expected that $\widehat{D}^{s}_{iso,\|,\perp}(\phi)$ obeys

$$\widehat{D}^{s}_{iso,\|,\perp}(\phi) = 1-\phi\alpha^{s}_{iso,\|,\perp} \tag{6.9}$$

Phantom spheres: The MPC-SR solvent is used but at the same time any steric excluded-volume interactions of spheres are switched off. We call these spheres "phantom spheres". However, steric rod-rod interactions are still present, in order to have the same static network properties. Thus, spheres interact only hydrodynamically with the rod network, and the steric contribution in Eq. (6.1) should vanish. Absolute and normalized diffusion constants obtained from simulations with phantom spheres are denoted by $D^{h}_{iso,\|,\perp}(\phi)$ and

$$\widehat{D}^{h}_{iso,\|,\perp}(\phi) := \frac{D^{h}_{iso,\|,\perp}(\phi)}{D_0}, \tag{6.10}$$

respectively. According to Ref. [47], $\widehat{D}^{h}_{iso,\|,\perp}(\phi)$ is expected to be given by

$$\widehat{D}^{h}_{iso,\|,\perp}(\phi) = \frac{1}{1+\phi\alpha^{h}_{iso,\|,\perp}}. \tag{6.11}$$

6.3 Results

A systematic study of the concentration dependence of tracer sphere diffusion constants was done for the two aspect ratios $L/d = 20$ and $L/d = 40$. The results of the normalized diffusion constants $\widehat{D}^{hs,s,h}_{iso,\|,\perp}(\phi)$ are shown in Fig. 6.1. Before coming to the results of phantom spheres in Sec. 6.3.2, results of simulation with volume exclusion of spheres (i.e. EV–HI and EV+HI spheres) will be discussed and compared to the theory of Dhont [47].

6.3.1 Spheres with volume exclusion

In Fig. 6.1, it can be seen that simulation results of $\widehat{D}^{s}_{iso,\|,\perp}$ for EV–HI spheres are generally larger than $\widehat{D}^{hs}_{iso,\|,\perp}$ obtained from simulations with EV+HI spheres. This fact is in accordance with the theory. Furthermore, there is a strong anisotropy in diffusion in the nematic phase for both EV–HI and EV+HI spheres. We also calculated $\widehat{D}^{hs}_{iso,\|,\perp}(\phi)$ and $\widehat{D}^{s}_{iso,\|,\perp}(\phi)$ by the theory of Dhont et al. [47]. For this purpose, the coefficients $\alpha^{s}_{iso,\|,\perp}$ were evaluated by inserting our system parameters into Eqs. (6.2) - (6.4). The coefficients $\alpha^{h}_{iso,\|,\perp}$ were calculated as described in appendix B. They depend very sensitively on hydrodynamic screening lengths $\varkappa^{-1}$. For the calculation of $\alpha^{h}_{iso,\|,\perp}$, we used the screening lengths $\varkappa^{-1}$ determined in Sec. 5.4. Since the anisotropic values $\alpha^{h,s}_{\|,\perp}$ also depend on nematic order parameters $\langle P_2 \rangle$ we inserted $\langle P_2 \rangle$ obtained from simulations. A comparison between the simulation data and the theoretical values of $\widehat{D}^{hs}_{iso,\|\perp}(\phi)$ and $\widehat{D}^{s}_{iso,\|,\perp}(\phi)$ is shown in Fig. 6.2. As can be seen, simulation results for isotropic diffusion $\widehat{D}^{hs,s}_{iso}(\phi)$ and diffusion in perpendicular direction $\widehat{D}^{hs,s}_{\perp}(\phi)$ are in perfect agreement with theory. This agreement nicely confirms both the validity of our screening-length calculations in Sec. 5.4 and the theory of Ref. [47]. For the aspect ratio $L/d = 20$, there are no theoretical values for $\rho \geq 6$. For these very high volume fractions $\phi = \rho d/L \geq 0.3$, the theory is not applicable, and the integrals which are involved in the calculation of $\alpha^{h}_{iso,\|,\perp}$ diverge.

Also normalized diffusion constants $\widehat{D}^{hs,s}_{\|}(\phi)$ for diffusion along the nematic director qualitatively follow the ϕ dependence of the theory. However, the deviations are stronger than for $\widehat{D}^{hs,s}_{iso,\perp}(\phi)$. Moreover, there is a systematic trend that all simulation results of $\widehat{D}^{hs,s}_{\|}(\phi)$ are smaller than the theoretical values. We can relate this deviation to the fact that the dependence of $\widehat{D}^{hs,s}_{\|}$ on the nematic order parameter $\langle P_2 \rangle$ predicted by Dhont et al. [47] is not a sufficient description

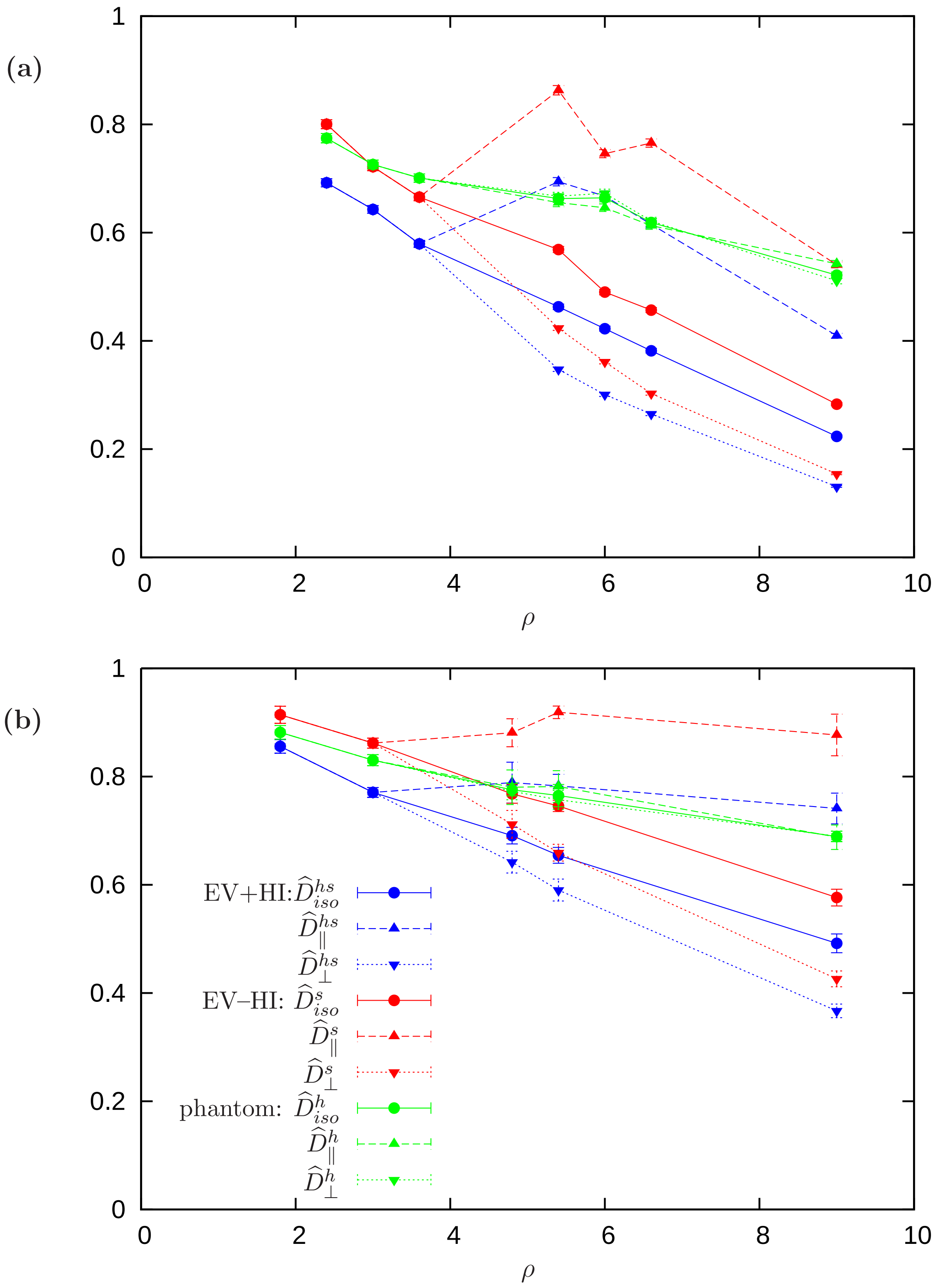

Figure 6.1: Dependence of the normalized diffusion constants $\widehat{D}^{hs,s,h}_{iso,\parallel\perp}$ on the dimensionless concentration ρ for the two aspect ratios (a) $L/d = 20$ and (b) $L/d = 40$. Symbols are explained in (b) for both plots.

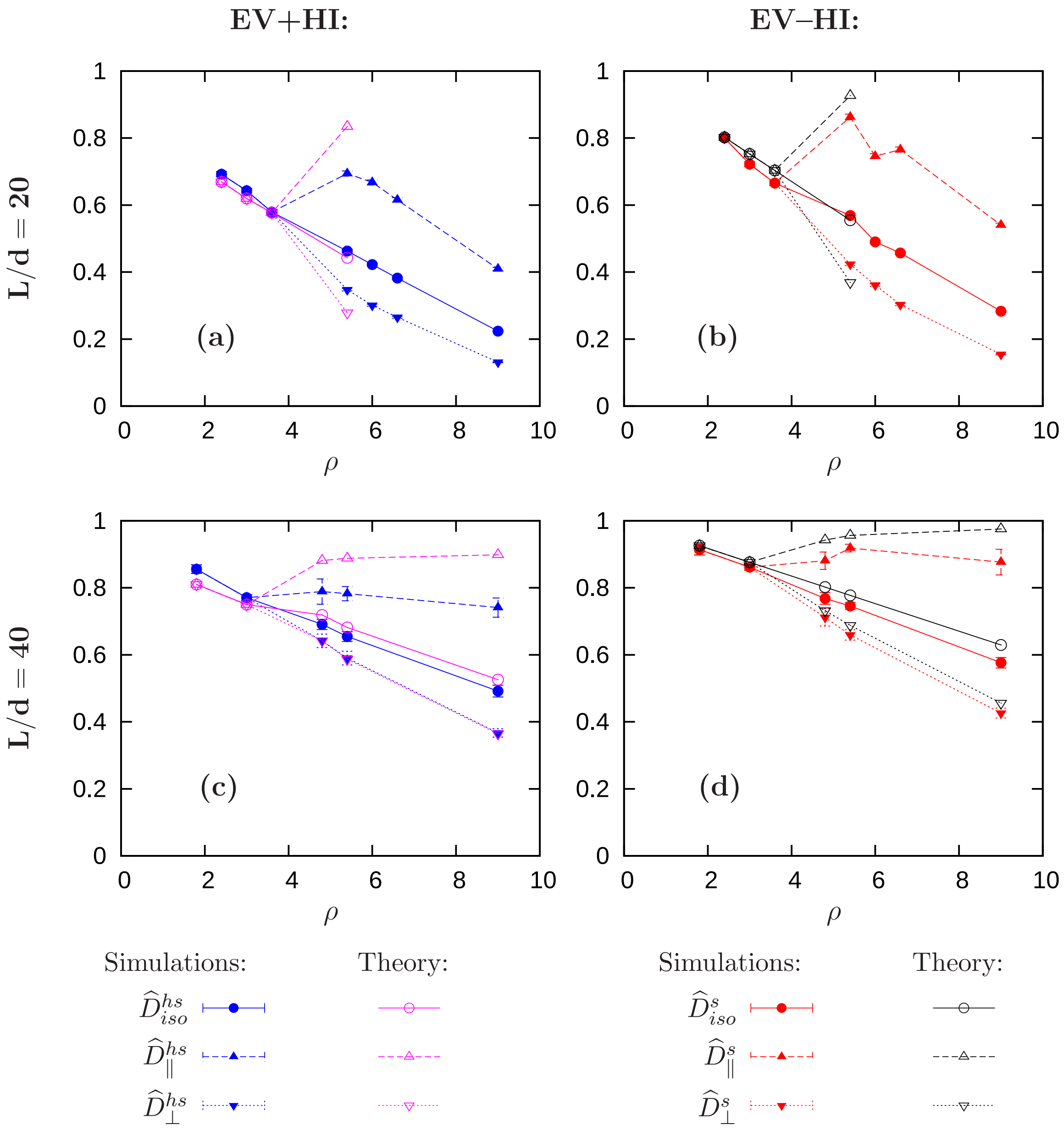

Figure 6.2: Normalized diffusion constants $\widehat{D}^{hs,s}_{iso,\|,\perp}$ as functions of the dimensionless rod concentration ρ. Simulation data and theoretical predictions according to the theory of Dhont et al. [47] for systems (a and c) with EV+HI and (b and d) EV–HI spheres for the aspect ratios (a and b) $L/d = 20$ and (c and d) $L/d = 40$.

of the problem for semiflexible rods, as the theory is based on stiff rods. Furthermore, the nematic order strongly fluctuates for the relatively small system sizes used in the simulations. The effect of both semiflexibility and fluctuations in nematic order is less crucial for diffusion perpendicular to the nematic director. An intuitive explanation of this observation can be given analogously to the $\langle P_2 \rangle$ dependence of hydrodynamic screening lengths (see Fig. 5.7 in Sec. 5.4.1): A small tilt of rods with respect to the nematic director (i.e. a nematic order parameter $\langle P_2 \rangle$ closed to 1) does not significantly open gaps in the network for diffusion in perpendicular direction. Also fluctuations of the flexible rods do not significantly hinder spheres in their motion perpendicular to $\hat{\mathbf{n}}$. However, diffusion in parallel direction is far stronger influenced by both small tilts and fluctuations of rods. Both effects strongly hinder tracer spheres in their diffusion along the nematic director.

6.3.2 Phantom spheres

In Fig. 6.1, also normalized diffusion constants $\widehat{D}^{h}_{iso,\parallel,\perp}$ of phantom spheres are shown. In contrast to systems with volume exclusion, hardly any anisotropy in diffusion is found for phantom spheres.

Astonishingly, there are some data points where even $\widehat{D}^{hs}_{\parallel} > \widehat{D}^{h}_{\parallel}$, i.e. diffusion of phantom spheres is slowed down more strongly than for spheres interacting both hydrodynamically and sterically. Obviously, our simulations do not obey the expected relation

$$\widehat{D}^{hs}_{iso,\parallel\perp}(\phi) = \widehat{D}^{s}_{iso,\parallel\perp}(\phi)\,\widehat{D}^{h}_{iso,\parallel\perp}(\phi). \tag{6.12}$$

This becomes even more obvious considering Fig. 6.3, where both sides of Eq. (6.12) are plotted independently. The fact that these curves do not coincide shows that Eq. (6.12) cannot be an appropriate description. However, the reason of this mismatch is very simple; the assumption that hydrodynamic sphere-rod interactions are equal for EV+HI and phantom spheres is incorrect. Since spheres are allowed to penetrate rods in phantom MPC systems, there is a considerable probability to find spheres overlapping with rods. This probability is larger for larger volume fraction. Hence, there is a significant amount of spheres which overlap with rod monomers such that hydrodynamic interactions are far stronger. In the continuum picture, the explanation is that the hydrodynamic mobility tensor typically increases enormously for small distances; this

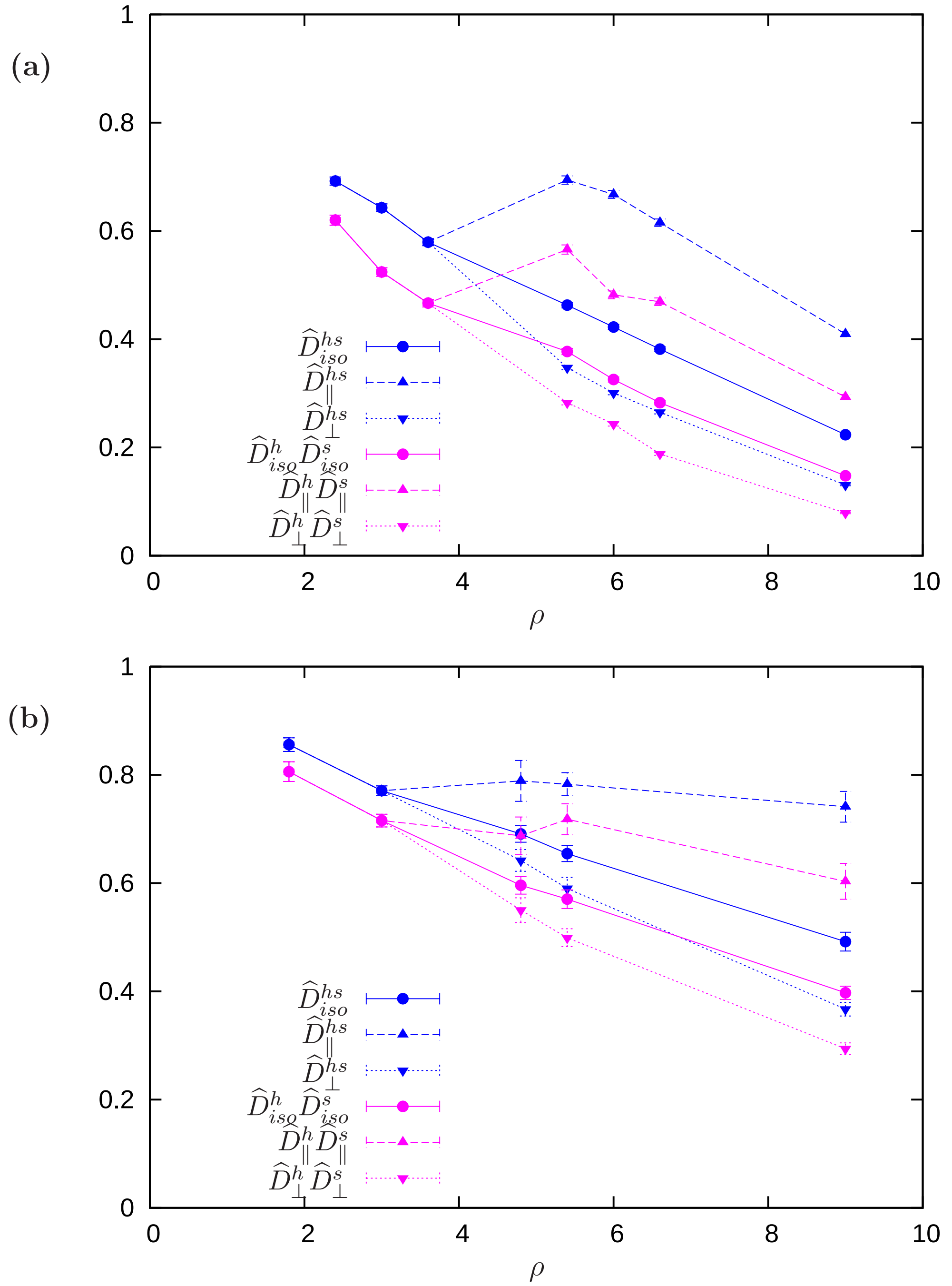

Figure 6.3: Test of the validity of Eq. (6.12) (a) for $L/d = 20$ and (b) for $L/d = 40$. The fact that the $\widehat{D}^{hs}_{iso,\|,\perp}$ (blue curves) do not coincide with $\widehat{D}^{h}_{iso,\|,\perp} \cdot \widehat{D}^{s}_{iso,\|,\perp}$ (magenta curves) shows that diffusion constants of EV+HI spheres are not related to the diffusion constants of EV–HI and phantom spheres systems by the simple relation (6.12).

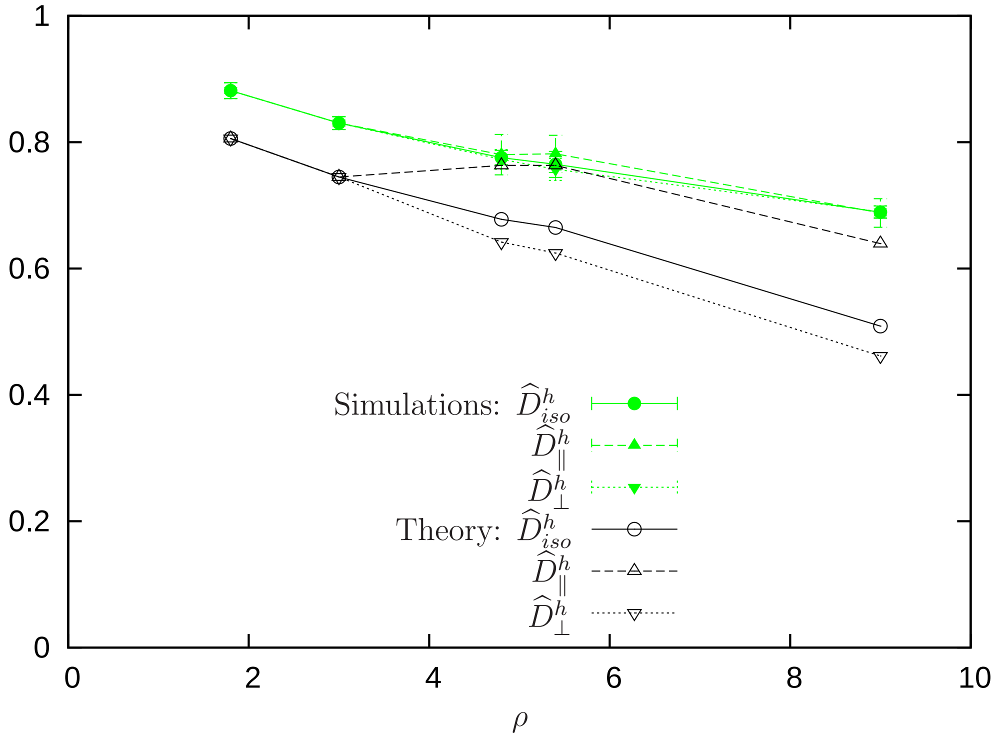

Figure 6.4: Normalized diffusion constants of phantom sphere simulations together with the prediction according to the theory of Dhont et al. [47]. In the calculation of the theoretical values, the constant probability density of phantom spheres was used. This difference in probability densities is responsible for the shift of $\alpha^h_{iso,\parallel,\perp}$ compared to systems with volume exclusion of spheres, since the volume exclusion causes a vanishing probability density for sphere positions which lie in the excluded volume.

holds for both the screened, Eq. (5.4), and the unscreened, Eq. (2.4), hydrodynamic mobility tensor. Although the continuum picture is not directly transferable to MPC-SR hydrodynamics at small length scales (compare Sec. 5.3), the effect is similar. It has been shown by Ripoll et al. [83] that diffusion of heavy phantom particles decreases with increasing concentration, as the probability of finding more than one heavy particle in the same collision box increases with concentration. This effect is not present in simulations of EV+HI and EV–HI spheres, because volume exclusion leads to a negligibly small probability to find two monomers in the same collision box.

We have applied the theory of Dhont et al. [47] also to phantom spheres. For this purpose, we calculate $\alpha^h_{iso,\|,\perp}$, which differ from those of the previous section by the fact that the Boltzmann probability is unity for all relative sphere-rod distances whereas the coefficients $\alpha^h_{iso,\|,\perp}$ of spheres with volume exclusion are calculated with a vanishing Boltzmann probability for relative sphere-rod distances for which sphere and rod overlap, as explained in appendix B. The normalized diffusion constants $\widehat{D}^h_{iso,\|,\perp}$ arising from this calculation are plotted in Fig. 6.4 together with the simulation data for $L/d = 40$. The mismatch of simulated (green) and theoretical curves (black) in Fig. 6.4 is due to the fact that the continuum hydrodynamic description does not hold for the MPC-SR solvent for distances smaller than the hydrodynamic cutoff (see Sec. 5.3).

6.4 Summary and conclusion

Simulations of tracer spheres in dense rod suspensions were performed for spheres with volume exclusion both with (EV+HI) and without hydrodynamic interactions (EV–HI), as well as for hydrodynamically interacting phantom spheres without volume exclusion. Diffusion constants were calculated from simulations and compared to the theory of Dhont et al. [47]. Screening lengths which were extracted from the Fourier transform of the hydrodynamic mobility tensor (see Sec. 5.4) were used for the evaluation of the theoretical diffusion constants. For spheres with volume exclusion (EV+HI and EV–HI) a good agreement between simulations and theory was found, which confirms both the theory as well as the calculation of screening lengths in the last chapter. Deviations from the theory for diffusion constants in parallel direction could be related to fluctuations of the nematic order parameter and of the rod shapes due to their flexibility. The hydrodynamic influence on sphere diffusion is different for spheres with (EV+HI spheres) and without volume exclusion (phantom spheres) because hydrodynamic interactions between spheres and rods with overlapping volumes are only present for phantom spheres. The theory is not applicable to phantom spheres – even when their uniform probability density is taken into account – because overlapping spheres and rods have distances below the hydrodynamic cutoff where hydrodynamic interactions are not properly mediated by the MPC-SR solvent.

7 Vesicles in shear flow

7.1 Scientific background

7.1.1 Vesicles

Vesicles are small fluid droplets enclosed by a membrane. Typically these membranes consist of amphiphilic phospholipid molecules which arrange in a bilayer structure. Lipid bilayer vesicles are very useful model systems for many biophysical phenomena and are interesting as soft mesoscopic objects in general. Neglecting all the microscopic details which are of course essential for living systems, many biological cells, such as blood cells, behave in many aspects like vesicles [13]. Also on a sub-cellular level, many organelles by themselves are vesicles, and material transport is often realized by transporting liquid cargo wrapped into a membrane.

The physical origin of the aggregation of phospholipid molecules in lipid bilayers is the hydrophobic effect. The energetic costs for a lipid molecule to leave the membrane is of the order of many $k_B T$ under physiological conditions which makes membranes very stable aggregates. However, the lipid molecules can freely move in the in-plane direction of the membrane. Therefore, membrane molecules can diffuse around and rearrange as a response to planar stress. The total membrane area is hardly compressible and can be regarded as conserved. Thus, the lipid bilayer membrane is a two-dimensional incompressible liquid which comes along with a two-dimensional membrane viscosity.

Typically, vesicles have sizes of the order of micrometers, whereas the thickness of the membrane is only of the order of nanometers. The membrane can be therefore regarded as a $(d_{dim} - 1)$ dimensional manifold (i.e. a plane in three-dimensional systems and a line in two-dimensions). However, the finite thickness of the lipid-bilayer membrane causes a curvature-dependent elastic energy, called bending energy. In three-dimensions (i.e. two-dimensional membranes), the local curvature can be characterized by the two principal radii of local curvature

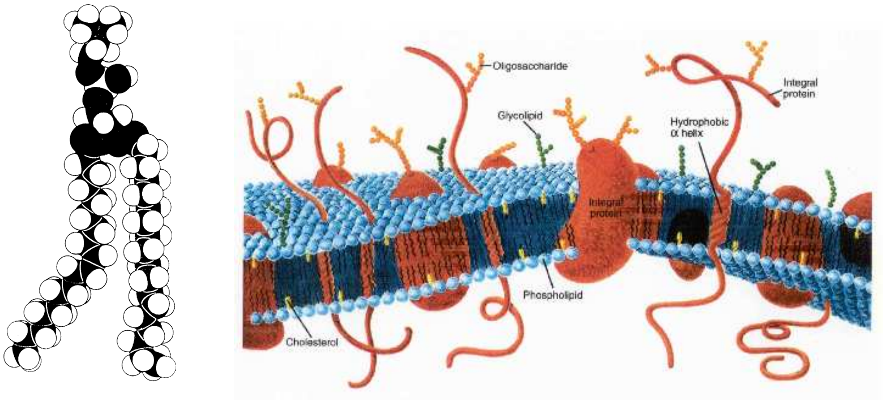

(a) (b)

Figure 7.1: (a) Schematic representation of a lipid molecule – which consists of a hydrophilic head and two hydrophobic hydrocarbon tails. The kink in one of the hydrocarbon chains is due to a C-C double bond and it is responsible for the fluidity of the membrane. (b) Schematic representation of a biological membrane which is composed of lipid molecules. Also embedded transmembrane proteins as well as cholesterol molecules are shown. Taken from Ref. [97].

R_1 and R_2, or equivalently by the mean curvature $\frac{1}{2}(\frac{1}{R_1}+\frac{1}{R_2})$ and the Gaussian curvature $\frac{1}{R_1 R_2}$. Typically, the energy costs for bending the membrane is governed by the mean curvature squared. However, in the two-dimensional case of our simulations, the membrane reduces to a one-dimensional interface where the curvature is quantified by only one curvature radius. The energy penalty for bending the (one-dimensional) membrane is characterized by a bending rigidity like for the semiflexible rods (see Chap. 4). Furthermore, there is no membrane viscosity in two-dimensional vesicles.

Important parameters of a two-dimensional vesicle are the perimeter P and the enclosed area A (analogous to the membrane surface and the enclosed volume in three dimensions). It is useful to combine these two parameters to a dimensionless quantity, the reduced area

$$A^* := \frac{4\pi A}{P^2}. \tag{7.1}$$

A^* is the ratio between the enclosed area A and the area of a circle with the same perimeter P. Only those combinations of A and P are reasonable which lead to $0 < A^* \leq 1$. The maximal value $A^* = 1$ corresponds to a perfect circle. In this chapter, we chose a reduced area of $A^* = 0.7$ as a representative for moderately aspherical vesicles.

In Chap. 5, we have seen that suspensions of rod-like colloids can be regarded as an effective fluid on length scales much larger than the size of the solute particles. This leads to a macroscopic viscosity η_{eff} which is larger than the pure solvent viscosity η (see Eq. (5.36)). The cytoplasm, i.e. the interior of a biological cell, is often comparable to such rod suspensions, since it contains many filamentous structures like F-actin or microtuboli. Although the cytoplasm is far more complex than a pure monodisperse rod suspension, it has typically a higher viscosity than the surrounding plasma, as explained by the results of Chap. 5. Therefore, we consider different viscosities inside η_{in} and outside $\eta_{out} \leq \eta_{in}$ of vesicles. Instead of using η_{in} and η_{out}, it is convenient to express relations in terms of the dimensionless "viscosity contrast"

$$\tau = \frac{\eta_{in}}{\eta_{out}}. \tag{7.2}$$

Below, we will see that several dynamical phenomena depend very sensitively on this quantity.

7.1.2 Shear flow

Linear shear flow can be described by the velocity-gradient tensor $\mathbf{\Gamma}$ which relates positions $\mathbf{r}$ to velocities $\mathbf{v}$ by

$$\mathbf{v}(\mathbf{r}) = \mathbf{\Gamma}\mathbf{r} + \mathbf{v}_h. \tag{7.3}$$

In the general case, also a homogeneous component $\mathbf{v}_h$ is possible; however, it can easily be avoided by a Galilei transformation to a comoving frame. The incompressibility condition $\nabla \cdot \mathbf{v} = 0$ requires that $\mathbf{\Gamma}$ is traceless. In the following, the case of simple shear flow is considered, where $\mathbf{v}_h = 0$ and the velocity-gradient tensor is

$$\mathbf{\Gamma} = \dot{\gamma} \begin{pmatrix} 0 & 1 & 0 \\ 0 & 0 & 0 \\ 0 & 0 & 0 \end{pmatrix}. \tag{7.4}$$

The resulting flow profile $\mathbf{v}(\mathbf{r}) = \mathbf{\Gamma}\ \mathbf{r}$ has only velocity components in x direction. In the representation of Eq. (7.4), the x direction is therefore called the "shear direction", whereas the y and z directions are the "gradient" and

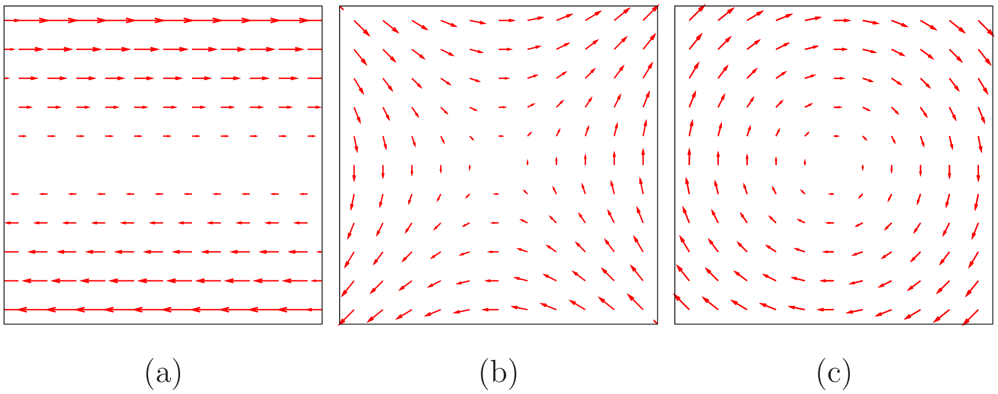

Figure 7.2: The velocity field of (a) simple shear flow and its decomposition into (b) the elongational and (c) the rotational part.

"vorticity directions", respectively. The shear rate $\dot{\gamma}$ quantifies the strength of the shear flow and is equal to $\partial v_x/\partial y$. Decomposing $\mathbf{\Gamma}$ into a symmetric part $\mathbf{E} = \frac{1}{2}\left(\mathbf{\Gamma} + \mathbf{\Gamma}^T\right)$ and an antisymmetric part $\mathbf{\Omega} = \frac{1}{2}\left(\mathbf{\Gamma} - \mathbf{\Gamma}^T\right)$, simple shear flow can be regarded as a superposition $\mathbf{v}(\mathbf{r}) = \mathbf{v}_e(\mathbf{r}) + \mathbf{v}_r(\mathbf{r})$ of an elongational

$$\mathbf{v}_e(\mathbf{r}) := \mathbf{E}\,\mathbf{r} = \frac{1}{2}\dot{\gamma}\begin{pmatrix} 0 & 1 & 0 \\ 1 & 0 & 0 \\ 0 & 0 & 0 \end{pmatrix}\mathbf{r} \tag{7.5}$$

and a rotational part

$$\mathbf{v}_r(\mathbf{r}) := \mathbf{\Omega}\,\mathbf{r} = \frac{1}{2}\dot{\gamma}\begin{pmatrix} 0 & 1 & 0 \\ -1 & 0 & 0 \\ 0 & 0 & 0 \end{pmatrix}\mathbf{r}. \tag{7.6}$$

The three velocity fields are shown in Fig. 7.2.
It is often convenient to consider the effects of the elongational and the rotational components to explain phenomena in simple shear flow.

7.1.3 Dynamical regimes of vesicles in shear

Aspherical vesicles under shear can be found in different dynamical phases. For small viscosity contrasts, vesicles are in the tank-treading (TT) regime. As the name already implies, the vesicle shape and orientation remain unchanged in this regime (besides fluctuations), but the membrane rotates around the enclosed area in the same direction as the rotational part of the shear flow. Λ_{max} and Λ_{min} are the two eigenvalues of the gyration tensor of the vesicle membrane ($\Lambda_{min} \leq \Lambda_{max}$) and $\hat{\mathbf{e}}_{max}$ and $\hat{\mathbf{e}}_{min}$ their corresponding eigenvectors. We quantify the shape asymmetry by

$$\alpha_s = \frac{\Lambda_{max} - \Lambda_{min}}{\Lambda_{max} + \Lambda_{min}} \tag{7.7}$$

and the vesicle orientation by the inclination angle

$$\theta = \measuredangle(\hat{\mathbf{x}}, \hat{\mathbf{e}}_{max}). \tag{7.8}$$

For larger viscosity contrasts τ, the inclination angle becomes unstable and either a transition to a tumbling (TB) motion or a swinging (SW) motion can be observed. In the tumbling regime, the inclination angle θ rotates, whereas the vesicle shape only experiences small periodic changes (i.e. α_s is almost unchanged). In the swinging regime, the inclination angle oscillates but does not perform full rotations. Also the periodic changes in shape are typically stronger in the SW regime.

The stability of these dynamical phases mainly depends on two parameters, the viscosity contrast τ and the reduced shear rate

$$\dot{\gamma}^* := \frac{\dot{\gamma}\eta R_p^2}{\kappa}. \tag{7.9}$$

Here $R_p = \frac{P}{2\pi}$ is the radius of a circle with the same perimeter P as that of the vesicle. The time $\eta R_p^2/\kappa$ is a typical relaxation time towards the equilibrium shape. Thus $\dot{\gamma}^*$ expresses the interplay between the perturbation by the external field $\dot{\gamma}$ and the ability of the vesicle to restore its equilibrium shape.

Without thermal fluctuations, the dynamical phase diagram as a function of τ and $\dot{\gamma}^*$ is partitioned into the three dynamical phases (TT, TB and SW) by sharp transitions. Such a phase diagram is shown in Fig. 7.3. Thermal fluctuations lead to smooth transitions between the three phases. We first focus on theories which neglect thermal fluctuations, such that sharp transition lines can be predicted.

As one can see in Fig. 7.3, the TT-TB transition line hardly depends on the reduced shear rate $\dot{\gamma}^*$ below the bifurcation point, and only the viscosity contrast τ is decisive for phase stability. The physical origin of the formation of these three phases can be explained by simple arguments. In the following, the origin of the TT and TB motion is explained; the intuitive explanation for the SW regime will be given later, after the theory of Keller and Skalak [50] has been discussed.

For $\dot{\gamma}^*$ far below the bifurcation point, the vesicle shape can be assumed to be that at equilibrium. The symmetric (elongational) and asymmetric (rotational) components of the shear flow have two counteracting effects. The elongation flow field tends to elongate the vesicle such that its long axis points into the $x = y$ direction, which corresponds to an inclination angle of $\theta = \frac{\pi}{4}$. However, the rotational part of the shear causes a torque on the vesicle membrane. In the case of low viscosity contrasts, the torque due to the rotational flow turns the inclination angle to values $\theta < \frac{\pi}{4}$. At a certain inclination angle θ the elongational part of the shear flow counteracts the torque on the vesicle due to rotational flow, which leads to a stable inclination angle $0 < \theta < \frac{\pi}{4}$. Although θ does not change in time, the torque on the membrane due to the rotational flow is still present. It causes the membrane to rotate around the vesicle in a tank-treading fashion. Fig. 7.6.a shows a sequence of snapshots of a tank-treading vesicle obtained from simulations, where the clock-wise tank-treading motion of the membrane can be followed due to the marker on the membrane. The no-slip-boundary condition between the membrane and the inner fluid has the effect, that there is a permanent viscous energy dissipation in the interior of the vesicle. For very high viscosity contrasts, the vesicle can be regarded as a rigid ellipse, and the torque on the membrane cannot lead to a tank-treading motion. Instead the torque causes a permanent rotation of θ. In this case, the vesicle is in the tumbling regime. The name “tumbling” expresses that the angular velocity of the vesicle is not uniform, as shown in the sequence of snapshots of a tumbling vesicle in Fig. 7.6.c. Since the velocity gradients in the internal fluid are stronger for more aspherical vesicles, the critical viscosity contrast τ^* of the TT-TB transition decreases with decreasing reduced area A^*.

7.1.4 Keller Skalak theory in two dimensions

Keller and Skalak [50] were the first who derived analytical expressions for the inclination angle θ and the average angular velocity ω for three-dimensional vesicles of fixed ellipsoidal shape. The Keller-Skalak (KS) theory was nicely confirmed both by computer simulations [71, 72] as well as by numerical Oseen tensor calculations [9]. Also the critical viscosity contrast τ^* of the TT-TB phase transition is well predicted by Keller and Skalak.

Although the KS theory is formulated for vesicles in three dimensions, it is straightforward to transfer it to two-dimensional systems by simply making one half-axis of the ellipsoid infinitely large. The resulting cylindrical three-dimensional geometry is equivalent to two-dimensional vesicles with the shape of an ellipse.

For such a vesicle, it is convenient to parametrize its shape by the long and the small half-axes a_1 and a_2, respectively. Let S' be the frame which has its origin at the center of the ellipse, and the x' direction points into the direction of the long axis. Then the local velocity $\mathbf{v}'$ of an element of the tank-treading membrane is assumed to be

$$v'_x = -\omega \frac{a_1}{a_2} x'_2 \tag{7.10}$$

$$v'_y = \omega \frac{a_2}{a_1} x'_1 \tag{7.11}$$

in the frame S'. We define the auxiliary variables

$$r_2 := \frac{a_2}{a_1} \qquad z_1 := \frac{1}{2}\left(\frac{a_1}{a_2} - \frac{a_2}{a_1}\right) \qquad z_2 := 2\frac{a_1^2 + a_2^2}{(a_1 + a_2)^2}.$$

Balancing torques on the membrane and assuming that the work done on the vesicles by the shear flow is dissipated in the interior of the vesicle, a non-linear differential equation can be constituted

$$\dot{\theta} = \frac{\dot{\gamma}}{2}\left[-1 + B\cos(2\theta)\right] \tag{7.12}$$

$$\text{with} \qquad B = \frac{(1 - r_2^2)^2 \left[z_2(1-\tau) - 2\right] - 8r_2^2}{(1 - r_2^4)\left[z_2(1-\tau) - 2\right]}. \tag{7.13}$$

Furthermore, the average angular velocity ω is calculated to be

$$\frac{\omega}{\dot{\gamma}} = -\frac{1}{z_1}\frac{\cos(2\theta)}{z_2(1-\tau) - 2}. \tag{7.14}$$

The stationary inclination angle θ of the tank-treading regime can be calculated from Eq. (7.12) with the condition that $\dot{\theta} = 0$,

$$\theta = -\frac{1}{2}\arccos\left(-\frac{1}{B}\right) \tag{7.15}$$

The dependence of θ on the viscosity contrast τ is shown in Fig. 7.7 for the reduced area of $A^* = 0.7$. For small τ, the inclination angle θ decreases monotonically up to a critical viscosity contrast τ^*, where $\theta = 0$. For larger viscosity contrasts $\tau > \tau^*$, there is no real solution of Eq. (7.15), i.e. there is no stationary inclination angle. For these viscosity contrasts, the vesicle is in the tumbling regime, where the inclination angle permanently rotates.

7.1.5 Swinging

The dynamical regime of swinging was discovered only very recently in 2006. It is also called the trembling [49] or vacillating breathing regime [68]. Kantsler et al. [49] were the first to find swinging vesicles in experiments. With increasing shear rate, they could observe a transition from tumbling to swinging motion. Independently of Kantsler et al. [49], Misbah [68] predicted the existence of the swinging regime theoretically. Since this theory is of lowest order of a perturbation theory in a deviation from spherical shape, the shear rate only determines the time scale, but cannot induce phase transitions. Therefore, further theories [17, 57, 73] including higher order terms have been developed which are able to predict a phase diagram depending on the shear rate, and thereby to explain the experiments of Ref. [49]

Although these theories are very complex, the physical origin of the swinging motion can be explained with simple arguments [73]. The fact that a relaxation of a vesicle to its equilibrium shape becomes less efficient with increasing $\dot{\gamma}^*$ makes the vesicle more easily deformable. Let us consider a vesicle with a reduced area A^* and a viscosity contrast τ which correspond to a tumbling vesicle, provided that the vesicle has its equilibrium shape, i.e. it has its equilibrium value of α_s. In terms of the KS theory, this means that $B(\alpha_s) < -1$ such that Eq. (7.15) does not have a real solution. Once such a vesicle is turned to inclination angles $-\frac{\pi}{2} < \theta < 0$, the forces due to the elongational flow tend to shrink the long axis of the vesicle. For sufficiently high $\dot{\gamma}^*$, the vesicle cannot recover its equilibrium shape any more such that α_s is strongly reduced. This reduced asphericity has the consequence that the vesicle is no longer in the tumbling regime, but tries to perform a tank-treading motion. In terms of the KS theory, this means that $B(\alpha_s) > -1$. Swinging can be therefore regarded as a periodic change between TT and TB.

The variety of theories on swinging [17, 57, 73] rely on different approaches. For the moderately aspherical vesicles of our computer simulations with $A^* = 0.7$, the phase diagrams calculated by these different theories show strong quantitative differences. Lebedev et al. [57] and Danker et al. [17] treated the problem in the quasi-spherical limit. However, the theory of Noguchi et al. [67, 74] does not rely on a quasi-spherical approximation. In the following, the generalized Keller-Skalak theory of Noguchi et al. [67] will be briefly summarized because it will be compared to our computer simulations later. This theory is the two-dimensional analogon to the generalized Keller-Skalak theory presented in Ref. [73].

7.1.6 Generalized Keller-Skalak theory in two dimensions

The theory of Keller and Skalak is extended such that also shape deformations are possible. Thus, the time evolution equation (7.12) of the KS theory is adopted with the difference that $B(\alpha_s)$ is not constant any more but depend on the current vesicle shape. A second differential equation for the time evolution of α_s is introduced. The total set of equations reads then

$$\begin{aligned} \dot{\theta} &= \frac{\dot{\gamma}}{2}\left(-1 + B(\alpha_s)\cos(2\theta)\right) && (7.16) \\ \dot{\alpha_s} &= -\frac{3}{4\pi\eta(\tau+1)R_A^2}\frac{\partial F}{\partial \alpha_s} + \frac{\dot{\gamma}}{\tau+1}\sin(2\theta). && (7.17) \end{aligned}$$

Here $R_A = \sqrt{A/\pi}$ denotes the radius of a sphere with same enclosed area as the vesicle, and F is the free energy of the vesicle shape, which is a function of α_s. F attains its minimum for the equilibrium vesicle shape. For the comparison with our computer simulations, Noguchi calculated the free energy F by Monte Carlo simulations with the same simulation parameters (see Sec. 7.3.1). Thus the first term on the right hand side of Eq. (7.17) causes a change of α_s towards its equilibrium value. The second term represents the change of α_s due to the external field $\dot{\gamma}$. Depending on the actual value of θ, the second term tends either to increase α_s (for $0 < \theta < \frac{\pi}{2}$) or to decrease it (for $-\frac{\pi}{2} < \theta < 0$).

The differential equations (7.16 - 7.17) are an initial value problem and can be solved numerically e.g. using the Runge-Kutta method. After an equilibration time, the solution of Eqs. (7.16 - 7.17) converges to a stationary trajectory in the $\theta - \alpha_s$ plot, independently of the initial conditions. The resulting phase diagram calculated with the same parameters as in our simulations of Sec. 7.3.1 is shown in Fig. 7.3.

Thermal fluctuations can be incorporated by adding Gaussian white noises $g_\theta(t)$ and $g_\alpha(t)$ to Eqs. (7.16) and (7.17), respectively. The noise terms have to obey the fluctuation-dissipation theorem, such that $\langle g_i(t)\rangle = 0$ and $\langle g_i(t)g_j(t')\rangle = \frac{2k_BT}{\zeta_i}\delta_{i,j}\delta(t-t')$ hold ($i,j \in \{\alpha,\theta\}$). Reasonable friction constants are the rotational friction of a circle

$$\zeta_\theta = \frac{1}{\pi}\eta P^2 \qquad \text{and} \qquad \zeta_\alpha = \frac{1}{\pi}\eta P^2(\tau+1). \tag{7.18}$$

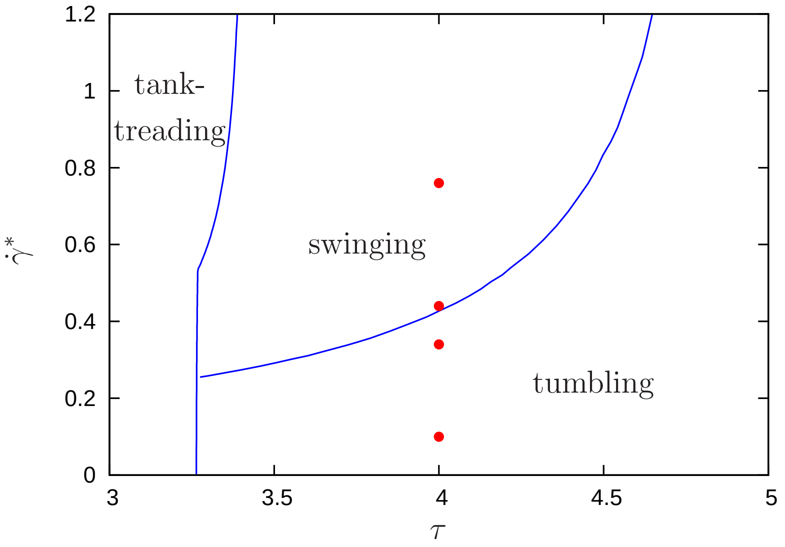

Figure 7.3: Phase diagram calculated according to generalized Keller-Skalak theory. Parameters are the same as in computer simulations. In particular, $\kappa = 50k_BT$ and $A^* = 0.7$. The red points indicate the location of the simulation in this phase diagram which are shown in Fig. 7.8.

Of course, the generalized Keller-Skalak theory which includes also thermal fluctuations does not lead to sharp transition lines in the τ-$\dot{\gamma}^*$ diagram. However, the resulting noisy trajectories in the θ-α_s plot agree nicely with our computer simulation, as it will be shown in Sec. 7.3.1.

7.2 Simulation details

Because of the lower computational costs, we study vesicle dynamics in a two-dimensional model system. Since there is a preferential rotation direction in sheared systems (see Sec. 7.1.2), angular-momentum conservation is crucial [37] as discussed in Sec. 3.2. The MPC-SR method therefore does not serve as an appropriate solvent, as it violates angular-momentum conservation. Thus we rather used the angular-momentum conserving MPC-AT+a solvent (for details see Sec. 3.2.3). This solvent also serves as a thermostat which prevents problems of heating up the system due to energy dissipation in sheared system.

In all simulations of this chapter, periodic boundary conditions are used for the x direction and no-slip wall boundary conditions for the y direction (for details, see Sec. 3.3). Linear shear with shear rate $\dot{\gamma}$ is realized by moving the upper wall with a velocity $\dot{\gamma} L_y \hat{\mathbf{x}}$, whereas the lower wall does not move.

The membrane is modeled by a closed chain of n monomers. For a monomer with index i $(1 \leq i \leq n)$, we introduce a convenient notation for the indices of its two neighboring monomers

$$\text{with} \qquad i_- = (i-1) \bmod n \qquad \text{and} \qquad i_+ = (i+1) \bmod n. \tag{7.19}$$

Thus also end monomers are treated correctly. The monomers have masses M and are connected by the same harmonic spring potential (see Eq. (4.9)) as in rod simulations. The bond potential therefore reads

$$U_{sp} = \frac{k_{sp}}{2} \sum_{i=1}^{n} (|\mathbf{R}_i| - l)^2, \tag{7.20}$$

where the bond vector $\mathbf{R}_i$ is defined by

$$\mathbf{R}_i := \mathbf{r}_{i_+} - \mathbf{r}_i. \tag{7.21}$$

Due to the topological constraint that the membrane is a closed chain, far stronger curvatures appear than in the case of semiflexible rods. The numerically very efficient bending potential (4.10) used in rod simulation cannot be used for the vesicle simulations, as for large curvatures this potential also affects the bond lengths. We rather use a bending potential U_{bend}, which is independent of bond lengths

$$U_{bend} = \kappa \sum_{i=1}^{n} \left(1 - \frac{\mathbf{R}_{i_+} \cdot \mathbf{R}_i}{|\mathbf{R}_{i_+} \| \mathbf{R}_i|} \right). \tag{7.22}$$

Since the MPC-AT+a solvent is compressible, it has to be avoided that unwanted changes of the enclosed area A occur. An area-dependent potential U_A ensures that the enclosed area deviates only very slightly from the desired area A_0

$$U_A = \frac{k_A}{2} \left(A - A_0 \right)^2. \tag{7.23}$$

The parameter k_A controls the strength of the potential, and the enclosed area A in Eq. (7.23) is a function of monomer positions

$$A = \frac{1}{2} \hat{\mathbf{z}} \cdot \sum_{i=1}^{n} \mathbf{r}_i \times \mathbf{r}_{i_+}. \tag{7.24}$$

The viscosity η_{out} is adjusted by varying the collision time h. Its values range from $h = 0.003a\sqrt{m/k_BT}$ to $h = 0.01a\sqrt{m/k_BT}$. The viscosity contrast τ is set by using different MPC masses for the inside and outside fluid. Since for the collision times $h \leq 0.01a\sqrt{m/k_BT}$ of our simulations, the total shear viscosity η of the MPC-AT+a solvent is dominated by η_{coll}, and η_{kin} has only a negligible contribution (see Eq. (3.19 - 3.21)), the viscosity ratio τ can be assumed to be equal to the ratio of the masses m_{in} and m_{out} of the inner and outer fluid particles, respectively,

$$\tau = \frac{\eta_{in}}{\eta_{out}} \approx \frac{m_{in}}{m_{out}}. \tag{7.25}$$

The viscosity contrast τ is therefore realized by using different MPC masses $m_{out} = m$ and m_{in} (with $m \leq m_{in} \leq 10m$) while all the other MPC parameters are the same for the fluid at both sides of the membrane.

It is not a trivial task to ensure that MPC particles stay on the correct side of the membrane (i.e. inside or outside of the vesicle). Before explaining the procedure how to keep particles on the correct side of the membrane, we have to clarify some terms:

- The location of the membrane is the polygon which is spanned by the monomer positions.
- For a group of n_{coll} particles, the non-rotating center-of-mass system S' is defined such that both linear and angular momenta vanish. The transformation of a velocity $\mathbf{v}_i$ in the rest frame of the simulation box S to S' is done by

  $$\mathbf{v}'_i = \mathbf{v}_i - \mathbf{v}_{cm} - \omega \times \mathbf{r}_{i,c}, \tag{7.26}$$

  where $\mathbf{v}_{cm}$ is the center of mass velocity, and

  $$\omega = \Pi^{-1} \sum_{j=1}^{n_{coll}} m_j \mathbf{r}_{j,c} \times \mathbf{v}_j \tag{7.27}$$

  is the average angular velocity of the n_{coll}-particle system (both in reference frame S). Here Π is the tensor of inertia (in two-dimensions, it is a scalar) and the $\mathbf{r}_{j,c}$ are the positions relative to the center-of-mass position $\mathbf{r}_{cm}$ of the n_{coll}-particle system.

With these definitions, it can be explained how to control that MPC particles stay on the correct side of the membrane. Actually, MPC particles are allowed to cross the membrane for small distances. The streaming and collision steps are carried out according to Eqs. (3.8) and (3.18) even if some MPC particles cross the membrane. For particles which are then located on the wrong side of the membrane, with a velocity which would bring them even further away from

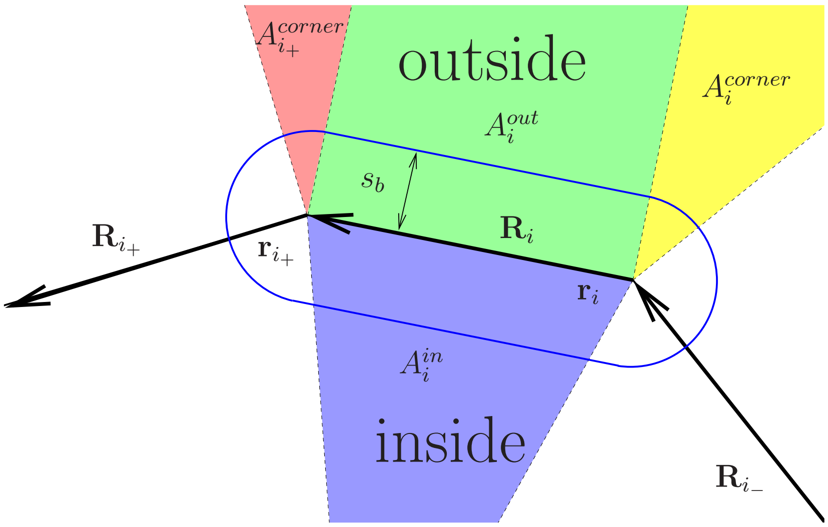

Figure 7.4: In order to make escaped MPC particles move towards the correct side of the membrane, these particles with a distance s_b to bond $\mathbf{R}_i$ have to be treated differently for each of the colored regions (for further explanations, see text).

the membrane, the velocities are modified such that they move towards the membrane in order to cross back to the correct side. In this additional velocity update, the resulting change in linear and angular momenta is transferred to membrane monomers such that both linear and angular momenta as well as energy are conserved. We therefore call this step "membrane collision". In the membrane collision, the velocities of all n_{coll} particles, which participate at the membrane collision, are inverted in their non-rotating center-of-mass system. These particles are the MPC particle which is on the wrong side and $n_{coll} - 1$ further membrane monomers. The new velocities are then

$$\mathbf{v}_{i,new} = 2\left(\mathbf{v}_{cm} + \omega \times \mathbf{r}_{i,c}\right) - \mathbf{v}_i . \tag{7.28}$$

The selection of the $n_{coll} - 1$ membrane monomers, which participate in a membrane collision, is demonstrated in Fig. 7.4. First the membrane bond which has the smallest distance to the MPC particle has to be identified. The definition of the distance s_b between a MPC particle and a bond is shown in Fig. 7.4. All points on the blue line have the same distance s_b to the bond i with bond vector $\mathbf{R}_i$. Different cases have to be distinguished, depending on the location of the

MPC particle relative to its closest bond.

- MPC particles which are on the wrong side of the membrane and are located either in the region A_i^{out} (green area in Fig. 7.4) or in the region A_i^{in} (blue area) uniquely belong to bond $\mathbf{R}_i$. For such a MPC particle, the velocity component $\mathbf{v}'_{j,\perp}$ perpendicular to bond $\mathbf{R}_i$ has to be calculated in the non-rotating three body system consisting of the MPC particle itself and the two monomers i and i_+ which span the bond i
$$\mathbf{v}'_{j,\perp} = \left(\hat{\mathbf{I}} - \frac{\mathbf{R}_i \otimes \mathbf{R}_i}{R_i^2} \right) \mathbf{v}'_j. \tag{7.29}$$
If $\mathbf{v}'_{j,\perp}$ and $\mathbf{r}_{j,\perp} = \left(\hat{\mathbf{I}} - \mathbf{R}_i \otimes \mathbf{R}_i / R_i^2 \right) \mathbf{r}_j$ point in the same direction (i.e. $\mathbf{v}'_{j,\perp} \cdot \mathbf{r}_{j,\perp} > 0$), a three-body membrane collision is performed according to Eq. (7.28) with the MPC particle and the two monomers i and i_+.
- MPC particles which are located on the wrong side of the membrane and either in the region A_i^{corner} (yellow area in Fig. 7.4) or in the region A_{i+}^{corner} (red area) have the same distances to bond i as to bond i_- or i_+, respectively. For such a MPC particle, it is checked if its velocity in the non-rotating center-of-mass system points towards the monomer which defines the corner (monomer i if the MPC particle is in A_i^{corner}). If not, a two-body membrane collision (see Eq. (7.28)) is performed with the MPC particle and this monomer i.

In order to prevent the membrane vesicles from crossing walls, a purely repulsive Lennard-Jones potential $U_{Wall}(y)$ is applied which only depends on the y position of monomers,

$$U_{Wall}(y) = \begin{cases} 4\varepsilon \left[\left(\frac{\sigma}{y} \right)^{12} - \left(\frac{\sigma}{y} \right)^{6} \right] + \varepsilon, & 0 \leq y \leq \sqrt[6]{2}\sigma \\ 4\varepsilon \left[\left(\frac{\sigma}{L_y - y} \right)^{12} - \left(\frac{\sigma}{L_y - y} \right)^{6} \right] + \varepsilon, & L_y - \sqrt[6]{2}\sigma \leq y \leq L_y \\ 0, & \text{otherwise} \end{cases} \tag{7.30}$$

In Chap. 7.3.2, where hydrodynamic lift forces on vesicles under shear flow closed to a wall will be determined, also a gravitational body force $\mathbf{f}_G = -\hat{\mathbf{y}} g \Delta\varrho$ will be needed which acts on the internal fluid of the vesicle. Here g denotes the strength of the gravitational field and $\Delta\varrho$ is the mass density difference between the inner and the outer fluids. This gravitational body force is thereby an (inverse) buoyancy force. It has to be mentioned that $\Delta\varrho$ refers to “heavy” masses which

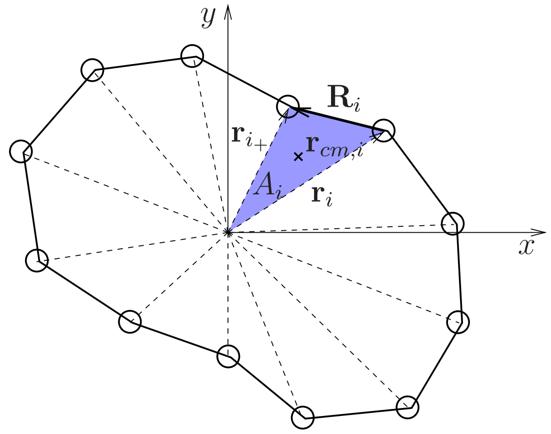

Figure 7.5: Decomposition of the enclosed area into triangles. The blue triangle is defined by two monomers with positions $\mathbf{r}_i$ and $\mathbf{r}_{i_+}$ and has size A_i with center-of-mass position $\mathbf{r}_{cm,i}$.

only play a role in a gravitational field and must not be identified with the "inert" mass densities $m_{in}\varrho$ and $m_{out}\varrho$ which are crucial in the MPC-AT+a collision step. One way of realizing such a body force is to apply gravitational forces to the inner MPC particles. However, the compressibility of the MPC-AT+a solvent would lead to an unwanted density gradient inside of the vesicle. Instead, we use that the total gravitational force

$$\mathbf{F}_G = \int_A \mathbf{f}_G dA \tag{7.31}$$

of the whole inside fluid which can be described by the potential

$$U_G = g \int_A y \Delta\varrho dA = -\mathbf{F}_G \cdot \mathbf{r}_{cm} \tag{7.32}$$

where $\mathbf{r}_{cm}$ is the center-of-mass position of the enclosed area. In our simulations, the enclosed area is bordered by a polygon which is spanned by the monomer positions $\mathbf{r}_i$. The enclosed area A can be regarded to be composed of triangles as shown in Fig. 7.5. The integral in Eq. (7.32) can be then replaced by a sum of the contributions $U_{G,i}$ of each of those triangles

$$U_G = \sum_i U_{G,i}. \tag{7.33}$$

The integral $U_{G,i}$ over such a triangle can be calculated analytically which is

$$U_{G,i} = \Delta\varrho \underbrace{\frac{1}{2}\left(\mathbf{r}_i \times \mathbf{r}_{i_+}\right) \cdot \hat{\mathbf{z}}}_{= A_i} g \underbrace{\frac{1}{3}\left(y_i + y_{i_+}\right)}_{= y_{cm,i}} = -\mathbf{F}_{G,i} \cdot \mathbf{r}_{cm,i}. \tag{7.34}$$

Here A_i is the area of triangle i, $\mathbf{F}_{G,i}$ is its gravitational force and $\mathbf{r}_{cm,i}$ its center-of-mass position ($y_{cm,i}$ is its y component). The origin does not have to be inside the vesicle as it is the case in Fig. 7.5. Since in expression (7.34), $U_{G,i}$ can also be negative (the cross-product in A_i may have both signs), summands in Eq. (7.33) partially cancel each other. The only non-vanishing contribution to the gravitational potential is that of the enclosed area.

For a constant mass density, the total gravitational force acting on the whole inner fluid would depend on its area A. It has turned out that this leads to artifacts even with the use of the area controlling potential U_A, Eq. (7.23). Therefore, an area-dependent mass density $\Delta\varrho = \Delta\varrho^0 A_0/A$ is used. Here A_0 and $\Delta\varrho^0$ are the equilibrium values for the enclosed fluid area and its mass density, respectively. The magnitude of the total gravitational force is then $F_G = \Delta\varrho^0 A_0 g = \Delta\varrho A g$. The gravitational potential finally reads

$$\begin{aligned} U_G &= \frac{\Delta\varrho^0 A_0 g}{6A} \sum_i \left(y_i + y_{i_+}\right)\left(\mathbf{r}_i \times \mathbf{r}_{i_+}\right) \cdot \hat{\mathbf{z}} && (7.35) \\ &= \frac{F_G}{6A} \sum_i \left(y_i + y_{i_+}\right)\left(\mathbf{r}_i \times \mathbf{r}_{i_+}\right) \cdot \hat{\mathbf{z}}. && (7.36) \end{aligned}$$

As long as not specified explicitly, the parameters used in vesicle simulations are $n = 50$, $l = a = \sqrt[6]{2}\sigma$, $M = 10m$ and $\varepsilon = 10k_BT$ and $\kappa = 50k_BT$. For the reduced area, we require that its value deviates less than one percent from its desired value of $A^* = 0.7$. Since A^* is a function of the perimeter P and the enclosed area A (see Eq. (7.1)), the parameters k and k_A for the potentials U_{sp} and U_A, respectively, have to be sufficiently high. We chose $k_A = 80k_BT/a^4$ and $k = 10^4 k_BT/a^2$. The linear sizes of the simulation box are $L_x = L_y = 80$. Gravitational forces F_G are only applied in simulations of Sec. 7.3.2, where different values in the range $k_BT/a \leq F_G \leq 50k_BT/a$ are used.

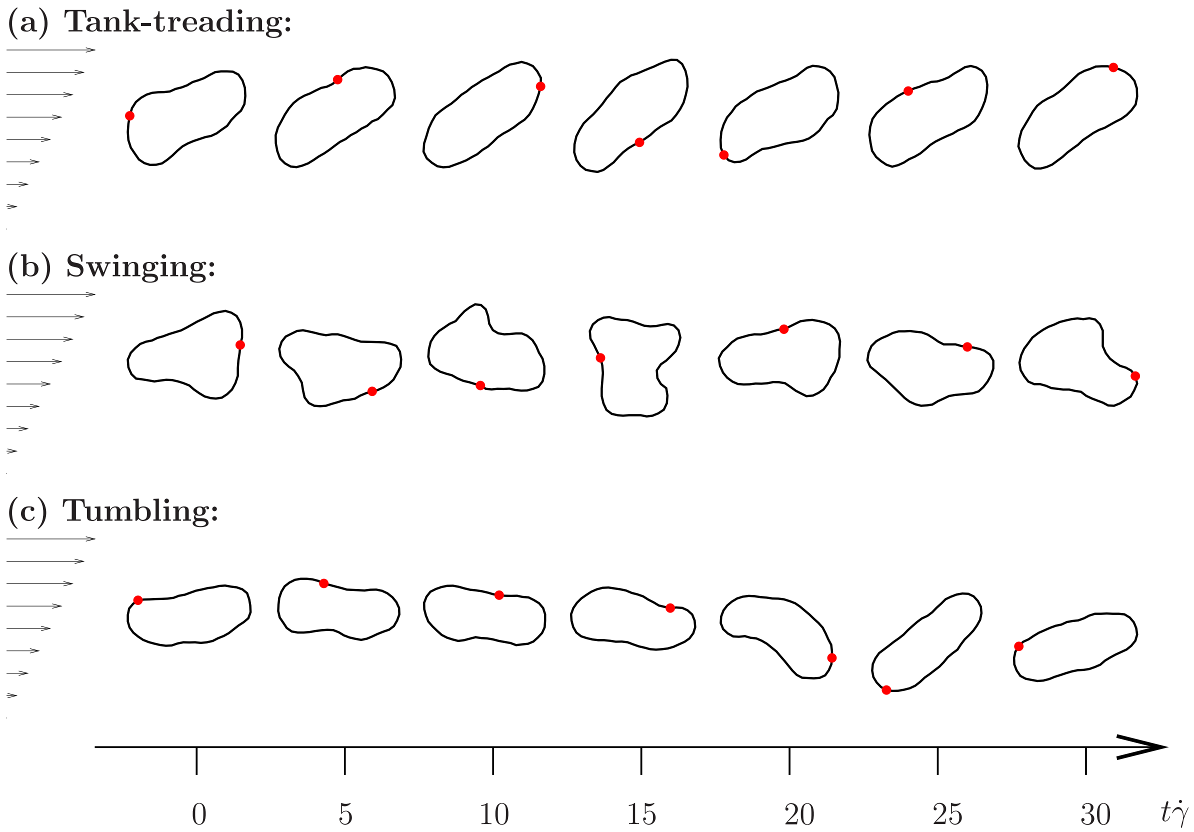

Figure 7.6: For each of the dynamical regimes, a sequences of vesicle snapshots is shown. The red point marks a fixed membrane element such that it is possible to follow the membrane motion. Parameters which are common for all systems are $\kappa = 50 k_B T$ and $A^* = 0.7$. Further parameters are: (a) $\eta = 120\sqrt{k_B T m}/a$, $\tau = 4$, $\dot{\gamma} = 0.005\sqrt{m/k_B T}/a \;\Rightarrow\; \dot{\gamma}^* = 0.1$ (b) $\eta = 120\sqrt{k_B T m}/a$, $\tau = 4$, $\dot{\gamma} = 0.0333\sqrt{m/k_B T}/a \;\Rightarrow\; \dot{\gamma}^* = 0.76$ (c) $\eta = 36\sqrt{k_B T m}/a$, $\tau = 10$, $\dot{\gamma} = 0.01\sqrt{m/k_B T}/a \;\Rightarrow\; \dot{\gamma}^* = 0.07$

7.3 Results

7.3.1 Dynamical regimes of vesicles in shear flow

Computer simulations of the three dynamical regimes (TT, TB, SW) are illustrated by a sequence of snapshots in Fig. 7.6.

In simulations, different reduced shear rates $\dot{\gamma}^*$ can be achieved, according to Eq. (7.9), by varying $\dot{\gamma}$, η, R or κ. However, the use of different R or κ would

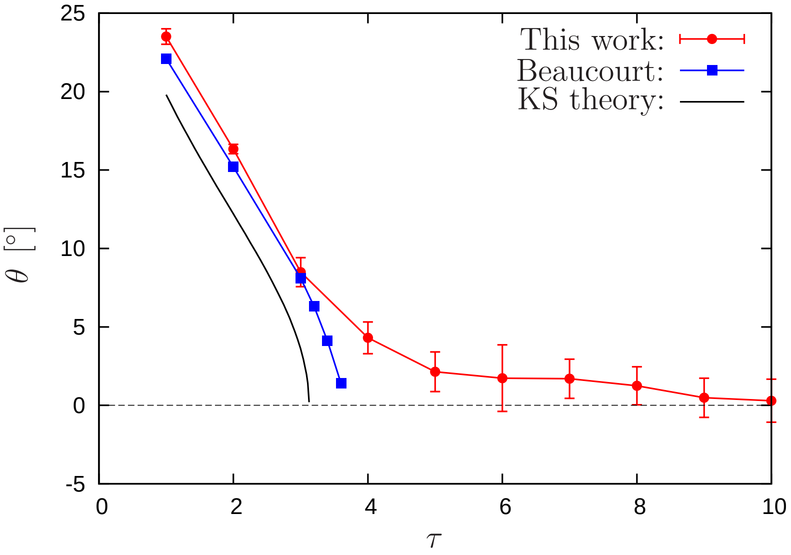

Figure 7.7: Inclination angle θ vs. viscosity contrast τ for simulations with $\dot{\gamma}^* = 0.068$. For comparison also the results of the boundary integral calculation of Beaucort et al. [9] as well as the curve according to Keller and Skalak [50] (see Eq. (7.15)) are shown.

make it difficult to compare results for different $\dot{\gamma}^*$. Hence $\dot{\gamma}^*$ is adjusted by $\dot{\gamma}$ and η only. We make sure that the Reynold number does not become too large; it does not exceed a value of $Re = 0.17$. The outer viscosity η itself can be changed to the desired value by changing the MPC collision time h.

The simulation model was tested by comparing simulation results with existing Oseen tensor calculations of Beaucort et al. [9]. For this purpose, a sequence of simulations was performed without a gravitational force and different viscosity contrasts ranging from $\tau = 1$ to 10. The shear rate was taken to be $\dot{\gamma} = 0.01\sqrt{k_BT/ma^2}$ such that $\dot{\gamma}^* = 0.068$, $Pe = 274$ and $Re = 0.17$. For this reduced shear rate, no swinging is expected (see Fig. 7.3). In Fig. 7.7, the resulting average inclination angles θ are plotted as a function of the viscosity contrast τ. Our computer simulations well reproduce the results of Beaucort et al. [9]. Small deviations closed to the TT-TB transition at $\tau \approx 4$ arise from thermal fluctuations of our simulations, whereas Beaucort et al. [9] study the zero-temperature limit. Moreover, thermal fluctuations lead to a continuous rather than to a sharp TT-TB transition. Thus, there are a few tumbling events even for the viscosity contrast $\tau = 3$, and also simulations with $\tau > \tau^* \approx 4$

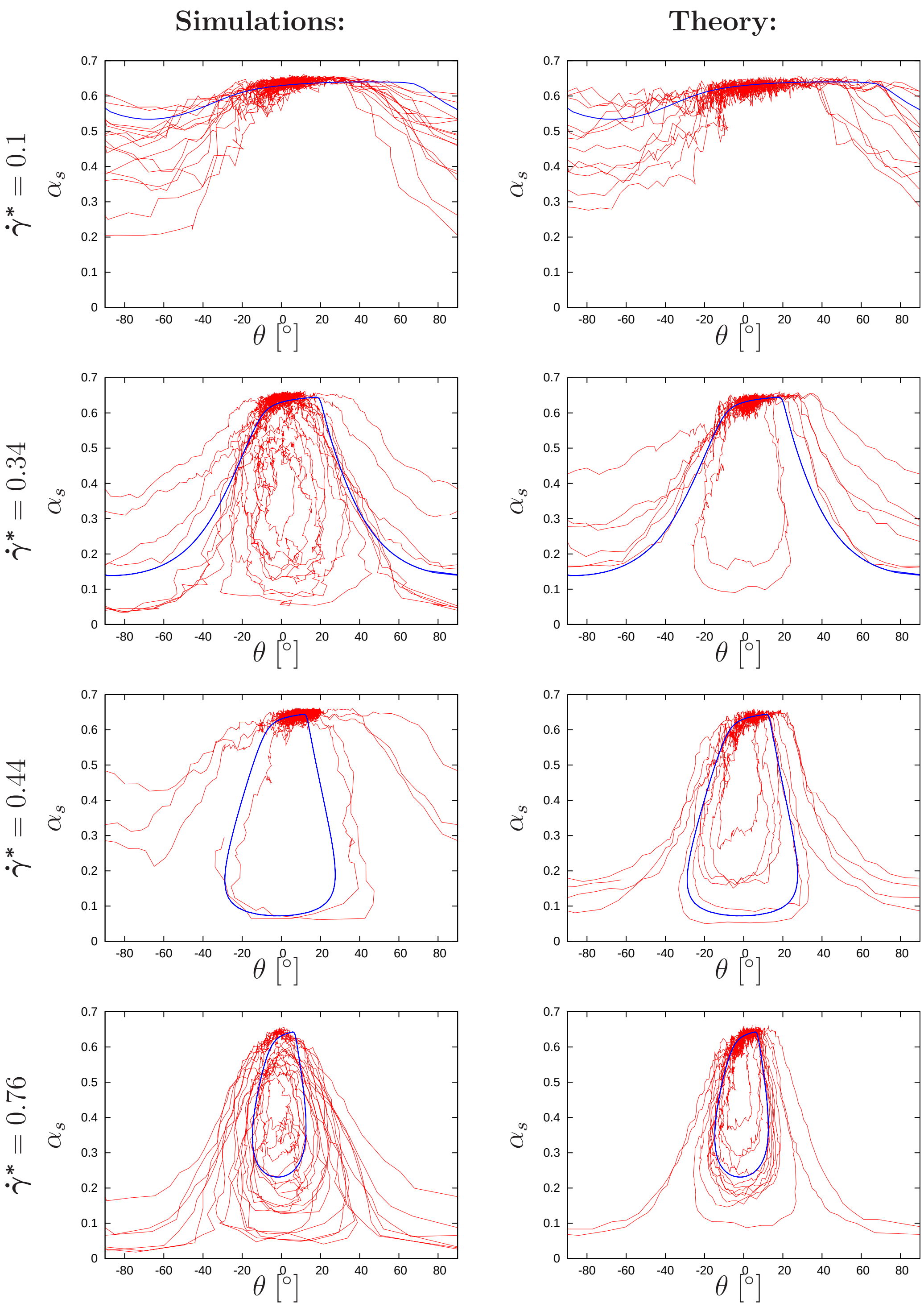

Figure 7.8: Trajectories in the θ-α_s plane obtained from simulations (left) and the generalized Keller-Skalak theory with thermal noise (right) are lines in red. In all plots, also the corresponding theoretical trajectory according the generalized Keller-Skalak theory without thermal noise is shown in blue.

exhibit some tank-treading events.

Fig. 7.7 also shows that also the KS theory [50] provides a very good prediction for the τ dependence of θ and the TT-TB transition.

Our simulations also show that the existence of a tumbling regime depends very sensitively on the Reynolds number Re. For $Re \gtrsim 1$, no tumbling motion was observed.

To investigate the TB-SW transition, the viscosity contrast was kept fixed at $\tau = 4$, and four different reduced shear rates $\dot{\gamma}^* = 0.1, 0.34, 0.44$ and 0.76 were studied. According to the generalized Keller Skalak theory [67] the reduced shear rates of $\dot{\gamma}^* = 0.1$ and 0.34 should belong to the tumbling regime, whereas for the $\dot{\gamma}^* = 0.44$ and 0.76, a swinging motion is expected (see Fig. 7.3). The resulting trajectories in the θ-α_s plane are shown in Fig. 7.8 for all the four different reduced shear rates $\dot{\gamma}^*$ together with the theoretical trajectories of the generalized KS theory without noise. The corresponding trajectories calculated by the generalized KS theory with thermal noise are also shown in Fig. 7.8. In this representation, closed cycles indicate swinging events, whereas trajectories exceeding the values of $\theta = \pm\pi/2$ are tumbling events. Obviously, thermal noise has an enormous impact on vesicle dynamics. In particular, at inclination angles slightly below $\theta = 0$, small thermal fluctuations can be decisive for the vesicle to perform a tumbling or a swinging cycle. Despite the strong fluctuations, the qualitative picture of simulated and noisy theoretical trajectories is in very good agreement for each of the four reduced shear rates. This confirms that the generalized KS theory of Noguchi is indeed a very good description of vesicle dynamics.

7.3.2 Lift force

Vesicles under shear close to a wall experience a hydrodynamic lift force F_L which repels them from the wall [1, 14, 75, 76, 90]. This hydrodynamic force is a pressure force which is of purely viscous nature – in contrast to e.g. aerodynamic forces acting on wings of a plane which are caused by inertia.

The hydrodynamic lift force plays an important role in the circulatory systems of vertebrates. Since the lift force pushes red blood cells (erythrocytes) to the center of a blood vessel, where the flow velocities is largest, it increases the efficiency of material transport. However, the mission of white blood cells (leukocytes) is

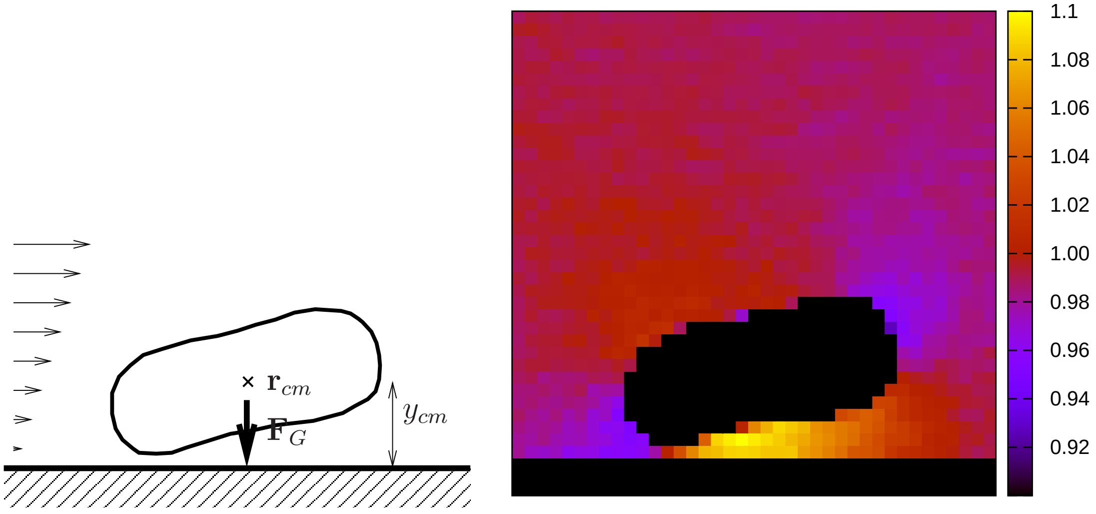

(a) (b)

Figure 7.9: (a) Contour of the steady shape of a tank-treading vesicle with viscosity contrast $\tau = 3$ under shear closed to a wall and (b) the resulting pressure field. The color code is expressed in units of $\varrho k_B T$. The hydrodynamic lift force is balanced by a external gravitational force $F_G = 14 k_B T/a$ at this distance from the wall which is $y_{cm} = 7.96a$ in this case.

to move along the vessel walls in order to find defects in the vascular endothelium [45]. For this purpose, special ligands are located at the outside of white blood cells which are able to bind to receptors on the vessel wall in order to resist the hydrodynamic lift force.

In our simulations the dependence of the lift force $F_L(y_{cm})$ on the wall distance y_{cm} (see Fig. 7.9.a) is determinded by applying a gravitational force F_G to the vesicle under steady shear as described in Sec. 7.2. The vesicle is moved towards or away from the wall until gravitational F_G and lift forces $F_L(y_{cm})$ balance each other. For this steady wall distance y_{cm}, the gravitational force can be identified by the lift force $F_L(y_{cm})$. Without F_G, there would not be any steady-state with wall distance y_{cm} in the presence of one wall.

Fig. 7.9.b shows the pressure field in the outer fluid for the steady-state configuration of a tank-treading vesicle. The hydrodynamic lift force is the integral of the pressure forces over the membrane contour. A higher pressure in the gap between the vesicle and the wall is responsible for the lift force. In this pressure-

field plot, it can be nicely seen that there is a lower pressure at the caps of the vesicle membrane. This pressure difference is the origin of the vesicle elongation. Several simulations were performed for the viscosity contrasts $\tau = 1, 2, 3, 4$ and 10 with gravitational forces ranging from $F_G = 1 k_B T/a$ to $50 k_B T/a$. The resulting wall-distance dependence of the hydrodynamic lift force is shown in Fig. 7.10.a in a double-logarithmic representation. For a fixed wall distance y_{cm}, the resulting lift forces decrease with increasing viscosity ratio τ.

Lift forces of vesicles with $\tau \leq 4$ obey a power-law dependence

$$F_L \propto y_{cm}^{\zeta} \tag{7.37}$$

on the wall distances y_{cm} for lift forces $F_L \leq 20 k_B T/a$. In Fig. 7.10.a, also a line with the power law dependence $1/y_{cm}^2$ is shown, from which we conclude the characteristic exponent

$$\zeta \approx -2. \tag{7.38}$$

For these distances, the vesicle is not in direct contact with the wall. At applied gravitational forces larger than $20 k_B T/a$, the vesicle comes in touch with the wall. However, the center-of-mass wall distance y_{cm} can be lowered even further by deforming the vesicle. The $1/y_{cm}^2$ dependence does not apply in this regime. Finally, the constraints of fixed enclosed area A and fixed perimeter P keep the center of mass wall distance larger than $y_{cm} \gtrsim 5a$. In Fig. 7.11, the amplitude $F_L y_{cm}^2$ of the lift force is shown as a function of the viscosity contrast τ. The amplitudes are fits to the curves in Fig. 7.10.a where those y_{cm} are considered, for which the vesicle is not in direct contact with the wall. A strong decrease of the amplitude $F_L y_{cm}^2$ can be seen with increasing viscosity contrast τ.

A direct comparison with theoretical predictions is not possible, since lift forces of two-dimensional vesicles bound to walls by a short-ranged attractive potential were investigated [14, 87].

For vesicles in three dimensions which are separated from the wall, the experimental work of Abkarian et al. [1] exhibits a $1/y_{cm}$ dependence of the lift force – independent of the reduced volume V^* (the three-dimensional analogon to the reduced area A^*). Sukumaran et al. [90] performed boundary integral calculations of three-dimensional heavy tank-treading vesicles and determined the lift-forces dependence on y_{cm} in the same way as we do. Besides the different dimensionality, their reduced volume $V^* \approx 0.95$ is far closer to the spherical limit. However, they find a $1/y_{cm}^2$ dependence, which is in accordance with our findings.

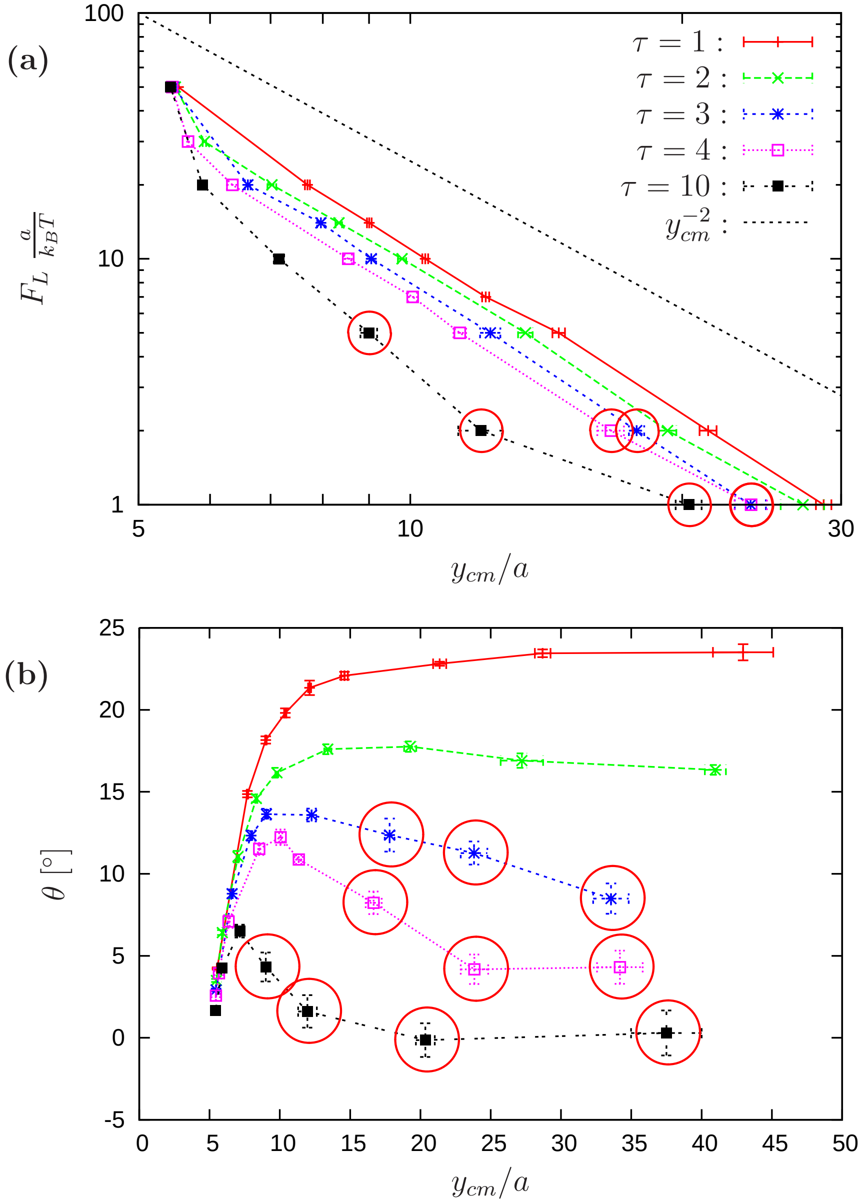

Figure 7.10: (a) lift forces and (b) the resulting average inclination angle in dependence of the average distance y_{cm} between wall and center of mass of the vesicle for $\dot{\gamma}^* = 0.068$ and $Pe = 274$. The legend in (a) applies to both plots. Points marked by red circles refer to tumbling vesicles. For comparison, also a line with a y_{cm}^{-2} dependence is plotted in (a).

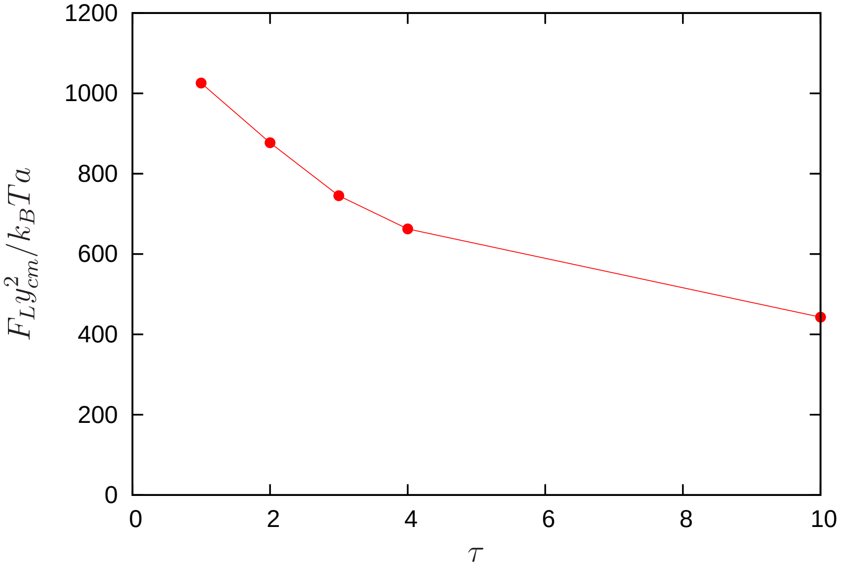

Figure 7.11: Amplitude of the lift force F_L as a function of the viscosity contrast τ. The data points are fits to the curves in Fig. 7.10.a for which vesicles are not in direct contact with the wall.

The theoretical studies of Olla [75, 76] on lift forces acting on tank-treading ellipsoids in three dimensions are valid for arbitrary combinations of ellipsoid half axes a_1, a_2, a_3 and holds thereby also for very aspherical vesicles. It also predicts a $1/y_{cm}^2$ dependence for large wall distances $y_{cm} \gg a_1, a_2, a_3$ which is indeed similar to our computer-simulation results. However, it is not possible to perform a two-dimensional limit of the theory of Ref. [75, 76], as we did for the KS theory by making one half axis a_3 infinitesimally large. This cylindrical geometry would violate the assumption $y_{cm} \gg a_1, a_2, a_3$ employed in the theory. Fig. 7.10,a also shows that tumbling is suppressed above a certain gravitational force. In order to perform a tumbling motion, the center of mass distance y_{cm} has to be larger than the long vesicle axis a_1. However, for too high gravitational forces, the center of mass distance y_{cm} becomes smaller than a_1, such that even vesicles with high viscosity contrasts do not tumble. Even if y_{cm} is slightly larger than a_1, the vesicle cap has to come so close to the wall that the resulting pressure forces may prevent the inclination angle to overcome a certain value. In Fig. 7.10,b, the inclination angle θ is plotted vs. wall distance y_{cm} for the same simulations as in Fig. 7.10,a. The right-most data points correspond to

$F_G = 0$, such that they cannot be shown in the log-log plot Fig. 7.10.a. Without any gravitational forces, the lift force caused by the upper wall at $y = 80a$ compensates the lift force of the lower wall for $y_{cm} = 40a$. Since the lift forces are very small at $y_{cm} = 40a$, strong fluctuations are observed in the wall distances. As long as a vesicle tank-treads, its inclination angle θ increases with wall distance y_{cm}. Even if the vesicle does not touch the wall, the pressure at the lowest part of the membrane is highest (see Fig. 7.9,b) such that it causes a torque which lowers θ. For very small wall distances, the vesicle comes into direct contact with the wall, where the repulsive wall potential causes a torque, which decreases θ, until the vesicle is finally completely parallel to the wall with $\theta = 0$. Vesicles with $\tau \geq 3$ start to tumble at sufficiently large wall distances. Since the vesicles with viscosity ratios $\tau = 3$ and $\tau = 4$ still tank-tread most of the time and only occasionally perform a tumbling event, their inclination angles do not completely vanish, whereas for $\tau = 10$ and $F_G \leq 1$, the average inclination angle vanishes.

For the near future, we plan to perform boundary integral calculations, where the lift force is calculated for vesicle geometries and tank-treading velocities obtained from our computer simulations.

7.4 Summary and Conclusion

We have studied the dynamics of vesicles in shear flow in a two-dimensional model system. These systems show a variety of interesting dynamical phenomena. In particular, the effect of a viscosity ratio, i.e. the ratio between the inner and the outer viscosity of the vesicle, on vesicle dynamics has been investigated. Depending on the viscosity ratio vesicles can either "tumble", "swing" or show "tank-treading". In the tumbling regime, the vesicle orientation permanently rotates, in the swinging regime the vesicle exhibits temporally periodical changes in shape and orientation and in the tank-treading regime both shape and orientation are constant in time, whereas the membrane rotates around the enclosed volume. For the first time, a transition from tank-treading to swinging with increasing viscosity contrast could be shown in computer simulations. Our simulations are in good agreement with a phenomenological theoretical description.

Close to walls, tumbling is strongly suppressed. Furthermore, the vesicle is repelled from the wall. The origin of this repulsion is the hydrodynamical lift force. We could show that the lift force on vesicles decays inversely proportional to the squared wall distance. With increasing viscosity, the hydrodynamic lift force becomes weaker, as the vesicle becomes less deformable.

Our observations are relevant for phenomena in biology, because vesicles can be considered as model system for blood cells in blood flow. The effect of a viscosity contrast is of particular interest, since the cytosol of blood cells contains many macromolecules and filaments which leads to a higher inner viscosity (compare Chap. 5). The hydrodynamic lift force plays an important role in the circulatory systems of vertebrates. Since the lift force pushes red blood cells (erythrocytes) to the center of a blood vessel, where the flow velocities is largest, it increases the efficiency of material transport. However, the mission of white blood cells (leukocytes) is to move along the vessel walls in order to find defects in the vascular endothelium. For this purpose, special ligands are located at the outside of white blood cells which are able to bind to receptors on the vessel wall in order to resist the hydrodynamic lift force.

8 Summary and conclusion

We have investigated the dynamics of dense suspensions of rod-like colloids and of single vesicles by means of computer simulations, with special attention on the influence of hydrodynamic interactions.

As soft-matter systems, these apparently very distinct systems have in common that they are characterized by hydrodynamic interactions, thermal fluctuations and a large separations of length and time scales between the solvent and the solute. Therefore an appropriate simulation model was chosen, which takes into account these essential characteristics. Colloids and vesicles were modelled in a coarse-grained fashion by a group of connected point particles, and their dynamics is treated by Molecular Dynamics. For the solvent, the Multi-Particle Collision Dynamics (MPC) algorithm was used, a mesoscale particle-based simulation technique which provides the thermodynamic and hydrodynamic properties which are essential for soft matter dynamics. Optionally, hydrodynamic interactions can be switched off. Thus the effect of hydrodynamics can be easily elucidated.

Rod-like colloids can form different thermodynamically stable phases. Their phase behavior depends mainly on volume fraction, but also temperature, flexibility, chirality and polydispersity are crucial. We focused on dense suspensions of monodisperse, semiflexible rods in the isotropic and nematic phase. Such systems are of high interest, as they can be regarded as model systems for biological phenomena in cells. The cytoplasm, the interior of a biological cell, typically contains a dense network of filaments immersed into an aqueous environment. These filaments are often oriented isotropically, but under certain circumstances they are directed. For the life of a cell it is essential that material can be transported by diffusion even in very dense networks.

We calculated self-diffusion constants of rod-like colloids for a broad range of volume fractions. We could find that solvent mediated hydrodynamic interactions lead to an increase in diffusion for all considered volume fractions. Moreover, simulations have shown that the larger the hydrodynamic diameter the more strongly diffusion is diminished with increasing concentration. In nematic systems, diffusion becomes anisotropic, which implies different diffusion constants for motion into parallel and perpendicular directions. The diffusion anisotropy was determined in dependence of concentration and rod aspect ratios. We could show that the diffusion anisotropy increases with the rod aspect ratio. Our results are in agreement with experiments of rod-like *fd* viruses.

In rod suspensions, not only hydrodynamics influences rod dynamics, but there is also the inverse effect that rods influence hydrodynamics. The rod network screens the otherwise long-ranged hydrodynamic interactions. Hydrodynamic interactions in soft-matter systems can be well described by the hydrodynamic mobility tensor which relates forces acting on a particular site of the system to velocities at different locations. We presented a procedure which allows us to calculate the hydrodynamic mobility tensor from equilibrium fluctuations of shear waves in simulations. The hydrodynamic mobility tensor contains important information about hydrodynamics, including hydrodynamic screening lengths. We have shown that the screening lengths is of the order of typical distances between neighboring rods. Also the solvent viscosity and the effective viscosity of the whole suspension could be identified from the hydrodynamic mobility tensor. Since such a direct determination of screening lengths is not possible in experiments, our method is highly advantageous for the understanding of hydrodynamics in dense systems. Hydrodynamic screening has consequences for dynamical phenomena in rod systems. In particular, diffusion of small particles immersed in rods depend very sensitively on hydrodynamic screening lengths.

In experiments, hydrodynamic screening lengths can be measured only indirectly due to their effect on other dynamical phenomena. Such indirect measurements have been done by our cooperation partners of the group Dhont. They developed a theory for tracer-sphere diffusion in rods, which is based on hydrodynamic screening. Hydrodynamic screening lengths could be obtained by fitting measured tracer-diffusion constants. Such indirect measurements are not very accurate and rely on the validity of the theory. In simulations, we calculated diffusion constants of small tracer spheres in dense rod suspensions. These diffusion constants agree well with the theory if screening lengths are used which have been calculated in Chap. 5. Thereby the validity of our screening lengths evaluation as well as the theory of Ref. [47] are nicely confirmed.

Far more complex soft matter systems are vesicles which are small fluid droplets enclosed by a membrane with an internal dynamics. We focus on phenomena arising in vesicles under shear in a two-dimensional model system. We consider vesicles with a viscosity contrast, i.e. the fluid inside the vesicle has a higher viscosity than the outer one. This situation is also interesting for biology, as blood cells typically contain a high viscous cytosol. Depending on the strength of the shear flow, the viscosity ratio and the ability of the vesicle to restore its equilibrium shape from perturbations, such vesicles can be found in different dynamical regimes – the tank-treading, tumbling and swinging regimes. In the tank-treading regime, which is observed for low viscosity contrasts, the vesicle has a fixed shape and orientation, but the membrane rotates around the vesicle. For higher viscosity ratios, the vesicle is more rigid and its orientation permanently rotates. In strong shear flows, deformations of the vesicles can be so strong that it is not able to relax to its equilibrium shape. In this case, also the dynamic regime of swinging can be observed. In addition to periodic changes in orientations like in the tumbling regime, also periodic shape deformations occur in the swinging regime. We could see the transition to a swinging regime with increasing viscosity contrast for the first time by computer simulations. Our simulations show a nice agreement with a corresponding phenomenological theory.

Furthermore, the dynamics of vesicles with different viscosity contrasts close to a wall has been investigated. We have shown that tumbling is strongly suppressed in the vicinity of a wall. Moreover, the hydrodynamical lift force has been studied, which is of purely viscous origin and repells vesicles from a wall. We could show that the lift force on vesicles decays inversely proportional to the squared wall distance. With increasing viscosity, the hydrodynamic lift force becomes weaker.

The lift force has also consequences for biology. In circulatory systems of vertebrates vesicle-like red blood cells are pushed by the lift force to the center of a blood vessel, where the flow velocities is larger. Thus it is prevented that red blood cells stick to vessel walls.

Appendix A

Calculation of $\widetilde{T}(k)$ for simple MPC-SR fluids under the assumption of molecular chaos

The hydrodynamic mobility tensor $\widetilde{\mathbf{T}}(\mathbf{k})$ in Fourier space was calculated for simple MPC-SR fluids in Sec. 5.3. Results of the simulations are shown in Fig. 5.3. For small wave numbers $k \lesssim k_c = 2\pi/\lambda_c$, where λ_c is the hydrodynamic cutoff, the trace $\tilde{T}(k)$ of the hydrodynamic mobility tensor nicely follows the $1/k^2$ dependence of the Stokes equation. This fact justifies that the MPC-SR method is a good simulation technique for hydrodynamic phenomena at not too small length scales. However, for larger wave numbers, $\tilde{T}(k)$ undergoes a crossover to a plateau, where $\tilde{T}(k)$ reaches a finite value which is independend of k. The crossover happens close to the cutoff wave number $k_c = 2\pi/\lambda_c$.

In this appendix, we calculate the plateau value of $\tilde{T}(k)$. Since in the plateau regime, inter-particle (i.e. hydrodynamic) correlations can be neglected, solvent dynamics is governed by molecular chaos,

$$\langle \mathbf{v}_i(t) \otimes \mathbf{v}_j(t) \rangle = \hat{\mathbf{I}}\, \delta_{i,j} \frac{k_B T}{m}. \tag{A.1}$$

Here $\mathbf{v}_i(t)$ is the velocity of particle i at time t, and m is the MPC particle mass. In order to distinguish between the different expressions of the different regimes, the mobility tensor under molecular chaos will be denoted by $\tilde{T}_{mc}(k)$ in the following. With the molecular-chaos assumption (A.1) and the collision rule of the MPC-SR method (3.9), an analytic expression for

$$\widetilde{\mathbf{T}}_{mc}(\mathbf{k}) = \frac{1}{k_B T} \int_0^\infty dt\, \langle \tilde{\mathbf{v}}^*(\mathbf{k}, 0) \otimes \tilde{\mathbf{v}}(\mathbf{k}, t) \rangle \tag{A.2}$$

can be calculated analytically. First, the integrand $\langle \tilde{\mathbf{v}}^*(\mathbf{k},0) \otimes \tilde{\mathbf{v}}(\mathbf{k},t)\rangle$ ise calculated for molecular chaos,

$$\langle \tilde{\mathbf{v}}^*(\mathbf{k},0) \otimes \tilde{\mathbf{v}}(\mathbf{k},t)\rangle = \left\langle \left[\mathbf{P}_\mathbf{k} \frac{1}{N} \sum_{i=1}^{N} \mathbf{v}_i(0) e^{i\mathbf{k}\cdot\mathbf{r}_i(0)} \right] \otimes \left[\mathbf{P}_\mathbf{k} \frac{1}{N} \sum_{j=1}^{N} \mathbf{v}_j(t) e^{-i\mathbf{k}\cdot\mathbf{r}_j(t)} \right] \right\rangle, \tag{A.3}$$

where Eq. (5.20) for $\tilde{\mathbf{v}}(\mathbf{k},t)$, and the abbreviation

$$\mathbf{P}_\mathbf{k} := \hat{\mathbf{I}} \, - \hat{\mathbf{k}} \otimes \hat{\mathbf{k}}. \tag{A.4}$$

for the projection operator has been used. With the symmetry relation

$$\mathbf{P}_\mathbf{k} = \mathbf{P}_\mathbf{k}^T \tag{A.5}$$

and

$$(\mathbf{P}_\mathbf{k}\mathbf{a}) \otimes (\mathbf{P}_\mathbf{k}\mathbf{b}) = \mathbf{P}_\mathbf{k}(\mathbf{a} \otimes \mathbf{b})\mathbf{P}_\mathbf{k}^T = \mathbf{P}_\mathbf{k}(\mathbf{a} \otimes \mathbf{b})\mathbf{P}_\mathbf{k} \tag{A.6}$$

Eq. (A.3) can be written as

$$\langle \tilde{\mathbf{v}}^*(\mathbf{k},0) \otimes \tilde{\mathbf{v}}(\mathbf{k},t)\rangle = \frac{1}{N^2} \mathbf{P}_\mathbf{k} \sum_{i,j} \left\langle \mathbf{v}_i(0) \otimes \mathbf{v}_j(t) e^{-i\mathbf{k}\cdot(\mathbf{r}_j(t)-\mathbf{r}_i(0))} \right\rangle \mathbf{P}_\mathbf{k}. \tag{A.7}$$

Since velocities and positions are generally uncorrelated ($\langle \mathbf{v}_i(0) \otimes \mathbf{r}_j(t)\rangle = 0$), and since for molecular chaos velocities are only correlated with velocities of the same particle (see Eq. A.1), Eq. (A.7) reduces to

$$\langle \tilde{\mathbf{v}}^*(\mathbf{k},0) \otimes \tilde{\mathbf{v}}(\mathbf{k},t)\rangle = \frac{1}{N^2} \mathbf{P}_\mathbf{k} \sum_{i} \langle \mathbf{v}_i(0) \otimes \mathbf{v}_i(t)\rangle \left\langle e^{-i\mathbf{k}\cdot(\mathbf{r}_i(t)-\mathbf{r}_i(0))} \right\rangle \mathbf{P}_\mathbf{k}. \tag{A.8}$$

For the time discretization of the MPC-SR dynamics $t = nh$, the first average on the right hand side has been calculated by Ripoll et al. in [83] for molecular chaos conditions,

$$\langle \mathbf{v}_i(0) \otimes \mathbf{v}_i(nh)\rangle \quad = \quad \langle \mathbf{v}_i(0) \otimes \mathbf{v}_i(0)\rangle (1-\gamma)^n \tag{A.9}$$

$$(A.1) = \quad \hat{\mathbf{I}} \, \frac{k_B T}{m}(1-\gamma)^n \tag{A.10}$$

The quantity

$$\gamma = \frac{2}{3}(1-\cos\alpha)\left(1-\frac{1}{\varrho}\right) \tag{A.11}$$

depends on two simulation parameters of the MPC-SR method, the average particle density ϱ and the collision angle α (for the definitions, see Sec. 3.2.1). For the second average on the right hand of Eq. (A.8), we use the relation

$$\left\langle e^{-i\mathbf{k}\cdot(\mathbf{r}_i(t)-\mathbf{r}_i(0))} \right\rangle = \left\langle e^{-i\mathbf{k}\cdot\Delta\mathbf{r}_i(t)} \right\rangle = e^{-\frac{1}{6}k^2\left\langle \Delta r_i^2(t)\right\rangle} \tag{A.12}$$

which holds if the $\Delta \mathbf{r}_i(t)$ obey a Gaussian distribution. For its derivation see e.g. Ref. [28], Chap. 4.4. $\langle \Delta r_i^2(t) \rangle$ can be replaced by $6D_0t$ for Brownian particles, where

$$D_0 = \frac{k_B T h}{m} \left(\frac{1}{\gamma} - \frac{1}{2} \right) \tag{A.13}$$

is the diffusion constant of a MPC-SR particle [83]. The assumption that the $\Delta \mathbf{r}_i(t)$ are Gaussian variables is not completely correct for small $t = nh$. However, we will see later that D_0 has a vanishing contribution to the plateau value of $\tilde{T}_{mc}(k)$. Thus Eq. (A.12) becomes

$$\left\langle e^{-i\mathbf{k}\cdot\Delta\mathbf{r}_i(nh)} \right\rangle = e^{-k^2 D_0 nh} \tag{A.14}$$

Inserting Eqs. (A.10) and (A.14) into Eq. (A.8), we find

$$\langle \tilde{\mathbf{v}}^*(\mathbf{k},0) \otimes \tilde{\mathbf{v}}(\mathbf{k},nh) \rangle = \frac{1}{N^2} \mathbf{P_k} \sum_i \hat{\mathbf{I}} \, \frac{k_B T}{m} (1-\gamma)^n \, e^{-k^2 D_0 nh} \mathbf{P_k}. \tag{A.15}$$

Since the sum is indepent of the summation index i, it can be replaced by the factor N. With the property of projection operators $\mathbf{P_k}$

$$\mathbf{P_k} \, \hat{\mathbf{I}} \, \mathbf{P_k} = \mathbf{P_k}^2 = \mathbf{P_k}, \tag{A.16}$$

Eq. (A.15) reads

$$\langle \tilde{\mathbf{v}}^*(\mathbf{k},0) \otimes \tilde{\mathbf{v}}(\mathbf{k},nh) \rangle = \frac{k_B T}{mN} \mathbf{P_k} \left[(1-\gamma) \, e^{-k^2 D_0 h} \right]^n. \tag{A.17}$$

This can be inserted as the integrand into Eq. (A.2). However, since values for $\langle \tilde{\mathbf{v}}^*(\mathbf{k},0) \otimes \tilde{\mathbf{v}}(\mathbf{k},t) \rangle$ are only available for discretes times $t = nh$, the integral has to be replaced by a discrete sum

$$\begin{aligned}
\widetilde{\mathbf{T}}_{mc}(\mathbf{k}) \quad &= \quad \frac{h}{2k_B T} \sum_{n=0}^{\infty} \left[\langle \tilde{\mathbf{v}}^*(\mathbf{k},0) \otimes \tilde{\mathbf{v}}(\mathbf{k},nh) \rangle + \langle \tilde{\mathbf{v}}^*(\mathbf{k},0) \otimes \tilde{\mathbf{v}}(\mathbf{k},(n+1)h) \rangle \right] \\
&= \quad \frac{h}{k_B T} \left[\sum_{n=0}^{\infty} \langle \tilde{\mathbf{v}}^*(\mathbf{k},0) \otimes \tilde{\mathbf{v}}(\mathbf{k},nh) \rangle - \frac{1}{2} \langle \tilde{\mathbf{v}}^*(\mathbf{k},0) \otimes \tilde{\mathbf{v}}(\mathbf{k},0) \rangle \right] \quad \text{(A.18)} \\
(A.17) &= \quad \frac{h}{mN} \mathbf{P_k} \left\{ \sum_{n=0}^{\infty} \left[(1-\gamma) \, e^{-k^2 D_0 h} \right]^n - \frac{1}{2} \right\} \quad \text{(A.19)}
\end{aligned}$$

Since obviously $\left[(1-\gamma) \, e^{-k^2 D_0 h} \right]^n < 1$, the sum in the last line is a geometric progression with

$$\sum_{n=0}^{\infty} q^n = \frac{1}{1-q}, \qquad 0 \le q < 1. \tag{A.20}$$

Thus Eq. (A.19) reads

$$\widetilde{\mathbf{T}}_{mc}(\mathbf{k}) = \frac{h}{mN}\mathbf{P}_{\mathbf{k}}\left[\frac{1}{1-(1-\gamma)\exp\left(-k^2 D_0 h\right)} - \frac{1}{2}\right]. \tag{A.21}$$

With the simulation parameters used in the underlying simulations of Fig. 5.3, one can easily calculate that $D_0 h = 1.029$ for all the four data curves – independendly of h. Furthermore, one can see that the plateau in Fig. 5.3 is only reached for $k \gtrsim 3$. For those wave vectors, the exponential in Eq. (A.21) can be set to zero which gives

$$\widetilde{\mathbf{T}}_{mc}(\mathbf{k}) = \frac{h}{2mN}\mathbf{P}_{\mathbf{k}} \tag{A.22}$$

Since

$$\eta V \tilde{T}(k) = \frac{\eta V}{2}\mathrm{Tr}\,\widetilde{\mathbf{T}}(\mathbf{k}) \tag{A.23}$$

is the quantity plotted in Fig. 5.3, the plateau value of the molecular chaos regime finally reads

$$\eta V \tilde{T}_{mc}(k) = \frac{\eta V}{2}\mathrm{Tr}\,\widetilde{\mathbf{T}}_{mc}(\mathbf{k}) = \frac{\eta V h}{2mN} = \frac{\eta h}{2m\varrho}. \tag{A.24}$$

This result is in very good agreement with the simulation data of Fig. 5.3.

Appendix B

Calculation of the hydrodynamic contribution $\alpha^{h}_{iso,\|,\perp}$ to the sphere diffusion constant in dense rod suspensions

According to the theory of Dhont et al. [47], the influence of hydrodynamic interactions on the self diffusion constant D_s^h of tracer spheres in dense rod suspensions can be described by the relation

$$\sigma^{h}_{iso,\|,\perp}(\phi) = \frac{D^{h}_{iso,\|,\perp}(\phi)}{D_0} = \frac{1}{1 + \alpha^{h}_{iso,\|,\perp}\phi}. \tag{B.1}$$

Here, D_0 is the diffusion constant of spheres at infinite dilution, and $\alpha^{h}_{iso,\|,\perp}$ is a coefficient, which describes the slow down of diffusion due to hydrodynamic interactions between the tracer sphere and the rod network. The practical calculation of $\alpha^{h}_{iso,\|,\perp}$ is described in the following. According to (29) of [47], $\alpha^{h}_{iso,\|,\perp}$ is given by

$$\alpha^{h}_{iso,\|,\perp} = \frac{4}{\pi d^2 L}\hat{\mathbf{v}}_p \cdot \left[\int d\mathbf{R} \oint d\hat{\mathbf{u}} P_0(\hat{\mathbf{u}}|\phi) e^{-\beta V(\mathbf{R},\hat{\mathbf{u}})} \mathbf{M}(\mathbf{R},\hat{\mathbf{u}})\right] \cdot \hat{\mathbf{v}}_p \tag{B.2}$$

Here, $P_0(\hat{\mathbf{u}}|\phi)$ is the orientational probability density function of rod orientations, $V(\mathbf{R},\hat{\mathbf{u}})$ is the steric interaction potential between sphere and rod, and $\mathbf{M}(\mathbf{R},\hat{\mathbf{u}})$ is a tensor, which describes how the flow field induced by a sphere located at a distance $\mathbf{R}$ from the rod center with the direction $\hat{\mathbf{u}}$ is reflected back to the sphere. The choice of the unit vector $\hat{\mathbf{v}}_p$ does not have an effect in the case of isotropic systems, whereas in nematic systems $\hat{\mathbf{v}} = \hat{\mathbf{n}}$ has to be chosen in order to calculate $\alpha_\parallel$, or $\hat{\mathbf{v}} \perp \hat{\mathbf{n}}$ to calculate $\alpha_\perp$ ($\hat{\mathbf{n}}$ is the nematic director). The explicit expression for $\mathbf{M}(\mathbf{R}, \hat{\mathbf{u}})$ is (see Eq. (24) of Ref. [47]).

$$\begin{aligned}\mathbf{M}(\mathbf{R}, \hat{\mathbf{u}}) &= \frac{12(\pi\eta)^2 a_s}{G(\varkappa d, \varkappa L)} \int_{-L/2}^{L/2} dl \mathbf{T}_s(\mathbf{R} - l\hat{\mathbf{u}}) \\ &\quad \cdot \left\{ \hat{\mathbf{I}} - \frac{H(\varkappa d, \varkappa L)}{G(\varkappa d, \varkappa L) + H(\varkappa d, \varkappa L)} \hat{\mathbf{u}} \otimes \hat{\mathbf{u}} \right\} \cdot \mathbf{T}_s(\mathbf{R} - l\hat{\mathbf{u}}) \quad \text{(B.3)}\end{aligned}$$

The tensor $\mathbf{T}_s(\mathbf{r})$ is the isotropic screened hydrodynamic mobility tensor defined by Eq. (5.4) which decays Yukawa-like over a distance, which is characterized by the screening length $\varkappa^{-1}$. The functions $G(\varkappa d, \varkappa L)$ and $H(\varkappa d, \varkappa L)$ are defined by

$$\begin{aligned}G(\varkappa d, \varkappa L) = \int_{\varkappa d/2}^{\varkappa L/2} dx \frac{h_1(x)}{x} &= \frac{1}{2} \left[x^{-2} + \mathrm{E}_1(x) - e^{-x}(x^{-1} + x^{-2}) \right]_{-\varkappa d/2}^{\varkappa L/2} \\ H(\varkappa d, \varkappa L) = \int_{\varkappa d/2}^{\varkappa L/2} dx \frac{h_2(x)}{x} &= \frac{1}{2} \left[-3x^{-2} + \mathrm{E}_1(x) + 3e^{-x}(x^{-1} + x^{-2}) \right]_{-\varkappa d/2}^{\varkappa L/2}\end{aligned}$$

where $\mathrm{E}_1(x) := \int_x^\infty dt \exp(-t)/t$ is the exponential integral. The fraction

$$K := \frac{H(\varkappa d, \varkappa L)}{G(\varkappa d, \varkappa L) + H(\varkappa d, \varkappa L)} \quad \text{(B.4)}$$

appearing in Eq. (B.3) is a constant for a given system and depends only on the rod sizes L, d and the screening length $\varkappa^{-1}$. Therefore it can be calculated before evaluating integrals.

Eq. (B.2) can be equivalently written as

$$\alpha^h_{iso,\parallel,\perp} = \frac{4}{\pi d^2 L} \hat{\mathbf{v}}_p \cdot \oint d\hat{\mathbf{u}} P_0(\hat{\mathbf{u}}|\phi) \mathcal{R}_{\hat{\mathbf{z}}\to\hat{\mathbf{u}}} \underbrace{\left[\int d\mathbf{R} e^{-\beta V(\mathbf{R},\hat{\mathbf{z}})} \mathbf{M}(\mathbf{R}, \hat{\mathbf{z}}) \right]}_{=:\, \mathbf{L}(\hat{\mathbf{z}})} \mathcal{R}^T_{\hat{\mathbf{z}}\to\hat{\mathbf{u}}} \cdot \hat{\mathbf{v}}_p \quad \text{(B.5)}$$

$\mathcal{R}_{\hat{\mathbf{z}}\to\hat{\mathbf{u}}}$ is a rotation matrix which turns a vector parallel to $\hat{\mathbf{z}}$ into a vector of same length parallel to $\hat{\mathbf{u}}$. Let us now focus on the calculation of $\mathbf{L}(\hat{\mathbf{z}})$. Assuming that the rods are perfectly cylindrical, the problem is now symmetrical to the z-axis. Therefore it is convenient to use cylindrical coordinates $R_\parallel$, $R_\perp$ and τ, with

$$\mathbf{R} = \begin{pmatrix} R_\perp \cos\tau \\ R_\perp \sin\tau \\ R_\parallel \end{pmatrix} \quad \text{(B.6)}$$

The interaction potential $V(\mathbf{R},\hat{\mathbf{z}})$ now depends only on $R_\parallel$ and $R_\perp$. For hard-core interactions, it reads

$$V(\mathbf{R},\hat{\mathbf{z}}) = V(R_\parallel, R_\perp) = \begin{cases} \infty & , R_\perp < \frac{d}{2} + a \text{ and } R_\parallel \in \left[-(\frac{L}{2}+a_s), \frac{L}{2}+a_s\right] \\ 0 & , \text{otherwise} \end{cases} \tag{B.7}$$

Accordingly, the Boltzmann probability is

$$e^{-\beta V(R_\parallel, R_\perp)} = \begin{cases} 0 & , R_\perp < \frac{d}{2} + a \text{ and } R_\parallel \in \left[-(\frac{L}{2}+a_s), \frac{L}{2}+a_s\right] \\ 1 & , \text{otherwise} \end{cases} . \tag{B.8}$$

For phantom spheres (spheres are not excluded from the volume occupied by rods), the potential vanishes for all $R_\parallel$, $R_\perp$, i.e., the Boltzmann probability reduces to unity. Inserting Eq. (B.3) into the definition (B.5) of $\mathbf{L}(\hat{\mathbf{z}})$ we obtain

$$\begin{aligned} \mathbf{L}(\hat{\mathbf{z}}) &= \frac{12(\pi\eta)^2 a_s}{G(\varkappa d, \varkappa L)} \int_{-\infty}^{\infty} dR_\parallel \int_0^\infty dR_\perp \int_0^{2\pi} R_\perp \, d\tau \int_{-L/2}^{L/2} dl \mathbf{T}_s(\mathbf{R}-l\hat{\mathbf{z}}) \cdot \Big\{ \hat{\mathbf{I}} \\ &\quad -K\hat{\mathbf{z}} \otimes \hat{\mathbf{z}} \} \cdot \mathbf{T}_s(\mathbf{R}-l\hat{\mathbf{z}}) \\ &= \frac{12(\pi\eta)^2 a_s}{G(\varkappa d, \varkappa L)} \int_{-\infty}^{\infty} dR_\parallel \int_0^\infty dR_\perp \cdot R_\perp \int_{-L/2}^{L/2} dl \\ &\quad e^{-\beta V(R_\parallel - l, R_\perp)} \underbrace{\int_0^{2\pi} d\tau \left[\mathbf{T}_s(\mathbf{R}-l\hat{\mathbf{z}}) \begin{pmatrix} 1 & 0 & 0 \\ 0 & 1 & 0 \\ 0 & 0 & 1-K \end{pmatrix} \mathbf{T}_s(\mathbf{R}-l\hat{\mathbf{z}}) \right]}_{=: \mathbf{N}(r_\parallel - l, R_\perp)} . \end{aligned} \tag{B.9}$$

The integrand depends on τ in such a way that the tensor $\mathbf{N}(r_\parallel - l, R_\perp)$ can be calculated analytically. Therefore we need the explicit form of the integrand. The isotropic screened hydrodynamic mobility tensor $\mathbf{T}_s(\mathbf{R}-l\hat{\mathbf{z}})$ expressed in cylindrical coordinates is

$$\mathbf{T}_s(\mathbf{R}-l\hat{\mathbf{z}}) = \frac{1}{4\pi\eta r^3} \begin{pmatrix} h_1 r^2 + h_2 R_\perp^2 \cos^2\tau & h_2 R_\perp^2 \cos\tau \sin\tau & h_2 R_\perp (R_\parallel - l)\cos\tau \\ h_2 R_\perp^2 \cos\tau \sin\tau & h_1 r^2 + h_2 R_\perp^2 \sin^2\tau & h_2 R_\perp (R_\parallel - l)\sin\tau \\ h_2 R_\perp (R_\parallel - l)\cos\tau & h_2 R_\perp (R_\parallel - l)\sin\tau & h_1 r^2 + h_2 (R_\parallel - l)^2 \end{pmatrix} \tag{B.10}$$

where $r := \sqrt{R_\perp^2 + (R_\parallel - l)^2}$ does not depend on τ. For brevity, we did not write the arguments of the functions $h_1 = h_1(\varkappa r)$ and $h_2 = h_2(\varkappa r)$ in Eq. (B.10). They also do not depend on τ. For symmetry reasons $\mathbf{N}(r_\parallel - l, R_\perp)$ must be diagonal, i.e. all the integrals in the off-diagonal elements vanish. The two eigenvalues in x and y directions are equal (degenerated). We denote them $N_\perp(r_\parallel - l, R_\perp)$.

The eigenvalue in z direction is called $N_\|(r_\| - l, R_\perp)$ in the following. Hence the only two integrals to evaluate are

$$\begin{aligned}
N_\perp(r_\| - l, R_\perp) &= \int_0^{2\pi} d\tau \hat{\mathbf{x}} \cdot \mathbf{T}_s(\mathbf{R} - l\hat{\mathbf{z}}) \begin{pmatrix} 1 & 0 & 0 \\ 0 & 1 & 0 \\ 0 & 0 & 1{-}K \end{pmatrix} \mathbf{T}_s(\mathbf{R} - l\hat{\mathbf{z}}) \cdot \hat{\mathbf{x}} \\
&= \int_0^{2\pi} d\tau \frac{1}{(4\pi\eta)^2 r^6} \Big\{ \big(h_1 r^2 + h_2 R_\perp^2 \cos^2\tau\big)^2 \\
&\quad + \big(h_2 R_\perp^2 \cos\tau \sin\tau\big)^2 + (1-K)\big[h_2 R_\perp (R_\| - l)\cos\tau\big]^2 \Big\} \\
&= \frac{\pi}{(4\pi\eta)^2 r^6} \big\{ 2r^4 h_1^2 + (1-K)(R_\| - l)^2 R_\perp^2 h_2^2 \\
&\quad + R_\perp^4 h_2^2 + 2r^2 R_\perp^2 h_1 h_2 \big\} \qquad \text{(B.11)}
\end{aligned}$$

and

$$\begin{aligned}
N_\|(r_\| - l, R_\perp) &= \int_0^{2\pi} d\tau \hat{\mathbf{z}} \cdot \mathbf{T}_s(\mathbf{R} - l\hat{\mathbf{z}}) \begin{pmatrix} 1 & 0 & 0 \\ 0 & 1 & 0 \\ 0 & 0 & 1{-}K \end{pmatrix} \mathbf{T}_s(\mathbf{R} - l\hat{\mathbf{z}}) \cdot \hat{\mathbf{z}} \\
&= \int_0^{2\pi} d\tau \frac{1}{(4\pi\eta)^2 r^6} \Big\{ \big[h_2 R_\perp (R_\| - l)\cos\tau\big]^2 \\
&\quad + \big[h_2 R_\perp (R_\| - l)\sin\tau\big]^2 + (1-K)\big[h_1 r^2 + h_2 (R_\| - l)^2\big]^2 \Big\} \\
&= \frac{2\pi}{(4\pi\eta)^2 r^6} \Big\{ (R_\| - l)^2 R_\perp^2 h_2^2 + (1-K)\big[r^2 h_1^2 + (R_\| - l)^2 h_2^2\big]^2 \Big\}
\end{aligned}$$

Now we insert $\mathbf{N}(r_\| - l, R_\perp) = \begin{pmatrix} N_\perp(r_\|-l,R_\perp) & 0 & 0 \\ 0 & N_\perp(r_\|-l,R_\perp) & 0 \\ 0 & 0 & N_\|(r_\|-l,R_\perp) \end{pmatrix}$ into Eq. (B.9). Obviously $\mathbf{L}(\hat{\mathbf{z}})$ is diagonal as well, and the only two different eigenvalues are $L_\|(\hat{\mathbf{z}})$ and $L_\perp(\hat{\mathbf{z}})$:

$$\begin{aligned}
\mathbf{L}(\hat{\mathbf{z}}) &= \begin{pmatrix} L_\perp(\hat{\mathbf{z}}) & 0 & 0 \\ 0 & L_\perp(\hat{\mathbf{z}}) & 0 \\ 0 & 0 & L_\|(\hat{\mathbf{z}}) \end{pmatrix} \qquad \text{(B.12)} \\
&= \frac{12(\pi\eta)^2 a_s}{G(\varkappa d, \varkappa L)} \int_{-\infty}^{\infty} dR_\| \int_0^\infty dR_\perp \int_{-L/2}^{L/2} dl R_\perp e^{-\beta V(R_\| - l, R_\perp)} \mathbf{N}(r_\| - l, R_\perp) \qquad \text{(B.13)}
\end{aligned}$$

The problem is now reduced to solving the following integrals

$$\begin{aligned}
L_\perp(\hat{\mathbf{z}}) &= \frac{12(\pi\eta)^2 a_s}{G(\varkappa d, \varkappa L)} \int_{-\infty}^{\infty} dR_\| \int_0^\infty dR_\perp \int_{-L/2}^{L/2} dl R_\perp e^{-\beta V(R_\| - l, R_\perp)} N_\perp(r_\| - l, R_\perp) \\
&= \frac{3\pi a_s}{4G(\varkappa d, \varkappa L)} \int_{-\infty}^{\infty} dR_\| \int_0^\infty dR_\perp \int_{-L/2}^{L/2} dl R_\perp \\
&\quad \cdot e^{-\beta V(R_\| - l, R_\perp)} \frac{1}{r^6} \big\{ 2r^4 h_1^2 + (1-K)(R_\| - l)^2 R_\perp^2 h_2^2 + R_\perp^4 h_2^2 + 2r^2 R_\perp^2 h_1 h_2 \big\}
\end{aligned}$$

and

$$\begin{aligned}
L_\parallel(\hat{\mathbf{z}}) &= \frac{12(\pi\eta)^2 a_s}{G(\varkappa d, \varkappa L)} \int_{-\infty}^{\infty} dR_\parallel \int_0^\infty dR_\perp \int_{-L/2}^{L/2} dl R_\perp e^{-\beta V(R_\parallel - l, R_\perp)} N_\parallel(r_\parallel - l, R_\perp) \\
&= \frac{3\pi a_s}{4G(\varkappa d, \varkappa L)} \int_{-\infty}^{\infty} dR_\parallel \int_0^\infty dR_\perp \int_{-L/2}^{L/2} dl R_\perp \\
&\qquad \cdot e^{-\beta V(R_\parallel - l, R_\perp)} \frac{2}{r^6} \left\{ (R_\parallel - l)^2 R_\perp^2 h_2^2 + (1-K)\left[r^2 h_1^2 + (R_\parallel - l)^2 h_2^2\right]^2 \right\}
\end{aligned}$$

Numerically. Technically, the infinite integral boundaries are replaced by finite values, and it has of course to be ensured that the integral converges over this integration range. Then the threefold integral is solved by Monte Carlo integration. Finally, the numerically determined $\mathbf{L}(\hat{\mathbf{z}})$ are inserted into Eq. (B.5), and the orientational average has to be performed. For isotropic systems, it is straightforward to see that

$$\alpha^h_{iso} = \frac{4}{\pi d^2 L}\, \frac{1}{3} \mathrm{Tr}\mathbf{L}(\hat{\mathbf{z}}) \tag{B.14}$$

For nematic systems, we choose $\hat{\mathbf{n}} = \hat{\mathbf{z}}$. Then it is convenient to express $\hat{\mathbf{u}}$ in spherical coordinates φ and ϑ. Due to the uniaxial symmetry of nematic systems, $P_0(\hat{\mathbf{u}}|\phi)$ can be replaced by $P_0(\vartheta)$. The rotation matrix $\mathcal{R}_{\hat{\mathbf{z}}\to\hat{\mathbf{u}}}$ expressed in spherical coordinates is

$$\mathcal{R}_{\hat{\mathbf{z}}\to\hat{\mathbf{u}}} = \begin{pmatrix} \cos\varphi\cos\vartheta & -\sin\varphi & \cos\varphi\sin\vartheta \\ \sin\varphi\cos\vartheta & \cos\varphi & \sin\varphi\sin\vartheta \\ -\sin\vartheta & 0 & \cos\vartheta \end{pmatrix} \tag{B.15}$$

Inserting this expression for $\mathcal{R}_{\hat{\mathbf{z}}\to\hat{\mathbf{u}}}$ into Eq. (B.5) and replacing $\oint d\hat{\mathbf{u}} P_0(\hat{\mathbf{u}}|\phi)(...)$ by $\frac{1}{2\pi}\int_0^\pi d\vartheta \sin\vartheta P(\vartheta) \int_0^{2\pi} d\varphi(...)$, we find

$$\begin{aligned}
\alpha^h_{\parallel,\perp} &= \frac{4}{\pi d^2 L}\hat{\mathbf{v}}_p \cdot \frac{1}{2\pi} \int_0^\pi d\vartheta \sin\vartheta P(\vartheta) \int_0^{2\pi} d\varphi \begin{pmatrix} \cos\varphi\cos\vartheta & -\sin\varphi & \cos\varphi\sin\vartheta \\ \sin\varphi\cos\vartheta & \cos\varphi & \sin\varphi\sin\vartheta \\ -\sin\vartheta & 0 & \cos\vartheta \end{pmatrix} \\
&\qquad \cdot \begin{pmatrix} L_\perp(\hat{\mathbf{z}}) & 0 & 0 \\ 0 & L_\perp(\hat{\mathbf{z}}) & 0 \\ 0 & 0 & L_\parallel(\hat{\mathbf{z}}) \end{pmatrix} \begin{pmatrix} \cos\varphi\cos\vartheta & \sin\varphi\cos\vartheta & -\sin\vartheta \\ -\sin\varphi & \cos\varphi & 0 \\ \cos\varphi\sin\vartheta & \sin\varphi\sin\vartheta & \cos\vartheta \end{pmatrix} \cdot \hat{\mathbf{v}}_p \\
&= \frac{2}{\pi^2 d^2 L}\hat{\mathbf{v}}_p \cdot \int_0^\pi d\vartheta \sin\vartheta P(\vartheta) \int_0^{2\pi} d\varphi \\
&\qquad \cdot \begin{pmatrix} \cos^2\varphi\cos^2\vartheta L_\perp + \sin^2\varphi L_\perp + \cos^2\varphi\sin^2\vartheta L_\parallel & ... & ... \\ ... & \sin^2\varphi\cos^2\vartheta L_\perp + \cos^2\varphi L_\perp + \sin^2\varphi\sin^2\vartheta L_\parallel & ... \\ ... & ... & \cos^2\varphi\cos^2\vartheta L_\perp + \sin^2\varphi L_\perp + \cos^2\varphi\sin^2\vartheta L_\parallel \end{pmatrix} \cdot \hat{\mathbf{v}}_p.
\end{aligned}$$

We do not write down the off-diagonal items, since they vanish upon integration over $d\varphi$. Now the integration over $d\varphi$ can be done analytically:

$$\begin{aligned}\alpha^h_{\|,\perp} &= \frac{2}{\pi d^2 L}\hat{\mathbf{v}}_p \cdot \int_0^\pi d\vartheta \sin\vartheta P(\vartheta) \\ &\quad \cdot \begin{pmatrix} L_\| \sin^2\vartheta + L_\perp(1+\cos^2\vartheta) & 0 & 0 \\ 0 & L_\| \sin^2\vartheta + L_\perp(1+\cos^2\vartheta) & 0 \\ 0 & 0 & 2\left[L_\| \cos^2\vartheta + L_\perp \sin^2\vartheta\right] \end{pmatrix} \cdot \hat{\mathbf{v}}_p\end{aligned}$$

$\alpha^h_\|$ and $\alpha^h_\perp$ can now be determinded by choosing $\hat{\mathbf{v}}_p = \hat{\mathbf{z}}$ or $\hat{\mathbf{v}}_p \perp \hat{\mathbf{z}}$ respectively. This yields

$$\begin{aligned}\alpha^h_\perp &= \frac{2}{\pi d^2 L} \cdot \int_0^\pi d\vartheta \sin\vartheta P(\vartheta)\left[L_\| \sin^2\vartheta + L_\perp(1+\cos^2\vartheta)\right] \\ &= \frac{2}{\pi d^2 L} \cdot \left[L_\| \left\langle \sin^2\vartheta \right\rangle + L_\perp(1+\left\langle \cos^2\vartheta\right\rangle)\right] \\ &= \frac{4}{3\pi d^2 L} \cdot \left[L_\| \left(1 - \langle P_2\rangle\right) + L_\perp\left(\langle P_2\rangle + 2\right)\right] \qquad \text{(B.16)} \\ \alpha^h_\| &= \frac{4}{\pi d^2 L} \cdot \int_0^\pi d\vartheta \sin\vartheta P(\vartheta)\left[L_\| \cos^2\vartheta + L_\perp \sin^2\vartheta\right] \\ &= \frac{4}{\pi d^2 L} \cdot \left[L_\| \left\langle \cos^2\vartheta\right\rangle + L_\perp \left\langle \sin^2\vartheta\right\rangle\right] \\ &= \frac{4}{3\pi d^2 L} \cdot \left[L_\| \left(2\langle P_2\rangle + 1\right) + 2L_\perp\left(1 - \langle P_2\rangle\right)\right] \qquad \text{(B.17)}\end{aligned}$$

In the last step of the derivations of Eqs. (B.16) and (B.17), the nematic order parameter $\langle P_2\rangle$, defined by Eq. (2.13) was inserted. From Eq. (2.13), it is straightforward to obtain the relations

$$\begin{aligned}\left\langle \cos^2\vartheta\right\rangle &= \frac{1}{3}\left(2\langle P_2\rangle + 1\right) \qquad \text{(B.18)} \\ \text{and} \quad \left\langle \sin^2\vartheta\right\rangle &= \frac{2}{3}\left(1 - \langle P_2\rangle\right) = 1 - \left\langle \cos^2\vartheta\right\rangle \qquad \text{(B.19)} \\ & \qquad \text{(B.20)}\end{aligned}$$

Since the nematic order parameter $\langle P_2\rangle$ is known for each system, also $\alpha^h_{\|,\perp}$ can be calculated directly.

Bibliography

[1] M. Abkarian, C. Lartigue, and A. Viallat, *Tank treading and unbinding of deformable vesicles in shear flow: Determination of the lift force*, Phys. Rev. Lett. **88** (2002), 68103.

[2] M. Adams and S. Fraden, *Phase behavior of mixture's of rods (tobacco mosaic virus) and spheres (polyethylene oxide, bovine serum albumin)*, Biophys. J. **74** (1998), 669.

[3] P. Ahlrichs, R. Everaers, and B. Dünweg, *Screening of hydrodynamic interactions in semidilute polymer solutions: A computer simulation study*, Phys. Rev. E **64** (2001), 40501.

[4] E. Allahyarov and G. Gompper, *Mesoscopic solvent simulations: Multiparticle-collisiondynamics of three-dimensional flows*, Phys. Rev. E **66** (2002), 036702.

[5] M. P. Allen, *Diffusion-coefficient increases with density in hard ellipsoid liquid-crystals*, Phys. Rev. Lett. **65** (1990), 2881.

[6] M. P. Allen and D. J. Tildesley, *Computer simulation of liquids*, Oxford : Clarendon Press, 1989.

[7] H. C. Andersen, *Molecular-dynamics simulations at constant pressure and-or temperature*, J. Chem. Phys. **72** (1980), 2384.

[8] D. Baziwane and Q. A. He, *Gelatin: The paramount food additive*, Food Reviews International **19** (2003), 423.

[9] J. Beaucourt, F. Rioual, T. Seon, T. Biben, and C. Misbah, *Steady to unsteady dynamics of a vesicle in a flow*, Phys. Rev. E **69** (2004), 11906.

[10] H. C. Brinkman, *A calculation of the viscous force exerted by a flowing fluid on a dense swarm of particles*, Appl. Sci. Res. Section A-Mechanics Heat Chemical Engineering Mathematical Methods **1** (1947), 27.

[11] D. Brown and J. H. R. Clarke, *A comparison of constant energy, constant temperature and constant pressure ensembles in molecular-dynamics simulations of atomic liquids*, Mol. Phys. **51** (1984), 1243.

[12] P. A. Buining, C. Pathmamanoharan, J. B. H. Jansen, and H. N. W. Lekkerkerker, *Preparation of colloidal boehmite needles by hydrothermal treatment of aluminum alkoxide precursors*, J. Am. Ceram. Soc. **74** (1991), 1303.

[13] N. A. Campbell and J. B. Reece, *Biologie*, Spektrum, Akademischer Verlag, Gustav Springer, 2003.

[14] I. Cantat and C. Misbah, *Lift force and dynamical unbinding of adhering vesicles under shear flow*, Phys. Rev. Lett. **83** (1999), 880.

[15] Z. Y. Chen, *Nematic ordering in semiflexible polymer-chains*, Macromolecules **26** (1993), 3419.

[16] P. Dalhaimer, D. E. Discher, and T. C. Lubensky, *Crosslinked actin networks show liquid crystal elastomer behaviour, including soft-mode elasticity*, Nat. Phys. **3** (2007), 354.

[17] G. Danker, T. Biben, T. Podgorski, C. Verdier, and C. Misbah, *Dynamics and rheology of a dilute suspension of vesicles: Higher-order theory*, Phys. Rev. E **76** (2007), 41905.

[18] A. A. Darinskii, A. Zarembo, N. K. Balabaev, I. M. Neelov, and F. Sundholm, *Anisotropy of diffusion in a liquid crystalline system of semi-flexible polymer chains*, PCCP **5** (2003), 2410.

[19] P. Davidson and J. C. P. Gabriel, *Mineral liquid crystals*, Curr. Opinion Colloid Interface Sci. **9** (2005), 377.

[20] P. G. de Gennes, *Scaling concepts in polymer physics*, Ithaca, N.Y. : Cornell Univ. Press, 1979.

[21] J. G. de la Torre and V. A. Bloomfield, *Hydrodynamic properties of complex, rigid, biological macromolecules - theory and applications*, Quarterly Reviews of Biophysics **14** (1981), 81.

[22] P. Debye and A. M. Büche, *Intrinsic viscosity, diffusion, and sedimentation rate of polymers in solution*, J. Chem. Phys. **16** (1948), 573.

[23] J. K. G. Dhont, *An introduction to dynamics of colloids*, Elsevier, Amsterdam, 1996.

[24] J. K. G. Dhont, Physics meets Biology, Lecture notes of the 35th. IFF spring school, ch. A2: Translational Brownian motion, Forschungszentrum Jülich, 2004.

[25] J. K. G. Dhont and W. J. Briels, *Viscoelasticity of suspensions of long, rigid rods*, Colloids Surf., A – Physicochemical And Engineering Aspects **213** (2003), 131.

[26] Z. Dogic and S. Fraden, Soft Matter, vol. 2, ch. 1: Phase bahavior of rod-like viruses and virus-sphere mixtures, WILEY-VCH Verlag, Weinheim, 2006.

[27] Z. Dogic, K. R. Purdy, E. Grelet, M. Adams, and S. Fraden, *Isotropic-nematic phase transition in suspensions of filamentous virus and the neutral polymer dextran*, Phys. Rev. E **69** (2004), 051702.

[28] M. Doi and S.F. Edwards, *The theory of polymer dynamics*, Clarendon Press, Oxford, 1986.

[29] X. M. Dong, T. Kimura, J. F. Revol, and D. G. Gray, *Effects of ionic strength on the isotropic-chiral nematic phase transition of suspensions of cellulose crystallites*, Langmuir **12** (1996), 2076.

[30] B. Dünweg, *Molecular-dynamics algorithms and hydrodynamic screening*, J. Chem. Phys. **99** (1993), 6977.

[31] B. Dünweg and K. Kremer, *Molecular-dynamics simulation of a polymer-chain in solution*, J. Chem. Phys. **99** (1993), 6983.

[32] P. Espanol and P. Warren, *Statistical-mechanics of dissipative particle dynamics*, Europhys. Lett. **30** (1995), 191.

[33] D. Faires and R. L. Burden, *Numerische methoden*, Spektrum, 1994.

[34] J. H. Ferziger and M. Peric, *Computational methods for fluid dynamics*, Springer Verlag, 1999.

[35] H. Fynewever and A. Yethiraj, *Phase behavior of semiflexible tangent hard sphere chains*, J. Chem. Phys. **108** (1998), 1636.

[36] I. O. Götze, H. M. Harreis, and C. N. Likos, *Tunable effective interactions between dendritic macromolecules*, J. Chem. Phys. **120** (2004), 7761.

[37] I. O. Götze, H. Noguchi, and G. Gompper, *Relevance of angular momentum conservation in mesoscale hydrodynamics simulations*, Phys. Rev. E **76** (2007), 046705.

[38] M. S. Green, *Markoff random processes and the statistical mechanics of time-dependent phenomena .2. irreversible processes in fluids*, J. Chem. Phys. **22** (1954), 398.

[39] R. D. Groot and P. B. Warren, *Dissipative particle dynamics: Bridging the gap between atomistic and mesoscopic simulation*, J. Chem. Phys. **107** (1997), 4423.

[40] M. Hecht, J. Harting, T. Ihle, and H. J. Herrmann, *Simulation of claylike colloids*, Phys. Rev. E **72** (2005), 011408.

[41] P. J. Hoogerbrugge and J. M. V. A. Koelman, *Simulating microscopic hydrodynamic phenomena with dissipative particle dynamics*, Europhys. Lett. **19** (1992), 155.

[42] T. Ihle and D. M. Kroll, *Stochastic rotation dynamics: A Galilean-invariant mesoscopic model for fluid flow*, Phys. Rev. E **63** (2001), 020201.

[43] T. Ihle and D. M. Kroll, *Stochastic rotation dynamics. I. Formalism, Galilean invariance, and Green-Kubo relations*, Phys. Rev. E **67** (2003), 066705.

[44] T. Ihle and D. M. Kroll, *Stochastic rotation dynamics II: Transport coefficients, numerics, long time tails*, Phys. Rev. E **67** (2003), 066706.

[45] B. A. Imhof and D. Dunon, *Basic mechanism of leukocyte migration*, Hormone And Metabolic Research **29** (1997), 614.

[46] K. Kang, J. Gapinski, M. P. Lettinga, J. Buitenhuis, G. Meier, M. Ratajczyk, J. K. G. Dhont, and A. Patkowski, *Diffusion of spheres in crowded suspensions of rods*, J. Chem. Phys. **122** (2005), 044905.

[47] K. Kang, A. Wilk, J. Buitenhuis, A. Patkowski, and J. K. G. Dhont, *Diffusion of spheres in isotropic and nematic suspensions of rods*, J. Chem. Phys. **124** (2006), 044907.

[48] K. Kang, A. Wilk, A. Patkowski, and J. K. G. Dhont, *Diffusion of spheres in isotropic and nematic networks of rods: Electrostatic interactions and hydrodynamic screening*, J. Chem. Phys. **126** (2007), 214501.

[49] V. Kantsler and V. Steinberg, *Transition to tumbling and two regimes of tumbling motion of a vesicle in shear flow*, Phys. Rev. Lett. **96** (2006), 36001.

[50] S. R. Keller and R. Skalak, *Motion of a tank-treading ellipsoidal particle in a shear-flow*, J. Fluid Mech. **120** (1982), 27.

[51] A. R. Khokhlov and A. N. Semenov, *Liquid-crystalline ordering in the solution of long persistent chains*, Physica A **108** (1981), 546.

[52] N. Kikuchi, C. M. Pooley, J. F. Ryder, and J. M. Yeomans, *Transport coefficients of a mesoscopic fluid dynamics model*, J. Chem. Phys. **119** (2003), 6388.

[53] A. J. C. Ladd, *Short-time motion of colloidal particles - numerical-simulation via a fluctuating lattice-boltzmann equation*, Phys. Rev. Lett. **70** (1993), 1339.

[54] P. Lallemand and L. S. Luo, *Theory of the lattice Boltzmann method: Dispersion, dissipation, isotropy, Galilean invariance, and stability*, Phys. Rev. E **61** (2000), 6546.

[55] A. Lamura and G. Gompper, *Numerical study of the flow around a cylinder using multi-particle collision dynamics*, Eur. Phys. J. **9** (2002), 477.

[56] A. Lamura, G. Gompper, T. Ihle, and D. M. Kroll, *Multi-particle collision dynamics: Flow around a circular and a square cylinder*, Europhys. Lett. **56** (2001), 319.

[57] V. V. Lebedev, K. S. Turitsyn, and S. S. Vergeles, *Dynamics of nearly spherical vesicles in an external flow*, Phys. Rev. Lett. **99** (2007), 218101.

[58] M. P. Lettinga, E. Barry, and Z. Dogic, *Self-diffusion of rod-like viruses in the nematic phase*, Europhys. Lett. **71** (2005), 692.

[59] M. P. Lettinga and E. Grelet, *Self-diffusion of rodlike viruses through smectic layers*, Phys. Rev. Lett. **99** (2007), 197802.

[60] M. P. Lettinga and Z. K. Zhang, private communication.

[61] J. A. Levy, H. Fraenkel-Conrat, and R. A. Owens, *Virology*, Prentice Hall, 1994.

[62] D. Lortz, *Hydrodynamik*, BI-Wissenschaftlicher-Verlag, Mannheim, Leipzig, Wien, Zürich, 1993.

[63] H. Löwen, *Anisotropic self-diffusion in colloidal nematic phases*, Phys. Rev. E **59** (1999), 1989.

[64] A. Malevanets and R. Kapral, *Mesoscopic model for solvent dynamics*, J. Chem. Phys. **110** (1999), 8605.

[65] A. Malevanets and J. M. Yeomans, *Dynamics of short polymer chains in solution*, Europhys. Lett. **52** (2000), 231.

[66] G. R. McNamara and G. Zanetti, *Use of the Boltzmann-equation to simulate lattice-gas automata*, Phys. Rev. Lett. **61** (1988), 2332.

[67] S. Meßlinger, B. Schmidt, H. Noguchi, and G. Gompper, *Dynamical regimes and hydrodynamic lift forces on vesicles under shear*, in preparation.

[68] C. Misbah, *Vacillating breathing and tumbling of vesicles under shear flow*, Phys. Rev. Lett. **96** (2006), 28104.

[69] K. Mussawisade, M. Ripoll, R. G. Winkler, and G. Gompper, *Dynamics of polymers in a particle-based mesoscopic solvent*, J. Chem. Phys. **123** (2005), 144905.

[70] J. Newman, H. L. Swinney, and L. A. Day, *Hydrodynamic properties and structure of fd virus*, J. Mol. Biol. **116** (1977), 593.

[71] H. Noguchi and G. Gompper, *Fluid vesicles with viscous membranes in shear flow*, Phys. Rev. Lett. **93** (2004), 258102.

[72] H. Noguchi and G. Gompper, *Dynamics of fluid vesicles in shear flow: Effect of membrane viscosity and thermal fluctuations*, Phys. Rev. E **72** (2005), 011901.

[73] H. Noguchi and G. Gompper, *Swinging and tumbling of fluid vesicles in shear flow*, Phys. Rev. Lett. **98** (2007), 128103.

[74] H. Noguchi, N. Kikuchi, and G. Gompper, *Particle-based mesoscale hydrodynamic techniques*, Europhys. Lett. **78** (2007), 10005.

[75] P. Olla, *The lift on a tank-treading ellipsoidal cell in a shear flow*, J. Phys. II **7** (1997), 1533.

[76] P. Olla, *The role of tank-treading motions in the transverse migration of a spheroidal vesicle in a shear flow*, J. Phys. A: Math. Gen. **30** (1997), 317.

[77] L. Onsager, *The effects of shape on the interaction of colloidal particles*, Ann. N.Y. Acad. Sci. **51** (1949), 627.

[78] J. Plastino, S. Olivier, and C. Sykes, *Actin filaments align into hollow comets for rapid vasp-mediated propulsion*, Current Biology **14** (2004), 1766.

[79] C. Pozrikidis, *Boundary integral and singularity methods for linearized viscous flow*, Cambridge Texts in applied mathematics, 1992.

[80] M. Ripoll, Computational Condensed Matter Physics, Lecture notes of the 37th. IFF spring school, ch. B5 Mesoscale hydrodynamics simulations, Forschungszentrum Jülich, 2006.

[81] M. Ripoll, M. H. Ernst, and P. Espanol, *Large scale and mesoscopic hydrodynamics for dissipative particle dynamics*, J. Chem. Phys. **115** (2001), 7271.

[82] M. Ripoll, K. Mussawisade, R. G. Winkler, and G. Gompper, *Low-Reynolds-number hydrodynamics of complex fluids by multi-particle collision dynamics*, Europhys. Lett. **68** (2004), 106.

[83] M. Ripoll, K. Mussawisade, R. G. Winkler, and G. Gompper, *Dynamic regimes of fluids simulated by multiparticle-collision dynamics*, Phys. Rev. E **72** (2005), 016701.

[84] M. Ripoll, R. G. Winkler, and G. Gompper, *Star polymers in shear flow*, Phys. Rev. Lett. **96** (2006), 188302.

[85] M. Ripoll, R. G. Winkler, and G. Gompper, *Hydrodynamic screening of star polymers in shear flow*, Eur. Phys. J. E **23** (2007), 349.

[86] G. Schütz, Physics meets Biology, Lecture notes of the 35th. IFF spring school, ch. A1 Statistical mechanics, Forschungszentrum Jülich, 2004.

[87] U. Seifert, *Hydrodynamic lift on bound vesicles*, Phys. Rev. Lett. **83** (1999), 876.

[88] W. Stöber, A. Fink, and E. Bohn, *Controlled growth of monodisperse silica spheres in micron size range*, J. Colloid Interface Sci. **26** (1968), 62.

[89] A. Stoobants, H. N. W. Lekkerkerker, and T. Odijk, *Effect of electrostatic interaction on the liquid-crystal phase-transition in solutions of rodlike polyelectrolytes*, Macromolecules **19** (1986), 2232.

[90] S. Sukumaran and U. Seifert, *Influence of shear flow on vesicles near a wall: A numerical study*, Phys. Rev. E **64** (2001), 11916.

[91] T. M. Svitkina, A. B. Verkhovsky, K. M. McQuade, and G. G. Borisy, *Analysis of the actin-myosin ii system in fish epidermal keratocytes: Mechanism of cell body translocation*, J. Cell Biol. **139** (1997), 397.

[92] S. Tanaka and M. Ataka, *Protein crystallization induced by polyethylene glycol: A model study using apoferritin*, J. Chem. Phys. **117** (2002), 3504.

[93] J. X. Tang and S. Fraden, *Isotropic-cholesteric phase-transition in colloidal suspensions of filamentous bacteriophage-fd*, Liq. Cryst. **19** (1995), 459.

[94] M. M. Tirado, C. L. Martinez, and J. G. de la Torre, *Comparison of theories for the translational and rotational diffusion-coefficients of rod-like macromolecules - application to short DNA fragments*, J. Chem. Phys. **81** (1984), 2047.

[95] R. Tuinier, J. K. G. Dhont, and C. G. De Kruif, *Depletion-induced phase separation of aggregated whey protein colloids by an exocellular polysaccharide*, Langmuir **16** (2000), 1497.

[96] A. van Blaaderen and A. Vrij, *Synthesis and characterization of monodisperse colloidal organo-silica spheres*, J. Colloid Interface Sci. **156** (1993), 1.

[97] D. Voet and J.G. Voet, *Biochemistry*, Wiley, New York, 1995.

[98] G. J. Vroege and H. N. W. Lekkerkerker, *Phase-transitions in lyotropic colloidal and polymer liquid-crystals*, Rep. Prog. Phys. **55** (1992), 1241.

[99] P. Wesseling, *Principles of computational fluid dynamics*, Springer-Verlag Berlin Heidelberg New York, 2000.

[100] R. G. Winkler, P. Reineker, and L. Harnau, *Models and equilibrium properies of stiff molecular chains*, J. Chem. Phys. **101** (1994), 8119.

[101] R. G. Winkler, A. Ripoll, K. Mussawisade, and G. Gompper, *Simulation of complex fluids by multi-particle-collision dynamics*, Comput. Phys. Commun. **169** (2005), 326.

[102] A. Yethiraj and H. Fynewever, *Isotropic to nematic transition in semiflexible polymer melts*, Mol. Phys. **93** (1998), 693.

[103] Z. K. Zhang, *Surface modification of colloidal silica particles and fd viruses*, Ph.D. thesis, University of Twente, Enschede, Netherlands, 2007.

[104] Z. K. Zhang and J. Buitenhuis, *Synthesis of uniform silica rods, curved silica wires, and silica bundles using filamentous fd virus as a template*, Small **3** (2007), 424.

[105] B. H. Zimm, *Dynamics of polymer molecules in dilute solution - viscoelasticity, flow birefringence and dielectric loss*, J. Chem. Phys. **24** (1956), 269.

List of Symbols

$\otimes$	Dyadic product
$\widetilde{(...)}$	Fourier transform of (...)
α	Collision angle, page 28
$\alpha^h_{iso,\|,\perp}$	Coefficient for the hydrodynamic contribution to sphere diffusion, page 84
$\alpha^s_{iso,\|,\perp}$	Coefficient for the steric contribution to sphere diffusion, page 84
α_s	Order parameter of the vesicle shape, see equation (7.7), page 99
β	Inverse thermal energy $\beta = 1/(k_B T)$
Γ	Velocity-gradient tensor, see equation (7.4), page 97
γ	Friction constant, see equation (2.32), page 23
γ_0	Rod friction constant without hydrodynamics, page 35
γ_s	Friction constant of a sphere (Stokes friction), page 36
$\dot{\gamma}^*$	Reduced shear rate, see equation (7.9), page 99
$\Delta(\varkappa^{-1})$	Error of $\varkappa^{-1}$, see equation (5.35), page 71
$\Delta\varrho$	Difference of (heavy) mass densities between the inner and the outer fluid in vesicle, page 108
$\Delta(b)$	Error of b, page 71
Δt	Time difference between two consecutively recorded monomer configurations., page 42
ε	Strength of U_{LJ}, page 39

ζ_θ	Friction constant for θ in the generalized KS theory, see equation (7.18), page 103
ζ_α	Friction constant for α_s in the generalized KS theory, see equation (7.18), page 103
η	Viscosity, page 11
η_{coll}	Collisional viscosity, page 29
η_{eff}	Effective (macroscopic) viscosity of rod suspensions, page 71
η_{in}, η_{out}	Viscosity inside and outside of a vesicle, page 97
η_{kin}	Kinetic viscosity, page 29
θ	Inclination angle of a vesicle, see equation (7.8), page 99
κ	Bending rigidity, page 39
$\varkappa$	Hydrodynamic screening constant in the isotropic systems, page 60
$\varkappa^{-1}$	Isotropic hydrodynamic screening length, page 60
$\varkappa_{(...)}$	Hydrodynamic screening constant for direction (...) in anisotropic systems, page 62
$\varkappa_{(...)}^{-1}$	Hydrodynamic screening length for direction (...) in anisotropic systems, page 62
$\Lambda_{\parallel,\perp}$	Eigenvalues of the gyration tensor, page 45
λ_c	Hydrodynamic cutoff length, page 68
$\Lambda_{min,max}$	Eigenvalues of the gyration tensor of vesicles, page 99
ν	Numerical constant. Appears in the calculation of $\alpha^s_{iso,\parallel,\perp}$, see equation (6.5), page 84
ξ	Mesh size, see equation (2.18), page 20
ξ_c	Length scale over which flow velocities are coupled by rods, page 76
Π	Moment of inertia, page 32

ρ	Dimensionless concentration, page 19
ρ_I	Dimensionless concentration of the isotropic phase at I-N coexistence, see equation (2.16), page 19
ρ_N	Dimensionless concentration of the nematic phase at I-N coexistence, see equation (2.16), page 19
ϱ	number density of MPC particles, page 27
ϱ_m	Mass density
ϱ_{rods}	Rod number density, page 19
σ	The interaction radius of U_{LJ} is $\sqrt[6]{2}\sigma$, page 39
τ	Viscosity contrast, see equation (7.2), page 97
τ^*	Critical viscosity contrast for the TT-TB transition, page 101
τ_B	Brownian time, page 22
Φ	Total potential energy, page 25
ϕ^*	Overlap volume fraction, see equation (2.17), page 20
ϕ	Rod volume fraction, page 19
$\boldsymbol{\Omega}$	Rotational part of $\boldsymbol{\Gamma}$, see equation (7.6), page 98
ω	Angular velocity
$\mathbf{A}$	Solution matrix of the ASCFE in Fourier space, page 62
A	Enclosed area of a two-dimensional vesicle, page 96
a	Collision box size, page 28
A_0	Enclosed vesicle area if $U_A = 0$, page 105
a_1, a_2	Half-axes of an ellipse, page 101
a_s	Tracer sphere radius, page 83
A^*	Reduced enclosed area of a two-dimensional vesicle, see equation (7.1), page 96

$\mathbf{b}$	Random shift vector, page 29
B	Crucial quantity for the inclination angle in the KS theory [50], see equation (7.13), page 101
b	Axis intercept in the $1/(\eta V\widetilde{T}(k))$ vs. k^2 plot. Used for fitting $\varkappa$, see equation (5.33), page 70
$B(\phi)$	Volume fraction dependent length scale of rod-rod distances, page 75
D	Diffusion constant, general, see equation (2.26), page 22
d	Steric rod diameter, page 35
D_0	Rod diffusion constant at infinite dilution without hydrodynamics, page 35
d_{dim}	Dimensionality
$D^{h}_{iso,\Vert,\perp}$	Tracer diffusion constant for phantom spheres, see equation (6.9), page 86
$D^{hs}_{iso,\Vert,\perp}$	Tracer diffusion constant for EV+HI spheres, see equation (6.5), page 86
$\widehat{D}^{h}_{iso,\Vert,\perp}$	Normalized tracer diffusion constant for phantom spheres, see equation (6.10), page 86
$\widehat{D}^{hs}_{iso,\Vert,\perp}$	Normalized tracer diffusion constant for EV+HI spheres, see equation (6.6), page 86
d_{hyd}	Hydrodynamic rod diameter, page 35
D_{iso}	Isotropic diffusion constant. Average of $D_{\Vert}$ and $D_{\perp}$, see equation (2.28), page 23
D_p	Diffusion constant of a heavy particle in MPC-SR solvents, page 40
$D_{\Vert}$	Diffusion constant for motion parallel to $\hat{\mathbf{n}}$, see equation (2.28), page 23
$D_{\perp}$	Diffusion constant for motion perpendicular to $\hat{\mathbf{n}}$, see equation (2.28), page 23
D_s	Diffusion constant of a sphere (Stokes diffusion), page 36
$D^{s}_{iso,\Vert,\perp}$	Tracer diffusion constant for EV–HI spheres, see equation (6.7), page 86

$\widehat{D}^{s}_{iso,\parallel,\perp}$	Normalized tracer diffusion constant for EV–HI spheres, see equation (6.8), page 86
$\widehat{D}_{iso,\parallel,\perp}(\rho)$	Normalized rod diffusion constants, see equation (4.20), page 48
$\mathbf{E}$	Elongational part of $\mathbf{\Gamma}$, see equation (7.5), page 98
E_{kin}	Kinetic energy
$\hat{\mathbf{e}}_{min,max}$	Eigenvectors of the gyration tensor of vesicles, page 99
E_{th}	Thermal energy, see equation (3.11), page 29
$\mathbf{f}$	Body force, page 59
F	Free energy
$\mathbf{f}_{ext}$	External body force, page 11
$\mathbf{F}_G$	Gravitational force, page 108
$\mathbf{f}_G$	Gravitational body force, page 108
$\mathbf{F}_i$	Force acting on monomer i, see equation (3.1), page 25
F_L	Lift force, page 114
$\mathbf{G}$	Tensor of gyration, page 45
g	Strength of the gravitational field, page 108
$\mathbf{g}_O$	Pressure vector, see equation (2.7), page 13
h	Collision time, page 28
h_1, h_2	Auxiliary functions in the explicit expression of $\mathbf{T}_s(\mathbf{r})$, see equation (5.6), page 61
h_{MD}	MD time step, page 26
$\hat{\mathbf{I}}$	Identity matrix, page 45
$\mathbf{k}$	Wave vector
k_A	Parameter controlling the strength of U_A, page 105

k_c	Hydrodynamic cutoff wave number, page 68
k_{sp}	Spring constant of the bond potential U_{sp}, page 39
L	Rod length, see equation (2.13), page 19
l	Equilibrium bond length in rods/vesicles, page 39
l_c	Characteristic length scale in a soft matter system, page 12
L_{iso}	Linear size of cubic simulation boxes $L_{iso} = L_x = L_y = L_z$, page 67
l_p	Persistence length, see equation (2.22), page 21
$L_{x,y,z}$	Size of the simulation box in x,y and z directions, page 28
M	Monomer mass, page 38
m	MPC particle mass
m_{box}	Mass of a virtual cluster particle, page 30
m_i	Mass of monomer i, page 25
m_{in}, m_{out}	MPC particle masses inside and outside of the vesicle, page 106
$\mathbf{m}$	Integer vector, page 67
$\hat{\mathbf{n}}$	Nematic director, see equation (2.12), page 18
N	total MPC particle number
n	Number of monomers in one rod/vesicle
N_c	Number of MPC particles in a particular box, page 32
N_f	Number of recorded monomer configuration per simulation, page 42
N_{virt}	Number of virtual wall particles in a collision box crossing a wall, page 33
$n_{x,y,z}$	Number of collision boxes in x,y and z directions, page 28
P	Perimeter of a two-dimensional vesicle, page 96
p	Pressure

$\langle P_2 \rangle$	Nematic order parameter, see equation (2.13), page 18
$\mathbf{r}$	Position
R	Curvature radius of a semiflexible rod, page 20
R_1, R_2	Principal radii of local curvature in three-dimensional membranes, page 96
R_A	Vesicle radius defined by the enclosed area, page 103
$\mathcal{R}_\alpha(\hat{\mathbf{u}}_{ran})$	Random rotation matrix in the MPC-SR and random MPC methods, page 28
$\mathbf{r}_{cm}$	Center of mass of rods/vesicles
Re	Reynolds number, see equation (2.3), page 12
R_e	End-to-end distance of a semiflexible rod, see equation (2.23), page 21
$\mathbf{r}_i$	Position of particle i
$\mathbf{r}_{i,c}$	Position of particle i relative to the center of mass, page 32
R_p	Vesicle radius defined by the vesicle perimeter, page 99
$\mathbf{R}_i^\pm$	Bond vectors in rods/vesicles, page 38
$\mathcal{R}_{\hat{\mathbf{u}}\to\hat{\mathbf{x}}}$	Rotation matrix which turn vectors around the axis $\hat{\mathbf{x}} \times \hat{\mathbf{u}}$ such that $\mathcal{R}_{\hat{\mathbf{u}}\to\hat{\mathbf{x}}}\hat{\mathbf{u}} = \hat{\mathbf{x}}$, see equation (4.15), page 44
$\mathbf{S}$	Hydrodynamic screening tensor, see equation (5.7), page 62
s	Arc length along the rod contour between one rod end and a certain site on the rod, page 20
S'	Co-rotating frame in single-rod diffusion, page 44
s_b	Distance of a MPC particle from a bond of the vesicle membrane, page 107
$\mathbf{T}_O$	Oseen tensor, see equation (2.6), page 13
$\mathbf{T}_a$	Anisotropic screened hydrodynamic mobility tensor, page 62
$\hat{\mathbf{t}}_1$	Tangential vector along the rod contour, see equation (2.21), page 21

t_L	Time required for a rod to reach a MSD $W_{iso}(t = t_L) = L^2$, page 49
$\widetilde{T}_{mc}(k)$	$\widetilde{T}$ in MPC-SR solvent under molecular chaos, see equation (5.25), page 68
$\widetilde{T}_{\parallel}(k)$	Scalar function of $\widetilde{\mathbf{T}}_a(\mathbf{k})$ which is used for fitting $\varkappa_{\perp}^{-1}$, page 74
$\widetilde{T}_{\perp}(k)$	Scalar function of $\widetilde{\mathbf{T}}_a(\mathbf{k})$ which is used for fitting $\varkappa_{\parallel}^{-1}$, page 74
$\mathbf{T}_s$	Isotropic screened hydrodynamic mobility tensor, page 61
$\widetilde{T}_s(k)$	Scalar function of $\widetilde{\mathbf{T}}_s(\mathbf{k})$ which is used for fitting $\varkappa^{-1}$, page 70
t_{tot}	Total simulated time of a simulation, page 42
$\hat{\mathbf{u}}$	Unit vector representing the rod orientation
U_{bend}	Bending potential in rods/vesicles, page 39
U_G	Gravitational potential, page 108
U_{LJ}	Shifted truncated Lennard-Jones potential, page 39
$\hat{\mathbf{u}}_{ran}$	Unit vector representing the orientation for the random rotation in the MPC-SR and random MPC methods, page 28
U_{sp}	Spring potential for bonds, page 39
U_{Wall}	Wall potential for vesicles, see equation (7.30), page 108
$\mathbf{v}$	Flow velocity
V	Volume
$\mathbf{v}_{box}$	Thermal velocity of a virtual cluster particle, page 30
v_c	Characteristic velocity in a soft matter system, page 12
$\mathbf{v}_{cm}$	Center of mass velocity
$\mathbf{v}_e$	Elongational flow velocity in shear, see equation (7.5), page 98
$\mathbf{v}_i$	Velocity of particle i
$\mathbf{v}_r$	Rotational flow velocity in shear, see equation (7.6), page 98
$\mathbf{v}_i^{ran}$	Random velocity in the MPC-AT+a method, page 32

$W_{\parallel}(t)$	Mean square displacement for diffusion parallel to $\hat{\mathbf{n}}$, see equation (2.28), page 23
$W_{\perp}(t)$	Mean square displacement for diffusion perpendicular to $\hat{\mathbf{n}}$, see equation (2.28), page 23
$W(t)$	Mean square displacement, see equation (2.25), page 22

Index

Danksagung

Ich bedanke mich bei Gerhard Gompper, der mir die Möglichkeit gab, an diesen interessanten Themen zu forschen. Er hat meine Doktorarbeit hervorragend betreut und sich viel Zeit für anregende Diskussionen genommen. Desweiteren gab er mir viel Freiheit in der Gestaltung meiner Arbeit und war immer offen für meine Ideen.
Ich bedanke mich bei Joachim Krug, dass er sich selbstverständlich bereiterklärt hat, die Zweitkorrektur dieser Arbeit zu übernehmen.
Zum Gelingen dieser Arbeit haben durch interessante Diskussionen beigetragen: Roland G. Winkler zu den Themen Hydrodynamik, hydrodynamischer Mobilitätstensor und hydrodynamische Abschirmung, sowie Jan K. G. Dhont unser Kooperationspartner und Ansprechpartner zum Thema Kugeldiffusion. Weitere interessante Diskussionen gab es mit Pavlik Lettinga, unserem experimentellen Kooperationspartner, über Stäbchendiffusion, sowie mit meinem Kollegen Hiroshi Noguchi, mit dem ich auf dem Gebiet der Vesikel-Dynamik zusammen gearbeitet habe. Mein Praktikant Benjamin Schmidt hat entscheident bei der Entwicklung und beim Testen des Simulationsprogramms zur Vesikel-Dynamik beigetragen. Mein Bürokollege Jens Elgeti war stets der erste Ansprechpartner für mich, sowohl bei wissenschaftlichen, als auch bei Alltagsfragen.
Für das gründliche Durchlesen dieser Arbeit bedanke ich mich bei Gerhard Gompper, Jens Elgeti, Marisol Ripoll, Apratim Chatterji, Daniel Lüsebrink und Frank Reininghaus.
Bei unserer Sekretärin Helga Paffen möchte ich mich dafür bedanken, dass sie mir Verwaltungsarbeiten abgenommen hat, die nicht selbstverständlich waren. Für Hilfestellungen und Problemlösungen im Bereich der Computernutzung bedanke ich mich bei Elmar Westphal und Joseph Heinen. Ferner möchte ich mich bei unserem gesamten Forschungsteam für die gute Zusammenarbeit und das schöne Arbeitsklima bedanken.
Meiner Frau Anna Fela und meiner Tochter Malena habe ich weit mehr zu verdanken, als dass sie mir durch die Freude, die ich an ihnen habe, die Kraft

gegeben haben, dieses Projekt meistern zu können.
Ein besonderer Dank geht an meine Schwiegereltern und Eltern, die mich besonders in der Endphase der Doktorarbeit unterstützt haben und jederzeit für die Betreuung meiner Tochter da waren. Ein weiteres Dankeschön geht an meine Eltern, die mir durch ihre finanzielle Unterstützung das Studium und damit die Voraussetzungen für die Doktorarbeit ermöglicht haben.
Vielen Dank!

Kurzzusammenfassung

Wir untersuchen die Dynamik von Suspensionen stäbchenförmiger Kolloide und von Vesikeln mit Hilfe von Computer-Simulationen. Dies sind zwei Beispiele für die reichhaltige Dynamik in "Weiche-Materie"-Systemen, die sich dadurch auszeichnet, dass sich aufgrund der langen Relaxationszeiten einerseits die Dynamik leicht experimentell untersuchen lässt und andererseits die Systeme in einen Nichtgleichgewichtszustand gebracht werden können. Beiden Systemen gemeinsam ist, dass sie als Modellsysteme für Transportphänomene in der Biologie der Zelle dienen, und dass wir besonders den Einfluss der Hydrodynamik untersuchen. Letzteres realisieren wir dadurch, dass wir die Simulationsmethode "multi particle collision dynamics" (MPC) verwenden, mit der das Lösungsmittel explizit mitsimuliert wird.

Wir berechnen die Diffusionskonstanten von stabförmigen Kolloiden in isotropen und nematischen Stäbchensystemen. Die Stäbchendiffusion wird durch sterische und hydrodynamische Wechselwirkungen zwischen Stäbchen stark beeinflusst. Aufgrund der Anisotropie der nematischen Phase ist auch das Diffusionsverhalten in der nematischen Phase anisotrop. Unsere Untersuchungen zeigen, dass hydrodynamische Effekte für eine Erhöhung der Diffusionskonstanten sorgen. Ferner zeigen die Simulationen, dass die Anisotropie der Diffusion in nematischen Systemen vom Aspekt-Verhältnis der Stäbchen abhängt. Die Simulationsergebnisse werden mit Ergebnissen unserer experimentellen Kooperationspartner (Gruppe J. K. G. Dhont, FZ-Jülich) verglichen, die Diffusionskonstanten von *fd* Viren messen. Unsere Beobachtungen zur hydrodynamischen Verstärkung und zur Anisotropie der Stäbchendiffusion sind in guter Übereinstimmung mit den experimentellen Daten.

In die oben beschriebenen Kolloidsysteme werden kugelförmige Tracer-Kolloide in geringer Konzentration zugegeben, deren Diffusionskonstanten bestimmt werden. Auch hier ist das Diffusionsverhalten in der nematischen Phase anisotrop. Der Einfluss des Stäbchennetzwerks auf die Kugeldiffusion kann auf sterische sowie hydrodynamische Effekte zurückgeführt werden. Die Ergebnisse sind in Übereinstimmung mit theoretischen Vorhersagen, in der insbesondere hydrodynamische Effekte mitberücksichtigt werden. Eine wichtige Größe für die Berechnung der theoretischen Diffusionskonstanten ist die hydrodynamische Abschirmlänge, die experimentell schwer zugänglich ist, jedoch in Simulationen direkt bestimmt werden kann.

Die hohe Konzentration der Stäbchen führt dazu, dass die sonst langreichweitigen hydrodynamischen Wechselwirkungen (Abhängigkeit ist proportional zum reziproken Abstand) zwischen Kolloiden effektiv abgeschirmt werden, so dass sie exponentiell abfallen. Wir haben eine Methode entwickelt, mit der die Abschirmlängen aus den Gleichgewichtsfluktuationen der Scherwellen des Lösungsmittels bestimmt werden können. Damit sind wir auch in der Lage, anisotrope Abschirmung in nematischen Systemen zu berechnen. Wir können zeigen, dass hydrodynamische Abschirmlängen von der Größenordnung typischer Nachbarabstände von Stäbchen sind. Die ermittelten Abschirmlängen können die in den Simulationen beobachteten Diffusionskonstanten von Tracer-Kugeln quantitativ erklären.

Weitaus komplexer als Stäbchen-Suspensionen sind Vesikel, da sie zusätzlich über eine interne Dynamik verfügen. In einem zweidimensionalen Modell-System untersuchen wir Vesikel im Scherfluss. Diese zeigen eine Reihe interessanter dynamischer Phänomene. Abhängig vom Verhältnis der Viskositäten innerhalb und außerhalb des Vesikels, können sie entweder taumeln, schwingen, oder sie zeigen "Tank-Treading". Beim "Taumeln" rotiert die Orientierung des Vesikels ständig, beim "Schwingen", weißt das Vesikel zeitlich periodische Veränderungen in Form und Orientierung auf, und im Bereich des "Tank-Treading" bleiben Form und Orientierung zeitlich konstant, jedoch bewegt sich die umgebende Membran wie die Kette eines Raupenfahrzeuges um die eingeschlossene Flüssigkeit. Zum ersten Mal konnte hier mit Computer Simulationen das "Schwingen" bei Erhöhung des Viskositätskontrast gezeigt werden. Es ergibt sich eine gute Übereinstimmung mit einer phenemenologischen theoretischen Beschreibung.

In der Nähe von Wänden wird das Taumeln unterdrückt. Hinzu kommt, dass das Vesikel von der Wand abgestoßen wird. Die Ursache dafür ist die hydrodynamische "Lift-Force". Wir finden, dass die Lift-Force umgekehrt proportional zum Quadrat des Wandabstandes abfällt, und dass sie mit zunehmendem Viskositätskontrast schwächer wird. Die Lift-Force ist insbesondere für die Bewegung von Blutkörperchen im Blutstrom von Relevanz.

Erklärung

Ich versichere, dass ich die von mir vorgelegte Dissertation selbständig angefertigt, die benutzten Quellen und Hilfsmittel vollständig angegeben und die Stellen der Arbeit - einschließlich Tabellen, Karten und Abbildungen -, die anderen Werken im Wortlaut oder dem Sinn nach entnommen sind, in jedem Einzelfall als Entlehnung kenntlich gemacht habe; dass diese Dissertation noch keiner anderen Fakultät oder Universität zur Prüfung vorgelegen hat; dass sie - abgesehen von unten angegebenen Teilpublikationen - noch nicht veröffentlicht worden ist sowie, dass ich eine solche Veröffentlichung vor Abschluss des Promotionsverfahrens nicht vornehmen werde. Die Bestimmungen dieser Promotionsordnung sind mir bekannt. Die von mir vorgelegte Dissertation ist von Prof. Dr. G. Gompper betreut worden.